AD NUMBER
AD339912
CLASSIFICATION CHANGES
TO: unclassified
FROM: secret
LIMITATION CHANGES
TO: Approved for public release, distribution unlimited
FROM: Distribution authorized to DoD only; Administrative/Operational Use; 04 FEB 1960. Other requests shall be referred to Defense Atomic Support Agency, Washington, DC.
AUTHORITY
DNA ltr dtd 26 Jan 1996; DNA ltr dtd 26 Jan 1996

Operation

REDWING

PACIFIC PROVING GROUNDS

May - July 1956

Project 3.1

THERMAL and BLAST LOAD PROTECTION for B-47E AIRCRAFT in FLIGHT (U)

Publication Date: February 4, 1958

HEADQUARTERS FIELD COMMAND, DEFENSE ATOMIC SUPPORT AGENCY
SANDIA BASE, ALBUQUERQUE, NEW MEXICO

Inquiries relative to this report may be made to:

Chief, Defense Atomic Support Agency
Washington 25, D. C.

When no longer required, this document may be destroyed in accordance with applicable security regulations.

DO NOT RETURN THIS DOCUMENT

WT-1327

OPERATION REDWING— PROJECT 5.1

THERMAL and BLAST LOAD EFFECTS on a B-47E AIRCRAFT in FLIGHT (U)

R. C. Laumann, 1st Lt, USAF
W. M. Gran
R. H. Heineman
R. P. Lang

Cook Research Laboratories
Cook Technological Center
Morton Grove, Illinois

Wright Air Development Center
Air Research and Development Command
Wright-Patterson Air Force Base, Ohio

ABSTRACT

Project 5.1 was established to measure overpressure, gust, and thermal effects on a B-47E aircraft in flight, and to provide additional research information on the effects of nuclear explosions on the aircraft. Results of this project will be used to correct the B-47E Weapons Delivery Handbook. Previous tests were conducted on a B-47E in Operations Ivy and Castle. Data obtained on these operations were primarily measurements of thermal effects. For Operation Redwing, a B-47E aircraft was instrumented for measurement of overpressures, irradiance, radiant exposure, and of bending, shear, and torsion in the wing and stabilizer. Further instrumentation was made to measure thermal strain and the effect of high thermal inputs upon thin skins and supporting structures. Instrumentation was also installed to obtain bending, shear and torsion responses of the fuselage when subjected to combined side and vertical loading.

The general positioning criteria for the aircraft were wing bending up to 95 percent of design limit and/or a temperature rise of 600 to +700 F in the thin-skinned elevator and aileron. In order to attain high temperature rises on participations in which the aircraft was gust critical, it was necessary to paint the thin-skin surfaces with high absorptivity paint. Temperatures of 430 to 547 F received during Shots Zuni and Dakota caused only minor permanent buckling in the aileron and elevator and resulted in no control problems or noticeable increase in drag. During Shot Dakota, the aircraft sustained 89 percent of design limit wing bending and an overpressure of 0.80 psi. On other participations, wing loading ranged from 46 to 75 percent of design limit, and no damage resulted.

The data obtained by participation of the B-47E aircraft in Operation Redwing are sufficient for correction of the existing B-47E Weapons Delivery Handbook. The data should also be useful as basic research information to aid in design of future USAF aircraft.

FOREWORD

This report presents the final results of one of the projects participating in the military-effect programs of Operation Redwing. Overall information about this and the other military-effect projects can be obtained from WT-1344, the "Summary Report of the Commander, Task Unit 3." This technical summary includes: (1) tables listing each detonation with its yield, type, environment, meteorological conditions, etc.; (2) maps showing shot locations; (3) discussions of results by programs; (4) summaries of objectives, procedures, results, etc., for all projects; and (5) a listing of project reports for the military-effect programs.

CONTENTS

ABSTRACT ---- 4

FOREWORD ---- 5

CHAPTER 1 INTRODUCTION ---- 11

1.1 Objective ---- 11
1.2 Background ---- 11
1.3 Theory ---- 12

CHAPTER 2 INSTRUMENTATION ---- 14

2.1 Transducers ---- 14
2.1.1 Calorimeters and Radiometers ---- 16
2.1.2 Thermocouples ---- 16
2.1.3 Strain Gages, Gust Loads ---- 16
2.1.4 Strain Gages, Thermal Stress ---- 16
2.1.5 Pressure Transducers ---- 17
2.1.6 Accelerometers ---- 17
2.1.7 Rate Gyro ---- 17
2.1.8 Recorders ---- 17
2.1.9 Photographic Equipment ---- 18
2.1.10 Time-Zero Reference ---- 18
2.1.11 Timing Oscillator ---- 18
2.1.12 Bridge Battery ---- 18
2.2 Application ---- 18
2.2.1 Thermal Inputs ---- 18
2.2.2 Temperature Rise ---- 20
2.2.3 Strain ---- 20
2.2.4 Overpressure Measurements ---- 24
2.2.5 Engine Effects ---- 24
2.2.6 Acceleration ---- 24
2.2.7 Rate of Pitch ---- 24
2.2.8 Shock Velocity ---- 24
2.2.9 Angle-of-Attack Indicators ---- 25
2.2.10 Control Surface Position Indicators ---- 26
2.2.11 Aircraft Space Positioning and Position Measurement ---- 26
2.2.12 Visible Effects, Data Cameras ---- 26
2.2.13 Camera Frame-Time Correlation ---- 26
2.3 Calibration ---- 27
2.3.1 Calorimeters and Radiometers ---- 27
2.3.2 Thermocouples ---- 27
2.3.3 Strain Gages ---- 27
2.3.4 Pressure Systems ---- 28
2.3.5 Accelerometers ---- 28
2.3.6 Rate Gyro ---- 28

2.3.7 Time-Interval Equipment ---- 28
2.3.8 Control Surface Sensors ---- 28
2.3.9 Angle-of-Attack Indicator ---- 28
2.3.10 Aircraft Instruments ---- 29

CHAPTER 3 OPERATIONS ---- 30

3.1 Shot Participations ---- 30
3.2 Flight Plans ---- 30

CHAPTER 4 RESULTS ---- 33

4.1 Operational Results ---- 33
4.2 Thermal Input ---- 33
4.3 Thermal Responses ---- 33
4.3.1 Temperature Rise ---- 33
4.3.2 Thermal Strain ---- 38
4.4 Gust Inputs ---- 42
4.5 Gust Load Effects ---- 43
4.5.1 Aircraft Disposition ---- 43
4.5.2 Structural Response ---- 47
4.5.3 Effects on Engine Performance ---- 53

CHAPTER 5 DISCUSSION ---- 54

5.1 Thermal Inputs ---- 54
5.2 Thermal Responses ---- 56
5.2.1 Temperature Rises ---- 56
5.2.2 Visible Effects ---- 56
5.2.3 Thermal Strain ---- 56
5.3 Gust Inputs ---- 59
5.4 Gust Load Effects ---- 60
5.4.1 Aircraft Disposition ---- 60
5.4.2 Structural Response ---- 62
5.4.3 Visible Damage ---- 62
5.4.4 Engine Response ---- 65

CHAPTER 6 CONCLUSIONS AND RECOMMENDATIONS ---- 66

6.1 Conclusions ---- 66
6.2 Recommendations ---- 66

APPENDIX A TRANSDUCER DATA ---- 67

APPENDIX B INPUT AND RESPONSE THEORY ---- 70

B.1 Overpressure and Material Velocity Prediction ---- 70
B.2 Thermal Energy Received ---- 70
B.3 Response to Blast Loading ---- 71
B.4 Thermal Response ---- 72

REFERENCES ---- 73

TABLES

2.1 Calorimeter and Radiometer Types ---- 16

3.1 Shot Participation and Predicted Results ---- 31
4.1 Summary of Operational Results ---- 34
4.2 Meteorological Data ---- 35
4.3 Thermal Radiation ---- 36
4.4 Summary of Peak Temperature Rise ---- 36
4.5 Summary of Peak Elevator Strains, Cap Mounted Gages ---- 41
4.6 Summary of Peak Elevator Strains, Internally Mounted Rosettes ---- 41
4.7 Summary of Peak Elevator Strains, Lower Skin Mounted Rosettes ---- 44
4.8 Summary of Gust Inputs ---- 44
4.9 Summary of Peak Attitude Changes and Accelerations ---- 44
4.10 Summary of Gust Load Effects ---- 50
4.11 Reference Bending Moments (in-lb $\times 10^{-6}$) ---- 51
4.12 Summary of Engine Performance ---- 51
5.1 Summary of Peak Left Elevator Strains, Upper Skin Mounted Rosette ---- 58
5.2 Calculated Gust Inputs and Attitudes ---- 62
A.1 Summary of Transducers ---- 68

FIGURES

2.1 Major areas of instrumentation ---- 15
2.2 Close-up view of ground-zero and vertical mounts ---- 19
2.3 Close-up view of optigraph and forward scatter mounts ---- 21
2.4 Sensor locations in the empennage area ---- 22
2.5 General location of thermocouple installations on the aircraft ---- 23
2.6 Location of instrumentation on No. 6 engine ---- 25
3.1 Typical flight pattern ---- 31
4.1 Time-history representation of irradiance, radiant exposure, and temperature rise on reference panel, ground-zero mount, for Shot Dakota ---- 37
4.2 Time-history representation of temperature rise on the inboard instrumented rib of the right elevator ---- 38
4.3 Time-history representation of chord-wise temperature distribution on the lower skin of the right stabilizer when painted white ---- 39
4.4 Time-history representation of span-wise temperature distribution on the lower skin of the right stabilizer when painted white ---- 39
4.5 Time-history representation of temperature rise on the radome as a function of surface condition ---- 40
4.6 Time-history representation of temperature rise on the aluminum and magnesium panels of the bomb-bay door ---- 40
4.7 Relative rib strains versus maximum lower skin temperature rise ---- 42
4.8 Residual buckles evident in the lower skin of the left elevator after Shot Dakota ---- 43
4.9 Time-history representation of overpressure taken at the aircraft during Shot Dakota ---- 45
4.10 Time-history representation of differential vertical acceleration taken at the aircraft center of gravity during Shot Dakota ---- 45
4.11 Time-history representation of differential angle of attack taken during Shot Dakota ---- 46
4.12 Time-history representation of differential rate of pitch taken during Shot Dakota ---- 46
4.13 Time-history representation of differential wing bending moment taken during Shot Dakota ---- 47

4.14 Time-history representation of differential stabilizer bending moment taken during Shot Dakota ---- 48
4.15 Time-history representation of differential bending moment taken at Fuselage Station 800.0 during Shot Dakota ---- 48
4.16 Time-history representation of differential bending moment taken at Fuselage Station 1044.0 during Shot Huron ---- 49
4.17 Time-history representation of differential wing deflection taken during Shot Flathead ---- 49
4.18 Time-history representation of differential engine pressure taken during Shot Dakota ---- 52
4.19 Time-history representation of engine temperature taken during Shot Dakota ---- 52
5.1 Predicted versus measured radiant exposure incident upon a horizontal plane ---- 55
5.2 Predicted versus measured total radiant exposure direct from ground zero ---- 55
5.3 Integrated radiometer inputs versus calorimeter inputs ---- 57
5.4 Predicted versus measured temperature rise ---- 57
5.5 Related rib strains of the left elevator thermal panel ---- 59
5.6 Predicted versus measured overpressure ---- 60
5.7 Comparison of differential pressures taken at points tangential and normal to the impinging shock front ---- 61
5.8 Predicted versus measured bending moment at Right Wing Station 615.0 ---- 63
5.9 Predicted versus measured bending moment at Left Wing Station 493.0 ---- 63
5.10 Comparison of the percent limit bending moments of Wing Stations 615.0 and 493.0 ---- 64
5.11 Gust damage evident in the bomb-bay area after Shot Dakota ---- 64

Chapter 1
INTRODUCTION

1.1 OBJECTIVE

The primary objective of this project was to measure overpressure, gust, and thermal effects of a nuclear detonation on a B-47E aircraft in flight. With the recorded data, criteria and methods used in the B-47E Weapons Delivery Handbook could be verified or corrected. In addition, the project was to provide basic research data for design criteria of future USAF aircraft.

1.2 BACKGROUND

Since the original tests of nuclear devices, considerable effort was made to determine their effect on aircraft systems. In the earlier tests, participation was limited because of a lack of knowledge of weapon characteristics and the effects of these characteristics upon aircraft systems.

During Operations Ivy and Castle, a B-47B aircraft was instrumented and positioned to obtain responses of sufficient magnitudes to allow prediction of delivery capabilities of the aircraft. Data obtained during Operation Ivy were used to establish a more accurate theory relating skin-temperature rise and distribution in aircraft structures to physical inputs from the weapon. Under a Wright Air Development Center (WADC) contract, the University of California at Los Angeles (UCLA) studied, designed, and built a furnace for simulation of thermal loads application, and the data obtained were correlated with experimental data from Operation Ivy (Reference 1). This theory was used on Operation Castle as a guide to establish aircraft positions.

During Operation Castle the aircraft was positioned to receive radiant exposures sufficient to elevate thin-skinned aileron and elevator sections approximately 350 F bove ambient temperature. At this temperature thermal loads were expected to cause some plastic deformation. The maximum temperature rise obtained was less than 200 F (Reference 2). No plastic deformation or adverse effects were noted on any part of the aircraft; however, measurements of thermally induced loads deviated considerably from predictions. A study of these effects was made (Reference 3) which demonstrated that the observed differences were caused by a thermal lag phenomenon, resulting in a temperature difference between the skin and the strain gage element used to measure the thermal loads. Although the primary objective of measuring the effects of plastic deformation was not achieved, much valuable information was obtained which led to improved devices and instrumentation techniques for the measurement of thermal loads (Reference 4).

While participating in Operation Castle, a B-36D experienced an unexpectedly large increase in engine-tailpipe temperature immediately after shock arrival (Reference 5). Subsequently, a study of the phenomenon was initiated by the Power Plant Laboratory, WADC. As a result of this study, one engine of the B-47E was instrumented for the measurement of engine performance parameters during Operation Redwing.

In previous operations, radiant exposure levels were limited primarily by theoretical structural limitations. Higher levels of radiant exposure were anticipated from Operation Redwing, however, with the consequence that the possibility of damage to secondary aircraft components had to be reinvestigated. It was found that if the radome of the bombing-navigational radar were elevated to a sufficiently high temperature, the outer skin laminate would separate from the honey-

comb substructure (i.e., filler). Separation of the outer laminate would lower the strength of the radome, making it more vulnerable to gust effects. During Operation Castle, gust effects were observed on the B-36D radome, which was buckled on Shot 1 at an overpressure of 0.81 psi. A further decrease in radome strength resulting from thermal effects might limit the operational capability of the B-47E; therefore, this possibility was investigated during Operation Redwing.

1.3 THEORY

In order to measure the effects of a nuclear explosion on a B-47E aircraft, it was necessary that the following phenomena be considered: (1) direct gamma radiation; (2) rise of the radioactive cloud; (3) overpressure of the shock wave; (4) material velocity (i.e., gust) following the shock wave; and (5) thermal radiation from the fireball.

The USAF dosage level of 25 rem for bombing operations was a limiting factor for low-altitude delivery of low-yield devices. However, this gamma-radiation level fell within the danger envelopes of other positioning criteria as the yield of the device increased. For the yields of Operation Redwing, direct gamma radiation was not a limiting position criterion.

Although the danger from the rise of the radioactive cloud increases with higher yield devices, experience gained from Operations Ivy and Castle indicates that the cloud lies within the danger envelopes for one of the other limiting phenomena. For a 5-Mt device, the cloud required nearly a minute to rise to test altitude; therefore, it could be avoided with high-speed aircraft.

Analysis and laboratory investigations have established the criterion for safe operation without overpressure damage; namely, the point above which damage to bomb-bay doors, radome, or engines will occur (Reference 6). The limit was established as 1.0 psi peak overpressure for the B-47E. Normally, this region falls within the danger envelopes of the thermal radiation and gust loading of the critical structure.

The factor most significantly affecting the limit to operational capabilities of the B-47E aircraft, for the yield ranges studied during Operation Redwing, was the gust loading effect on the primary structure. Under nearly all conditions, the limit overpressure envelope of 1.0 psi lies within the danger region envelope for limit allowable gust. For detonations having a yield less than approximately 5 Mt, effects of radiant exposure on an all-white aircraft with absorptivity, α, of approximately 0.22 can also be neglected.

The dynamic analyses of wing and horizontal stabilizer reactions to gust loading given in Reference 6 were used to evaluate danger-region diagrams for Operation Redwing participation of the B-47E aircraft. The analyses were used to evaluate the dynamic magnification factor (amplification in load over that expected under static conditions with identical type of load distribution) and most critical stations of the wing and stabilizer. By use of the theoretical values of this factor for the wing and stabilizer, the most critical section of the aircraft was found to be Wing Station 465.0. However, since Station 465.0 was inaccessible for instrumentation, Wing Station 493.0 was instrumented, and hereinafter in this report, Station 493.0 is referred to as the critical wing station. At Station 493.0 the 1.0 g flight load was 1.86×10^6 in-lb. An incremental bending moment of 4.14×10^6 in-lb could be sustained without exceeding the allowable design limit, i.e., 100 percent of limit load which is, effectively, the same incremental increase which could be sustained at Wing Station 465.

The analysis conducted by UCLA to determine the most vulnerable area of the B-47B aircraft to damage resulting from radiant exposure during Operation Castle was continued and extended by Allied Research Associates (Reference 7) to include analysis of the B-47E aircraft for participation during Operation Redwing. The investigations established that the most vulnerable areas on the aircraft were the 0.020-inch aluminum skin on the aileron; the 0.025-inch aluminum skin on the elevators; and, to a somewhat lesser extent, the 0.032-inch skin on the flaps. Since the aileron sections did not lend themselves easily to instrumentation, it was decided that the 0.025-inch elevator section would be the primary test section used in Operation Redwing and that cor-

relating temperature measurements would be made on the aileron and other selected sections.

To ensure that the thin-skinned sections reached temperatures sufficient to cause plastic deformation, the absorptivity (α) of the test areas (elevator, aileron, and flap) was increased through the use of paints varying in color to black (α = 0.96). High absorptivity paints were used on the lower-yield shots (under 1.0 Mt) in order to bring the danger region envelopes for gust and thermal radiation into closer coincidence. In this manner, it was possible to position the aircraft to receive near-limit values of both these variables. On higher-yield shots, α had to be progressively decreased in order to maintain a coincidence of danger envelopes.

From the investigations described in Reference 7, it was determined that some permanent buckle of the elevator skin would begin at approximately 380 F above ambient and that failure because of 1.0 g flight loads on a heated section would probably not occur below temperatures of 900 F. An analysis was made to determine the flight capabilities of the B-47E aircraft if such a section were damaged in flight. It was concluded that the aircraft would be in no danger from either flutter or control effects because of buckling, should the lower skin of the elevator section rise 650 F. The conclusion was that, should the lower skin of both elevators be severely buckled, the aircraft would remain stable and maneuverable and that radiant exposure of the instrumented section would not be a limiting factor. However, difficulty could be encountered in an attempt to land an aircraft in this condition. To land with only one damaged elevator would entail less risk. Consequently, only one elevator at a time was completely painted with high-absorptivity paint, while small patches (three to five rib sections) were similarly coated on the other elevator, aileron, and flaps. In this way, if severe thermal damage were encountered, all control surfaces with the exception of one elevator would be essentially intact.

An additional thermal consideration resulted from the use of MIL-E-7729 white paint on the underside of the aircraft. Experiments conducted by the Materials Laboratory, WADC, established that this paint would begin to char at a temperature of 425 F, with a consequent increase in absorptivity. Tests were conducted at the Eniwetok Proving Ground to determine the relationship between peak temperature and change in absorptivity, so that this factor could be taken into account to predict peak temperature rise during evaluation of aircraft position for shot participation. The tests were made by use of the Cook Research Laboratories thermal source, which produced a radiant exposure of approximately 1.5 cal/cm^2. A reflectometer (Taylor Integrating Sphere) was used to make measurements of absorptivity (averaged over a wave-length band of 600 to 800 mμ). The rate of temperature rise and decay was approximately 15 F/sec. Results of these tests were used as positioning criteria during the latter part of the operation.

Gust effects on the turbojet engines[1] of the B-47E aircraft were expected to result in changes in engine performance which would create an increase in tailpipe temperature and possibly a flameout. Engine tests were conducted during this operation to establish a relationship between gust inputs and engine effects. It was expected that the principal effects would be either unchoking of the exhaust nozzle or flow distortion at the compressor inlet, causing undesired changes in the engine's operation (e.g., excessive increase in tail-pipe temperature).

On those shots where near-limit values of both radiant exposure and air blast were expected, the radome of the bombing-navigational radar had to be considered a possible limiting factor to operations. The radome was painted white according to standard aircraft configuration, except for an area 6 inches in diameter which was left unpainted. In this manner it was possible to study the absorption, transmission of radiant exposure, and heat transfer characteristics of the laminate in a small area.

---

[1] General Electric Type J47-25, Serial No. 063-880, instrumented.

Chapter 2
INSTRUMENTATION

The B-47E was instrumented for the in-flight measurement of thermal, overpressure, and gust inputs and effects resulting from operation in the vicinity of high-yield detonations.

Thermal inputs measured were radiant exposure (broad and spectral bands) and irradiance. Measurements were made normal to a line from the detonation to the aircraft, normal to the horizontal plane of flight, for radiant exposure transmitted through the radome, and for scattered radiant exposure coming in from above the aircraft. Blast inputs measured were overpressure and shock propagation time.

Thermal effects, such as temperature rise and distribution and resultant strains in thin-skinned sections and supporting structures, were measured. Temperature rise of the radome and covered and uncovered thermocouples (convection calorimeter) installed on the lower surfaces of the stabilizer and aileron were also measured. An integral unit consisting of one covered and one uncovered thermocouple constituted a convection calorimeter. Gust loads effects such as shear, bending moment, and torsion resulting from gust loads were measured on the wing, empennage, and fuselage. The effects on engine performance were monitored on the No. 6 engine. Additional miscellaneous backup data were obtained from rate gyro, free gyro, and angle-of-attack indicators for use in evaluation of aircraft attitude changes and self-induced reaction loads.

Aircraft space-position information was obtained in flight from the K-4 radar bombing and navigational system and monitored by use of photopanel records. Primary flight position measurements were made by use of a Raydist navigational system. Mapping-camera photos, radarscope photos, and photos from cameras aimed at ground zero were used as a supplementary source of position data.

Data were recorded on oscillograph paper, magnetic tape, and film. A central recording assembly located in the aircraft bomb bay provided a facility for the recording of 300 data channels, plus automation for single channel readout during maintenance and calibration and semiautomatic in-flight operation and sequencing. In addition, seven magnetic tape-recorder channels and 20 data cameras were operated on all test flights.

2.1 TRANSDUCERS

A comprehensive list of transducers and the recording capacity is given in Appendix A. The locations on the aircraft of the major areas of instrumentation are shown in Figure 2.1. Details of installation and location of instrumentation elements are specified completely in Reference 8.

During the period between Shots Zuni and Flathead, information was received from the Aircraft Laboratory, WADC, that, under certain dynamic loading conditions, Wing Station 615.0 could become critical. As a consequence, eight strain-gage bridge channels were installed to obtain bending, shear, and torsion. Later in the program, it was decided to increase the scope of the project to include the evaluation of side-load effects on the fuselage. To measure side-load effects, two fuselage stations, 800.0 and 1044.0, were instrumented with 14 and 17 strain gage bridges, respectively.

Other additions consisted of: (1) a convection calorimeter in the aileron at Wing Trailing Edge Station 476.0; (2) a right-elevator ripple camera aimed at the instrumented elevator section; (3) an angular accelerometer at Fuselage Station 560.0; and (4) eight channels to record pressure and temperature information on Engine No. 6.

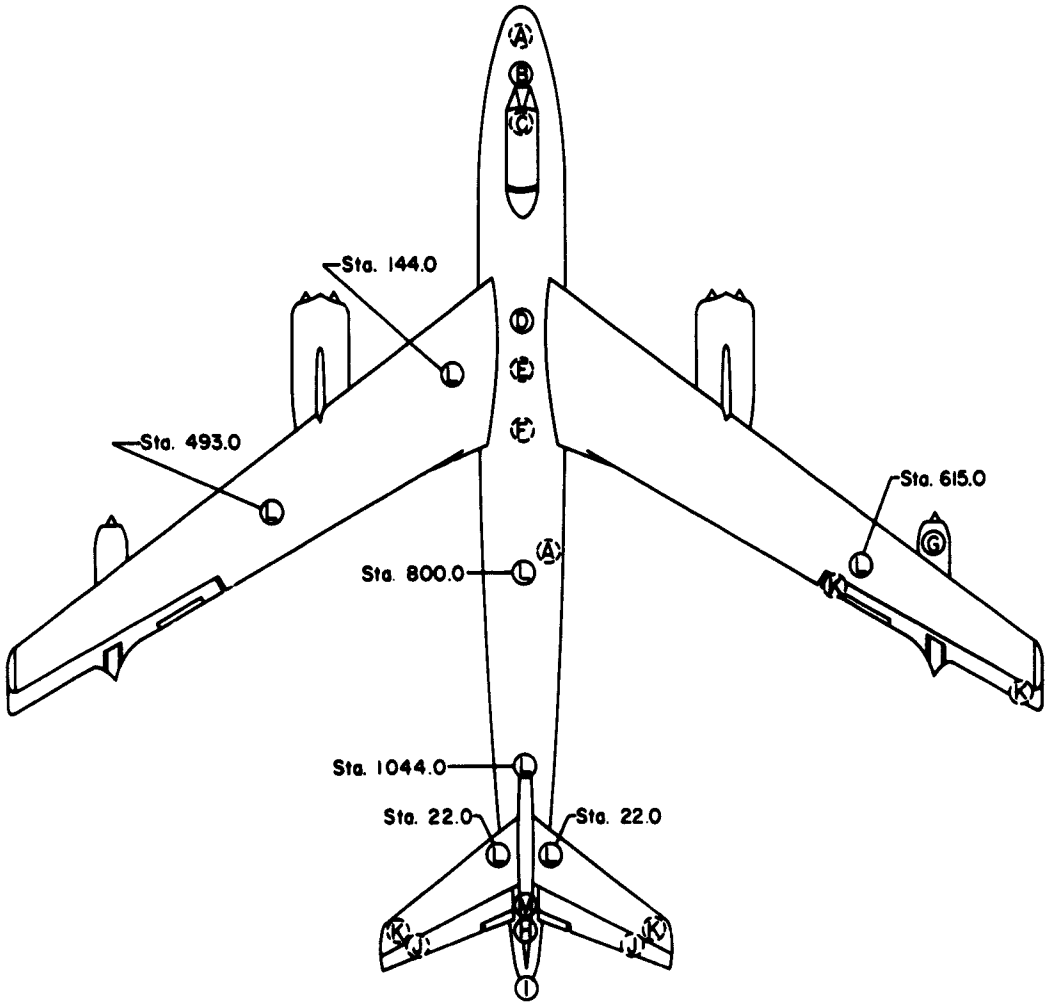

(A)	PHOTO PANEL	(Navigator Compartment, Chaff Chute)
(B)	SCATTER MOUNT	(Calorimeters, N-9 Cameras)
(C)	RADOME	(Calorimeters, Thermocouples)
(D)	OPTIGRAPH MOUNT	(Calorimeters, N-9 & Beattie Cameras)
(E)	BOMB-BAY AREA	(Central Recording Assembly, Thermocouples)
(F)	CENTER OF GRAVITY	(Linear & Angular Accelerometers, Rate Gyro)
(G)	#6 ENGINE	(Thermocouples, Pressure Transducers)
(H)	TRUE VERTICAL MOUNT	(Calorimeters, N-9 Cameras)
(I)	GROUND ZERO MOUNT	(Thermal Reference Panel, Calorimeters, Radiometers, N-9 Cameras, T_0 Indicator)
(J)	THERMAL PANEL	(Strain Gages, Thermocouples)
(K)	THERMOCOUPLE AREA	(Thermocouples)
(L)	GUST LOAD STATION	(Moment & Shear Strain Gage Bridges)
(M)	PRESSURE RING	(Pressure Transducers)

Figure 2.1 Major areas of instrumentation.

2.1.1 Calorimeters and Radiometers. The calorimeters and radiometers used for the measurement of radiant exposure and irradiance were supplied by the U. S. Naval Radiological Defense Laboratories (NRDL). Disk-type calorimeters and foil-type radiometers were used for all direct measurements, while some 10 and 20 button foil-type calorimeters were used for scattered radiant exposure measurements. The instrument types and filters used to obtain measurements in broad or spectral bands are specified in Table 2.1. The sensitivity of each instrument and associated recording channel was determined prior to each shot. Thus, many different instrument types and filter combinations were utilized during the course of the operation.

2.1.2 Thermocouples. The majority of the thermocouples used were of the copper-constantan (c-c) type. Each junction consisted of two copper and two constantan wires (10 or 15 mil) percussion welded to the metal surface in close proximity to each other. Each pair of wires was

TABLE 2.1 CALORIMETER AND RADIOMETER TYPES

Instruments		Filters	
Type	Range	Type	Field of View
			deg
Radiometer, RF-10	10 (cal cm^2)/sec	Quartz	21
Radiometer, RF-50	50 (cal cm^2)/sec	Quartz	45
Calorimeter, Red	10 to 20 + cal/cm^2	Quartz	90
Calorimeter, Black	5 to 20 cal/cm^2	Quartz	160
Calorimeter, White	2.5 to 10 cal/cm^2	3-69 *	90
Calorimeter, Brass	1.5 to 3 cal/cm^2	2-73 *	90
		2-58 *	90
		RG-8 †	90
		RG-8 †	160
		7-56 *	90
		Ge + 7-56 ‡	90

* Corning Glass Works color specification.
† Schott-Jena Glass Works, West Germany, code specification.
‡ Ge - Germanium.

connected in parallel to reduce the possibility of data loss due to failure of the small gage wires. In several instances where a nonmetallic material was instrumented for temperature distribution, c-c junctions were made by butt welding 10-mil wire. Where temperatures of over 700 F were anticipated, welded chromel-alumel (c-a) thermocouples were installed. All thermocouples were referenced to an ice bath at 32 F.

2.1.3 Strain Gages, Gust Loads. All strain gages used throughout the aircraft for gust load measurements, with the exception of the gages used on the outer skin surface of the two stabilizers, were Baldwin SR-4 Type EBDF-13D (minus). They were temperature compensated for use on 24ST aluminum from −50 F to +300 F. The gages used on the stabilizer skin were Baldwin SR-4, Type EBDF-13Q strain gages.

2.1.4 Strain Gages, Thermal Stress. The quartz compensated (Q gage) strain gage, designated EBDF-13Q, was developed by the Cook Research Laboratories and manufactured by the Baldwin-Lima-Hamilton Corporation. The Q gage was used for the measurement of all thermal strain. This instrument is, ideally, a temperature-insensitive gage which gives an output proportional to elongation strain, where correspondingly the EBDF-13D gage gives an output proportional to direct, stress-inducing strain. (Both relations apply only to conditions of thermal equilibrium.)

The advantage of the Q gage in the measurement of thermal strains was that the compensation error caused by thermal lag (difference in temperature between panel and strain sensitive filament) was small. Therefore, any uncertainty in the evaluation of this temperature difference results in only a small error. The corrections which must be applied when using D gages, however, result in strain compensation approximately proportional to this temperature difference.

2.1.5 Pressure Transducers. The five overpressure measurements on the fuselage were made with Statham Type P-131-2.5D-350 pressure transducers. These instruments sensed differential pressure within a range of ± 2.5 psi. The static side of each overpressure transducer was vented to ambient pressure through a solenoid valve which was closed immediately prior to taking measurements. Thus, the static side of each transducer was always referenced to ambient pressure. Orifice openings for these gages were identical to those used on the aircraft static system and had a pneumatic response in excess of 200 cps. The Statham P-69-1D-350 gage that formed the sensing element of the stabilizer angle-of-attack indicator was also of the differential type, with a range of 1 psi. Aircraft ram and static pressure systems were monitored by Statham P-68 absolute pressure gages having ranges of 0 to 30 psi and 0 to 10 psi, respectively.

In the instrumentation of the engine, six pressure transducers were used. Four were differential gages and two were absolute gages. Instruments used to record compressor-inlet pressure differential were Statham P-69 transducers, two with a range of 0 to 3 psi and one with a range of 0 to 1 psi. The P-96-20D-350 differential transducer installed to measure compressor discharge pressure was similar to the P-69 gages mentioned above. Tail-pipe pressure was recorded by means of a Statham P-68-30A-350 gage identical to that used to monitor the ram pressure system. A Statham P-122-500A-500 absolute gage was installed to measure the pressure in the small slot fuel system.

All pressure gages used unbonded strain-gage wire as the transducing element, electrically connected as a Wheatstone bridge. The operating temperature range specified by the manufacturer (−60 to +200 F) was adequate to accommodate all instrument requirements on the aircraft. Gages differed in frequencies of natural resonance and sensitivity and in methods of installation required for each type of measurement.

2.1.6 Accelerometers. Three linear accelerometers, Giannini Type 24118, and one angular accelerometer, Statham Type AA17B, were installed in the aircraft. The functions, model numbers and specifications for the units were:

Function	Model	Range
Vertical acceleration	Giannini Type 24118-5-200	± 5 g
Longitudinal acceleration	Giannini Type 24118-1-200	± 1.0 g
Lateral acceleration	Giannini Type 24118-2½-200	± 2.5 g
Angular acceleration	Statham Type AA17B-3-300	± 3 rad/sec^2

The Giannini units were of the spring-supported-mass type incorporating magnetic damping and potentiometer output. The two arms of the potentiometer were matched with external resistances to complete the bridge circuit. Sensing circuit of the Statham angular accelerometer consisted of an unbonded strain-gage bridge coupled to a spring-supported mass. All units were designed to function within the temperature range of −60 to +150 F.

2.1.7 Rate Gyro. A rate gyro, Model RG-01-0200-1, manufactured by the Pacific Scientific Company, was installed in the aircraft. This unit was an air-damped, electrically operated gyro with a maximum input range of ± 10 deg/sec. The instrument was designed to operate within the temperature range of −50 to +170 F.

2.1.8 Recorders. The bulk of the transducer outputs were wired into a central recording assembly (CRA) located in the bomb bay. The assembly housed the recording oscillographs, timers,

bridge voltage supply, tape recorder, and the ice bath reference junction for all thermocouples. In addition, panel boards were provided in the CRA for the routing of signals to the appropriate recorder. Attenuating and damping resistors, balancing circuits, and automatic controls for individual and sequential channel selection (for test purposes) were also provided on these panel boards.

Six 50-channel, Consolidated Electrodynamics Corporation Type 5-119P3-52 recording oscillographs were located in the CRA. These recorded information as sensed by the transducers shown in Appendix A.

A seven-channel Ampex magnetic tape transport, with appropriate power supplies and amplifiers, was installed behind the copilot in the pressurized area of the cockpit. Data signals from the four calorimeters in the navigator's window and the two calorimeters in the optigraph canopy were amplified and recorded, together with a timing reference, on this instrument.

A voice recorder was installed in the CRA and connected to a point common to all channels of the aircraft's intercommunication system. This instrument was used to determine the reaction of the crew to noted phenomena and to record commentary on unusual events.

2 1.9 Photographic Equipment. Several types of photographic equipment were used in the aircraft. One of the most used was the 16-mm Bell and Howell N-9 gun-sight-aiming-point (GSAP) camera. This camera proved valuable because of its wide range of shutter and frame speeds. Two 35-mm Beattie Portronic Jr. Cameras were modified by Cook Research Laboratories for continuous film transport for use in an optigraph system developed by the National Advisory Committee for Aeronautics (NACA). Other cameras employed were the standard AF 16-mm B-1A, 35-mm A-4 and K-17C.

2.1 10 Time-Zero Reference. Selenium self-generating photoelectric cells, mounted in the aft ground-zero mount, were employed to establish a time-zero reference. The outputs of these cells were connected to each oscillograph for time correlation. Another cell of the same type was used to produce a time-zero indication for the frame-correlation camera. In this manner, time correlation between events was established.

2.1.11 Timing Oscillator. A 400-cps standard oscillator (American Time Products) modified to provide a 100-cps signal was installed in the CRA. This signal was fed to separate channels on each oscillograph to provide means for accurate measurement of time intervals.

. 1.12 Bridge Battery. A Sonotone Corporation nickel-cadmium battery of high capacity was installed in the CRA to provide a stable voltage source for the transducers. A signal proportional to the magnitude of this source was recorded on each oscillograph to monitor the source level throughout a test run.

2.2 APPLICATION

2.2.1 Thermal Inputs. Two radiometers and 16 calorimeters were installed in an adjustable (ground-zero) mount located on the tail turret at Fuselage Station 1330.0 (Figure 2.2). This mount was adjusted for each shot so that the instrument faces were normal to a line from the detonation to the aircraft. The fields of view of these instruments were recorded on six N-9 cameras located in the mount. Many of these calorimeters were equipped with filters to measure the spectral distribution of the radiant exposure.

A fixed mount on the underside of the fuselage at Station 1237.3 supported three calorimeters directed downward along an axis normal to the longitudinal and lateral axes of the aircraft (Figure 2.2). Two N-9 cameras recorded the fields of view of these calorimeters. A fourth vertical calorimeter was installed in the left stabilizer at Station 156.0. The face of this instrument was parallel to the elevator panel surface. With the elevator in neutral position, a measure of radiant exposure normal to the panel surface was obtained.

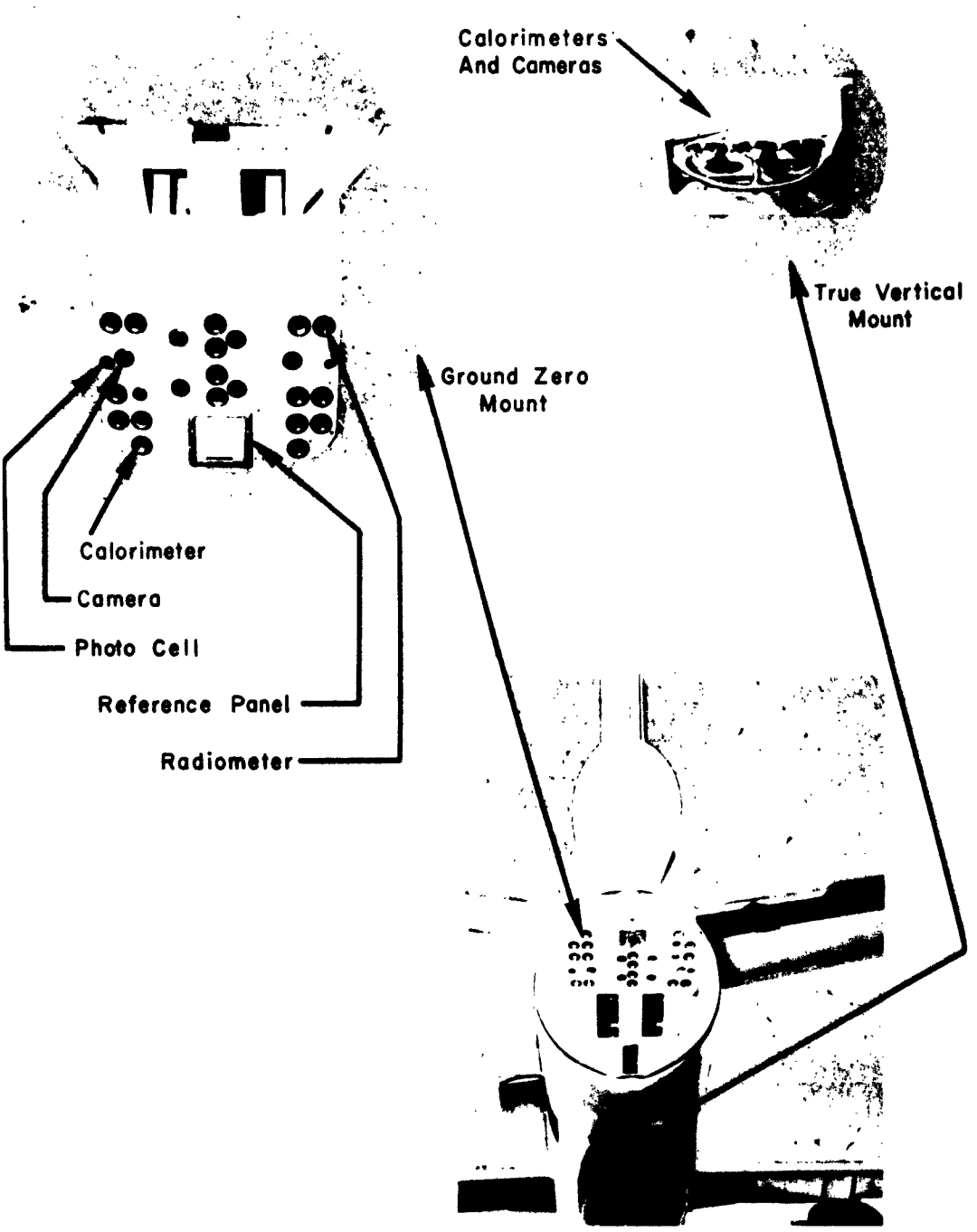

Figure 2.2 Close-up view of ground-zero and vertical mounts.

Four calorimeters and a camera were installed in a forward scatter mount at Fuselage Station 118.0. These instruments plus two calorimeters in the optigraph canopy (Figure 2.3) were used to measure radiant exposure (scatter) on the upper surface of the aircraft. One calorimeter oriented to measure back scatter was mounted in the ground zero mount with its sighting axis orthogonal to the line of sight to ground zero and in the vertical plane containing this line.

Radiant energy passing through the radome honeycomb material was measured by two calorimeters located just inside the radome surface. The paint was removed from the surface of the material in front of the right calorimeter to determine the effect of paint on transmission.

2.2.2 Temperature Rise. The right and left elevator sections at Station 148.0 were instrumented to measure the thermal effects on 0.025-inch aluminum skin and the structure supporting the skin. Fifteen thermocouples were installed on the left and 12 on the right elevator sections. The thermocouples were arranged on the panel and support members to measure temperature distribution.

The right stabilizer was equipped with a total of six thermocouples. At Station 192.0, five points were instrumented to determine the temperature distribution in the stabilizer's 0.040-inch skin. Three of these thermocouples sensed the isolated skin temperatures, while the other two were positioned to determine temperature near supporting structure. The remaining thermocouple was placed at Station 168.0 to sample the temperature of the 0.064-inch skin.

Left stabilizer Station 192.0 was instrumented with three pairs of calorimeters to determine the effects of convection cooling. The convection calorimeters were placed (isolated from the aircraft skin) in a chord-wise configuration in the lower stabilizer skin (Figure 2.4). Each pair consisted of two aluminum disks equipped with the. nocouples. One disk of the pair was placed flush with the aircraft skin and the other was shielded from the airstream by means of a glass cover having 0.92 transmission from 0.3 to 2.4 microns.

The right aileron was equipped with thermocouples installed in the 0.020-inch lower skin at two locations (Wing Stations 476.0 and 767.0) to measure temperature rise and distribution in the panels. Three thermocouples each were installed at Fuselage Stations 488.0 and 599.0 in the right bomb-bay door. These were used to establish the relationship between the effects of radiant exposure on 0.040-inch magnesium (Station 599.0) and 0.032-inch aluminum (Station 488.0). The radome was instrumented with two groups of three thermocouples to measure the thermal conductivity of the laminate material.

A reference panel designed for mounting in the ground-zero mount was instrumented with five thermocouples. By changing the absorptivity (α) of its surface (various paints), the temperature rise in the panel could be varied for a given thermal exposure to correspond with the temperature rise in the instrumented elevator sections.

Figure 2.5 shows the locations of all thermocouple installations on the aircraft.

2.2.3 Strain. The strains induced into the left and right elevator structural components at Station 148.0 by means of thermal loads were measured with 64 strain gage bridges. Because of the possibility of damage to the original elevators, a spare set of elevators was instrumented identically to the elevators installed on the aircraft.

On the 0.025-inch aluminum skin of each elevator, three equiangular strain-gage rosettes were placed on the inner skin of the lower surface and three were placed directly below these on the outer skin surface (back to back). Each gage of the rosettes functioned as the single active arm of a Wheatstone bridge. A junction box installed in the aft fuselage at Station 1235.0 contained the inactive arms of these bridges, which were mounted free of strain. The left elevator had one rosette mounted on the inside surface of the upper skin. In addition to the rosettes placed on the skin of the elevator, the left elevator was instrumented with a rosette on the web of each of the adjacent supporting members, i.e., the front spar, inboard rib, and outboard rib. On the right elevator, rosettes were mounted on the web surface of the front spar and inboard rib only. Six strain measurements were made on the left elevator by the use of two active arms

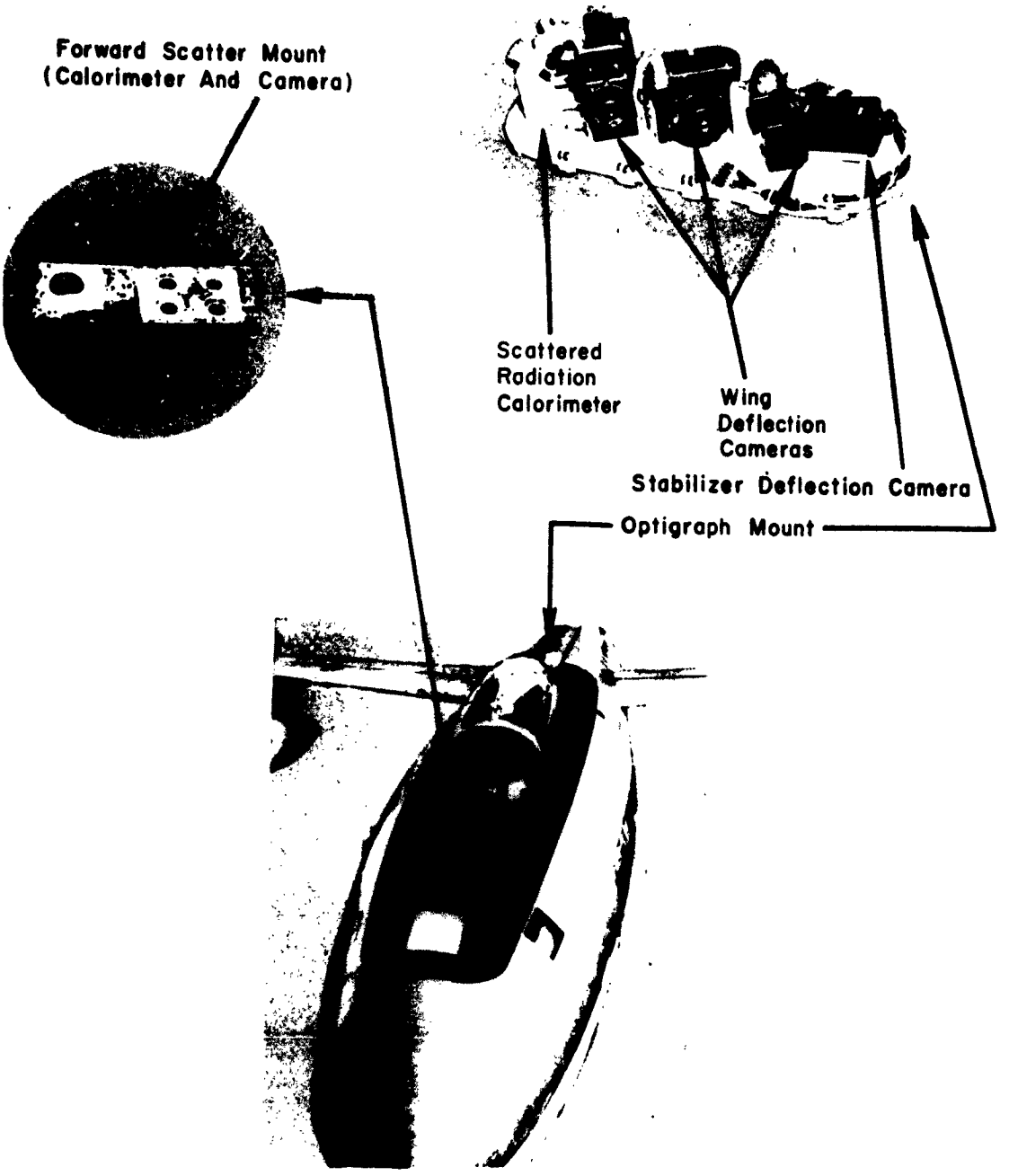

Figure 2.3 Close-up view of optigraph and forward scatter mounts.

each on the upper and lower caps of the primary adjacent support members. Instrumentation of the right elevator was identical to the left, with the exception that the outboard rib was not instrumented. The two inactive arms necessary to complete each bridge circuit were mounted on strain-free supports located on the front spars of the respective elevators.

The reference panel (Section 2.2.2) which was mounted in an unrestrained condition was also instrumented with two equiangular Q-type strain-gage rosettes back to back at its center. The

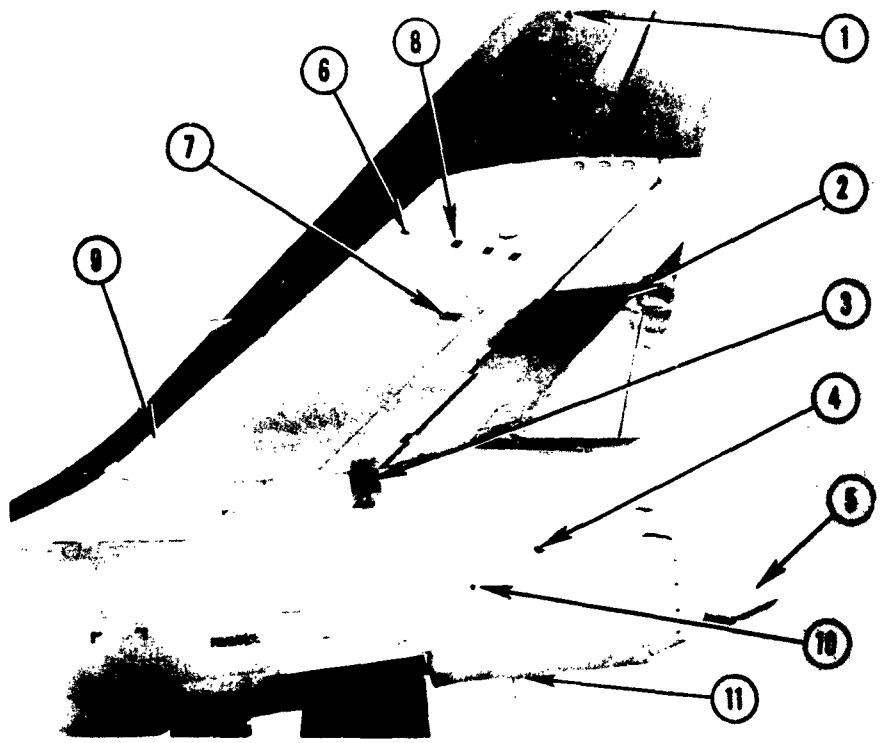

Figure 2.4 Sensor locations in the empennage area: (1) angle-of-attack indicator, (2) thermal panel, (3) horizontal stabilizer deflection camera and light, (4) elevator ripple camera, (5) ground-zero mount, (6) angle-of-attack transducer, (7) calorimeter, (8) convection calorimeter, (9) strain-gage bridges, (10) overpressure gage, (11) vertical mount.

reference panel was used to obtain data for the study of strain-gage error caused by the nonuniform temperature distribution across a strain-gage rosette mounting.

The buckle deflection of the elevator's lower skin, induced by thermal loads, was measured by two deflection indicators. The deflection indicators consisted of two spring-loaded linear potentiometers directly actuated by the buckling movement of the skin. These potentiometers made contact with the smallest possible area of the skin surface in order to minimize heat transfer from the panel. Two N-9 cameras were installed at Fuselage Station 1248.0 to photograph the instrumented panel deflection on each elevator.

Strain-gage bridges were installed at the root and mid-span of the left wing, at the three-quarter span of the right wing, at two fuselage stations, and at the roots of the horizontal stabilizer for the purpose of measuring bending moment, shear, and torsion. Thirteen bridges each were installed at Left Wing Station 144.0 and 493.0 on the front and rear spars and upper skin. Eight bridges were installed at Right Wing Station 615.0 on the front and rear spars. Fourteen

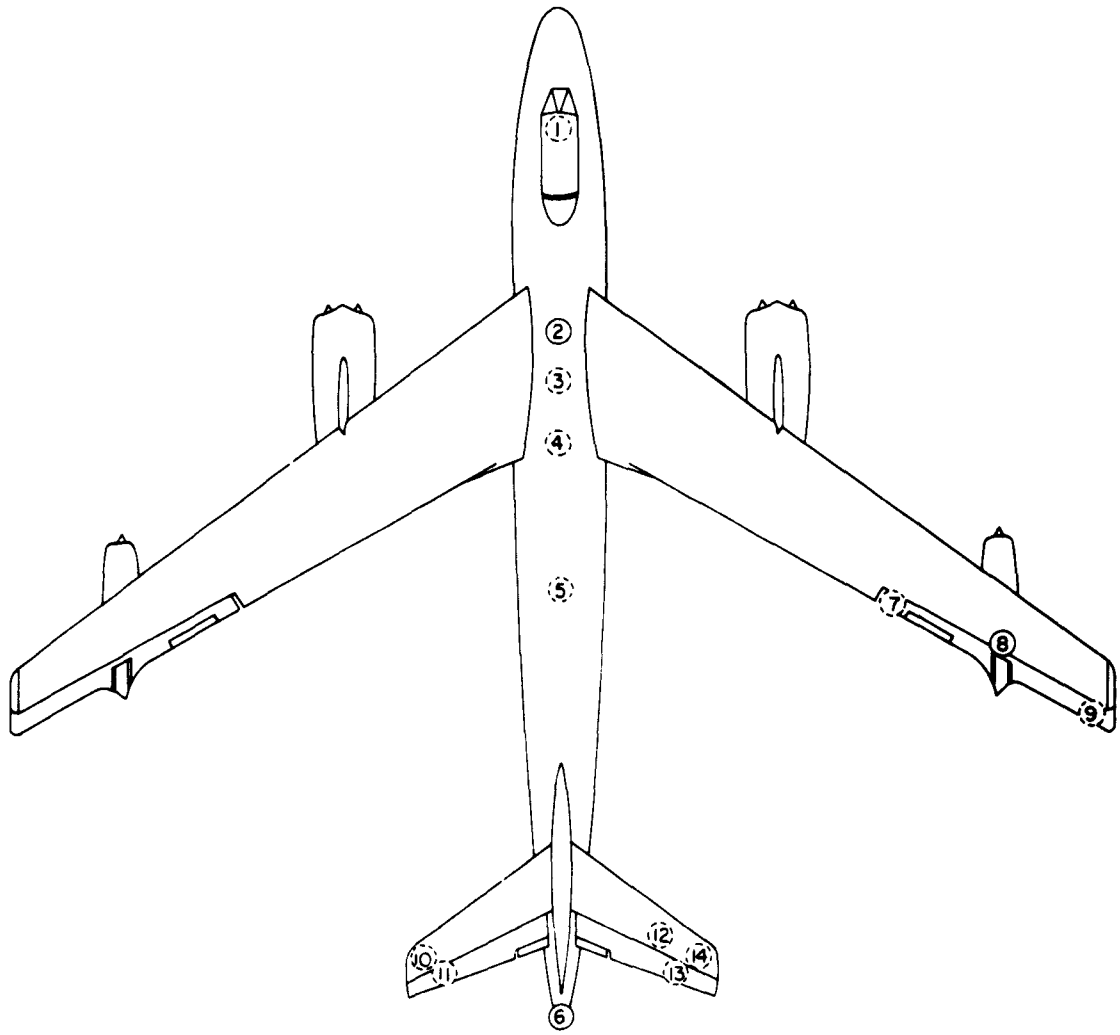

①	RADOME	⑧	#6 ENGINE
②	OPTIGRAPH MOUNT	⑨	RIGHT AILERON
③	BOMB BAY DOOR	⑩	LEFT STABILIZER
④	CENTRAL RECORDING ASSEMBLY	⑪	LEFT ELEVATOR, THERMAL PANEL
⑤	BOMB BAY DOOR	⑫	RIGHT STABILIZER
⑥	GROUND ZERO MOUNT, REFERENCE PANEL	⑬	RIGHT ELEVATOR, THERMAL PANEL
⑦	RIGHT AILERON	⑭	RIGHT STABILIZER

Figure 2.5 General location of thermocouple installations on the aircraft.

and 17 bridges were installed at Fuselage Stations 800.0 and 1044.0, respectively, on the longerons and skin. Nineteen bridges were installed at Left Stabilizer Station 22.0, and 15 bridges were installed at the same station on the right stabilizer. The stabilizer bridges were located on the main spar, leading edge, and upper skin. A complete description of the gust-load instrumentation is given in Reference 8.

2.2.4 Overpressure Measurements. Overpressure measurements used in the determination of the magnitudes of gust inputs were made at five locations on the fuselage of the aircraft. One of these was in the lower fuselage (forward wheel well) at Station 292.0. The remaining four were located at Fuselage Station 1227.0 in a ring about the fuselage. Transducers comprising the rear ring were positioned as follows: one at the base of the vertical fin at 1 o'clock; a second on the right side of the fuselage at 3 o'clock; a third on the lower surface of the fuselage at 6 o'clock; and a fourth on the left side at 9 o'clock.

Transducers installed on the lower surface of the fuselage were positioned to permit evaluation of shock-front incidence angle. The remaining three transducers were installed primarily for the measurement of overpressure magnitude. Additional pressure transducers were installed on the aircraft ram and static systems to permit monitoring of the gust effects upon these installations.

2.2.5 Engine Effects. A total of eight channels of pressure and temperature information were recorded on Engine No. 6 to evaluate changes in the operational characteristics of the GE-J47-25 engine due to gust effects. These measurements consisted of compressor inlet pressure (CIP), compressor discharge pressure (CDP) and temperature (CDT), small slot fuel pressure (SSFP), tail-pipe pressure (TPP), and exhaust gas temperature (EGT) as shown in Figure 2.6.

Three ram-pressure measurements were made at the inlet (CIP) by means of differential pressure transducers referenced to ram pressure prior to shock arrival. The pressure probes were located peripherally at the inlet (partially shown in Figure 2.6). A pressure probe and a thermocouple probe were installed in Fuel Nozzle Assembly Nos. 2, 4, and 7 for the measurement of CDP and CDT. The thermocouples were operated in parallel to obtain the average measurement of CDT. Pressure probes were manifolded to a differential pressure transducer to obtain one average measurement of CDP. Four probe-type thermocouples (CDT) were projected into the tail pipe at equiangular locations. These were connected in parallel in order to obtain the average tail-pipe temperature. SSFP and TPP measurements were made by means of absolute pressure transducers. Percent of rated engine speed was photographically recorded from a tachometer indicator.

2.2.6 Acceleration. Acceleration of the aircraft fuselage produced by the gust inputs was measured by one angular and three linear accelerometers placed at the aircraft center of gravity. These transducers were oriented as described in Section 2.1.6. The vertical accelerometer was installed at Fuselage Station 570.0, while the longitudinal and lateral units were installed at Fuselage Station 573.0. The angular accelerometer was installed at Fuselage Station 560.0.

2.2.7 Rate of Pitch. Rate of aircraft attitude change about the pitch axis was recorded by means of a rate gyro located as closely as possible to the center of gravity of the aircraft. The instrument was located at Fuselage Station 573.0.

2.2.8 Shock Velocity. The direction of the shock-wave-velocity vector in the plane of the vertical and longitudinal axes of the aircraft was determined by measurement of transit time for the shock wave over the aircraft fuselage. Pressure transducers were located in the aft fuselage at Station 1227 and the forward fuselage at Station 292. The time interval between the recording of the pressure change at the shock front by these transducers divided into the distance between the transducers was the propagation velocity relative to the aircraft along the line of flight. This

relative propagation velocity added to the aircraft velocity formed the hypotenuse of a right triangle, one of whose sides was equal to the shock-wave velocity. The angle between this side and the hypotenuse could then be calculated.

2.2.9 Angle-of-Attack Indicators. An angle-of-attack indicator, Model L-30, manufactured by Specialties Inc., was installed on the left side of the vertical fin. This instrument operated on a difference in pressure existing between the upper and lower surfaces of its sensing probe. This difference in pressure caused a rotation of the probe in the direction of the relative wind,

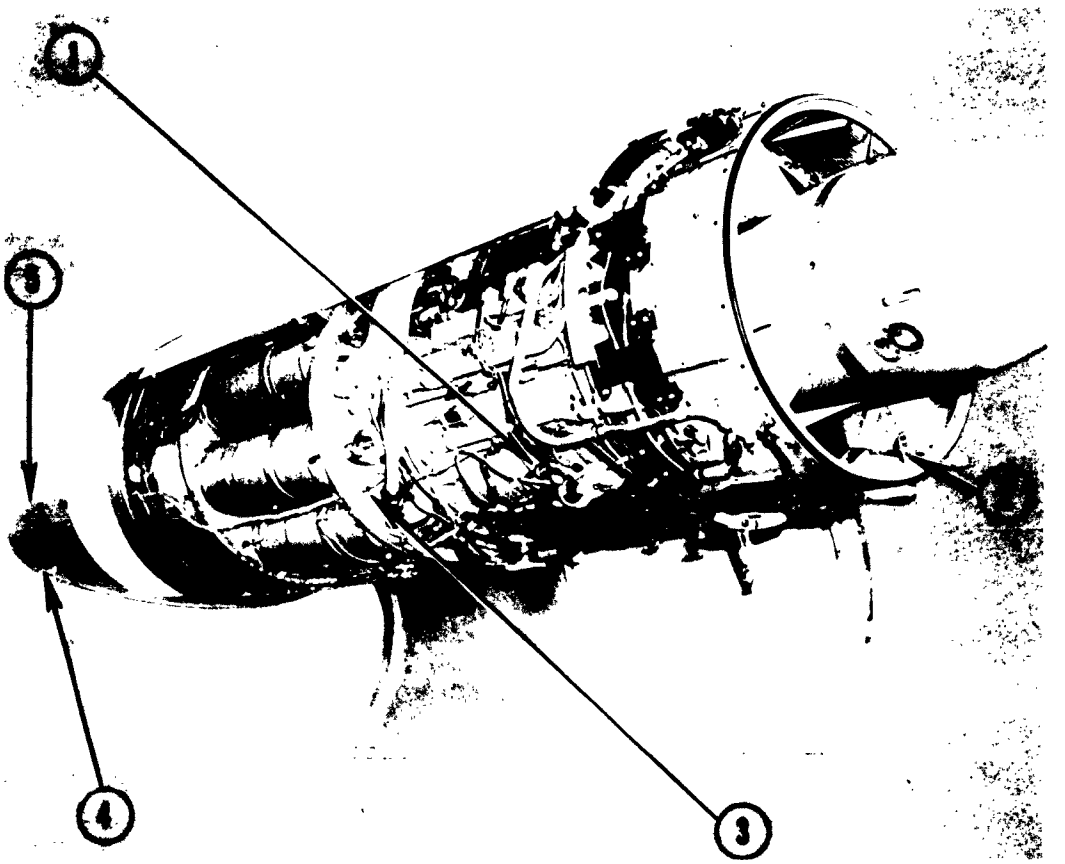

Figure 2.6 Location of instrumentation on No. 6 engine: (1) small-slot fuel pressure; (2) compression inlet pressure, 3 probes; (3) compressor discharge pressure and temperature; (4) exhaust gas temperature, 4 probes; (5) tail-pipe pressure, 1 wall-static probe.

thus causing a corresponding change in potentiometer output in proportion to the change in angle of attack. Range of operation of this instrument was ±15 degrees.

In the horizontal stabilizer, a Statham Type P-69-1D-350 pressure transducer was installed to measure the differential pressure between the upper and lower surfaces of the forward section of the stabilizer (Figure 2.4). Installation of the transducer was such that one side of the transducer was connected to an orifice in the upper skin surface while the other side was coupled to an identical orifice in the lower skin surface.

2.2.10 Control Surface Position Indicators. Giannini Type 85175A potentiometers formed the sensing elements of the rudder, elevator, and aileron position indicators. The potentiometers were coupled through suitable linkages to the control surfaces to provide coupling ratios of one to one for the elevator and aileron surfaces and a ratio of two to one for the rudder surface. Each potentiometer was a three-turn unit having a total resistance of 300 ohms for the elevator and aileron and 150 ohms for the rudder installations.

2.2.11 Aircraft Space Positioning and Position Measurement. An accurate record of aircraft positions during the test operation was made with a Raydist tracking system. The equipment (furnished and operated by the Hastings Instrument Company, Hampton, Virginia) consisted of a low frequency transmitter, mounted in the aircraft, which emitted a continuous signal received at four ground stations located in a known relationship to one another. Three of the ground stations transmitted phase information received from the aircraft transmitter to the fourth station. At the fourth, or master station, the signal was combined with phase information received directly from the aircraft for measurement of the aircraft position.

The aircraft radar and navigational equipment was utilized for in-flight positioning and as a backup position recorder for the Raydist system. The array of indicators on the navigator's instrument panel was photographically recorded. These data included true air speed, K-system air speed, altitude, free-air temperature, compass heading, time, sighting angle, and azimuth. In addition, the aircraft radarscope cameras were used to record position information directly. The data yielded aircraft position versus time information. The location of the camera and panel are shown in Figure 2.1.

A K-17C mapping camera was mounted in the gimbal provided at Fuselage Station 1063.0. The camera, controlled by an intervalometer, operated at a rate of one frame every 3 seconds during the test operation. The ground-zero photos were analyzed to obtain data of approximate aircraft position versus time.

An auxiliary positioning computer (APC) developed and built by Radiation, Incorporated, for USAF, provided an accurate means of positioning the aircraft over a specified target at a predetermined real time. The equipment comprising the system included an ARC-49 receiver and decoder located at Fuselage Station 85.0 and a modified B-2A tracking computer (part of the regular K-4 system on the aircraft). A timing signal received by the ARC-49 from a ground source set the APC into operation. A value of range time was preset into the computer which corresponded to the real time of the received signal. A comparison was then performed mechanically between this real time and the computed time as measured in the K-4 tracking computer. After comparison, this information was displayed on the time-error indicators at the navigator's and pilot's positions. These instruments indicated whether the pilot should increase or decrease speed in order to place the aircraft over an assigned target at the specified time.

2.2.12 Visible Effects, Data Cameras. The effect of shock and gust on the tail section and wing was recorded photographically. Vertical and horizontal stabilizer-surface deflections were recorded on two N-9 cameras. One, in the optigraph canopy of the aircraft at Fuselage Station 446.0, recorded the gross deflection of the entire tail section. The other camera was located in the vertical stabilizer below the horizontal stabilizer at Fuselage Station 1146.0 and photographed both stabilizers simultaneously on the same film frame by means of a mirror-prism assembly. In this manner, relative stabilizer deflection was obtained.

Wing deflections were recorded by one N-9 camera and two Beattie cameras located at Fuselage Station 446.0 (38 percent wing chord) in the optigraph canopy. The Beattie cameras were used to make continuous-line recordings of wing deflection. The N-9 camera was used to provide additional bending deflection information. All the above systems used target lights placed at various locations on the wing and tail assemblies (Reference 8).

2.2.13 Camera Frame-Time Correlation. A 16-mm movie camera was installed in the right chaff compartment to photograph a panel on which counters (actuated by switches in the thermal-

and-gust-effects cameras) were mounted. Time correlation was obtained from a timer clock mounted on the same panel. A time-zero signal was obtained from a light triggered by a selenium type photocell actuated by light from the detonation. Time zero was also indicated by direct detonation light through a small aperture in the counter panel. Roll and pitch were indicated by a free gyro.

2.3 CALIBRATION

2.3.1 Calorimeters and Radiometers. Calibrations for these instruments were obtained from the Naval Radiological Defense Laboratory (NRDL). Channel sensitivity calibrations (mv/in) were made with an accurate mv source contained in the instrument test set developed by Cook Research Laboratories (Reference 9). Millivolt-per-inch deflection calibrations were made before each shot.

2.3.2 Thermocouples. Millivolt-per-inch deflection calibrations were made for all temperature channels before each shot. These calibrations were made with the instrument test set and used in conjunction with standard thermocouple tables for conversion from mv to temperature rise.

2.3.3 Strain Gages. The strain sensitivity (magnitude and sense) of strain gages used to measure thermal loads was evaluated by the use of known parameters of the data channel to determine magnitude and the application of point loads to determine sense. This type of calibration was made necessary because the desired measurement was strain at a point and not a dynamometer type of indication of external force, e.g., load-cell applications. Consequently, the strain response of each gage had to be determined individually, and the direction of galvanometer trace deflection had to be related to compression or tension through the application of point loads (or some similar technique) which would induce a known strain of either sign. Loads applied to the trailing edge of the elevator were used to calibrate gages on the upper and lower elevator skin and on the ribs. Loads applied to the main elevator spar were used to calibrate the gages and rosettes on this spar. Loads applied to a small area in the center of each skin rosette were used as a check (on these gages) of the main load calibration.

Since the gages used for the thermal loads measurements were Q gages, another type of calibration check was used. As stated in Section 2.1.4, the Q gage measures elongation strain; therefore, since aluminum exhibits a positive temperature coefficient of expansion, measurements made at two different temperatures of the structure could be used to evaluate sense. Two methods of obtaining a temperature difference were employed. The first consisted of balancing all channels on the ground and recording the differential deflection with the aircraft in flight at a high altitude. The differential change in temperature from ground to air could be used to evaluate sense. Elongation strain produced by a temperature difference of 100 F was approximately 1,300 μin/in. This was assumed large in comparison with elongation strain produced by air loads on a nearly neutral elevator in level flight. The second method consisted of a simplification of the above, in which the data channels were balanced during the heat of day and a differential deflection record taken at a stabilized, lower, night temperature.

The magnitude of the elongation strains was evaluated by the following relationship:

$$\epsilon = \frac{\delta_{act}}{\delta_{cal}} \left(\frac{R}{R_s N K_s} \right) \qquad (2.1)$$

Where: ϵ = elongation strain, in/in
δ_{act} = galvanometer deflection during shot, inch
δ_{cal} = galvanometer deflection due to shunting one arm of bridge, inch
R = shunted bridge arm resistance, ohms
R_s = shunt resistance, ohms
N = number of active bridge arms
K_s = manufacturers calibration gage factor

Actual stress-producing strain was determined from elongation strain by using a corrective procedure developed empirically by laboratory techniques.

The point-load system of calibration was employed in the calibration of the gust-load strain gages (Reference 10). The data obtained from the point-load application were used to determine shear, bending moment, and torsion equations at the instrumented stations (Reference 11). All bridge outputs were recorded individually, and the data were combined analytically after the test operation. Periodic check loads of 2,500 pounds were applied at outboard wing and stabilizer stations to check the three types of load equations at the instrumented stations.

2.3.4 Pressure Systems. Pressure transducer calibrations were performed on all units before and after their installation in the aircraft. The first calibration, performed in the laboratory, consisted of a detailed calibration to insure that all transducers were linear and that their outputs agreed with the information supplied by the manufacturer. The second calibration, performed in the field, consisted of a check of the transducers, including the electrical system used in recording their outputs during test. Both calibrations were accomplished by the application of known pressures in several steps throughout the range of the instruments and recording the corresponding outputs. In the laboratory calibration, an L & N potentiometer bridge was used to record the outputs of the gages, instead of the oscillograph used in the field calibrations. Pressures applied were measured by means of water or mercury manometers, depending upon the range of the transducer undergoirg calibration.

2.3.5 Accelerometers. Like the pressure transducers, the accelerometers were calibrated in the laboratory, as well as in the field. The laboratory calibration consisted of complete calibration and check, by the use of a spin table, to supply the necessary g forces for static and dynamic inputs. During this process, inputs were applied in steps throughout the range of each instrument, while the electrical outputs were recorded by means of an L & N potentiometer bridge. In the field, each accelerometer was given a static check of +1.0 g, 0.0 g, and −1.0 g to verify the laboratory data and to check operation through the recording system installed in the aircraft.

2.3.6 Rate Gyro. The rate gyro installed for the measurement of pitch rate was given a complete laboratory calibration prior to installation in the aircraft. The procedure followed was similar to that used in the tests on accelerometers, with the exception that a low-speed spin table capable of operation in both directions was used. Inputs in terms of degrees per second were applied in steps throughout the range of the gyro. Outputs were recorded by means of an L & N potentiometer bridge, while table speed was measured by the use of elapsed time techniques.

2.3.7 Time-Interval Equipment. The accuracy of time-interval measurement required in these tests was ± 100 μsec. No calibration other than operational checks was required, since the units had self-contained, crystal-controlled 100-kc oscillators (10 μsec per cycle).

2.3.8 Control Surface Sensors. Position indicators installed on the rudder, elevator, and aileron were calibrated in the field by the movement of the control surfaces through their ranges of deflection and the recording of the electrical outputs at various angular deflections. Deflections of the rudder were measured by a rudder protractor designed by the airframe manufacturer. The remaining control surface deflections were measured by the use of a clinometer. Electrical outputs were recorded through the instrumentation installed in the aircraft.

2.3.9 Angle-of-Attack Indicator. Calibration of the angle-of-attack indicators was performed after their installation in the aircraft. The instrument installed in the vertical stabilizer was calibrated by the rotation of the probe through its range of operation and the recording of the

electrical outputs for various angular deflections. The differential pressure type of angle-of-attack indicator installed in the horizontal stabilizer was calibrated pressure-wise and converted to angle of attack analytically. In both the above cases, the outputs were recorded by the use of the instrumentation system installed in the aircraft.

2.3.10 Aircraft Instruments. With the exception of K-system true air speed, no calibration of the aircraft's instruments was made, since normal instrument accuracy was all that was required. True air speed was calibrated with a standard K-system 180-degree wind run.

Chapter 3
OPERATIONS

Planning for the participation of the B-47E aircraft in Operation Redwing was initiated during the early part of 1955.

Certain modifications had to be made to the aircraft to accommodate instrumentation and its maintenance. To insure safety of flight, certain parts of the aircraft vulnerable to effects of radiant exposure, such as the elevator balance seal, drains, and internal sections, were shielded or painted with low-absorptivity paint. Thermal curtains made of heavy white cotton duck backed with aluminized vinyl were placed over the canopy and navigator's windows. The curtains were necessary only during the thermal phase of the detonation and were, therefore, designed for rapid installation and removal.

At the completion of the installation-and-calibration stage of the project, the aircraft was flown in test flights in the continental United States to check the response characteristics and operation of the instrumentation. Upon arrival at the EPG on 12 March 1956, the B-47E was again flown on test and practice missions to develop air crew proficiency and in-flight calibration of certain equipment. A flight plan was chosen which would facilitate positioning of the aircraft at a point in space at a predetermined time. This plan was followed on all test participations.

3.1 SHOT PARTICIPATIONS

In making a choice of shot participations, it was necessary to evaluate various positioning factors as related to the limiting criteria set forth in Chapter 1 and to select the combinations of gust and thermal effects which would satisfy the objectives of the project. The choice of shot participations, as well as positioning criteria, are shown in Table 3.1. These criteria were established by such studies as the one presented in Reference 6.

For Shots Cherokee, Navajo, and Tewa, the limiting parameter was the radiant exposure necessary to cause a temperature rise of 400 to 500 F on numerous portions of the aircraft simultaneously. However, on Shot Tewa, the aircraft was also positioned for gust effects at the sacrifice of the elevator thermal-strain data. On Shots Zuni, Dakota, and Apache, the gust effects were the limiting factors, and test panels were painted so that the resulting temperature rises would be high enough to cause buckling in the thin-skinned test panels. The position of the aircraft on Shot Flathead was such that the predominant effects would be overpressure and gust. During Shots Huron and Mohawk, the aircraft was positioned to obtain side loads. No thermal effects were anticipated.

3.2 FLIGHT PLANS

Because of the excessive amount of aircraft traffic handled at Eniwetok, the operational plan had to be executed with considerable emphasis on time. Also, because of the need to be at a specified position in space at a predetermined time, the time correlation of the operational plan was given more emphasis than would be necessary on an actual bombing mission. The typical flight plan used during Operation Redwing is shown in Figure 3.1, and flight conditions existing for each shot are presented in Table 4.1. The aircraft was flying away from ground zero at time zero on all shots except Mohawk and Huron, when the aircraft was positioned for side loads. The flight plan shown in Figure 3.1 was chosen by the aircraft commander and was used on all tests of the operation. This plan made it possible to establish with considerable accuracy wind

TABLE 3.1 SHOT PARTICIPATION AND PREDICTED RESULTS

Shot	Limit Moment Wing Station 493.0	ΔP	ΔT	Aircraft Surface and Absorptivity
	pct	psi	F	
Cherokee	56	0.38	450	Aileron 0.24
			498	Elevator 0.30*
Zuni	58	0.42	630	Elevator 0.81*
Flathead	95	0.30	Negligible	—
Dakota	90	0.71	590	Elevator 0.96*
			710	Aileron 0.96
Mohawk	65†	0.31	Negligible	- -
Apache	67	0.57	720	Elevator 0.96*
Navajo	95	0.86	700	Aileron 0.48
			400	White Aileron 0.21
Tewa	90	0.83	505	Aileron 0.51
			Negligible	White Aileron 0.21
Huron	69†	0.39	Negligible	—

* Elevator; temperature rise in approximately 65 percent of left elevator lower surface.

† Side loads; represents percent fuselage bending.

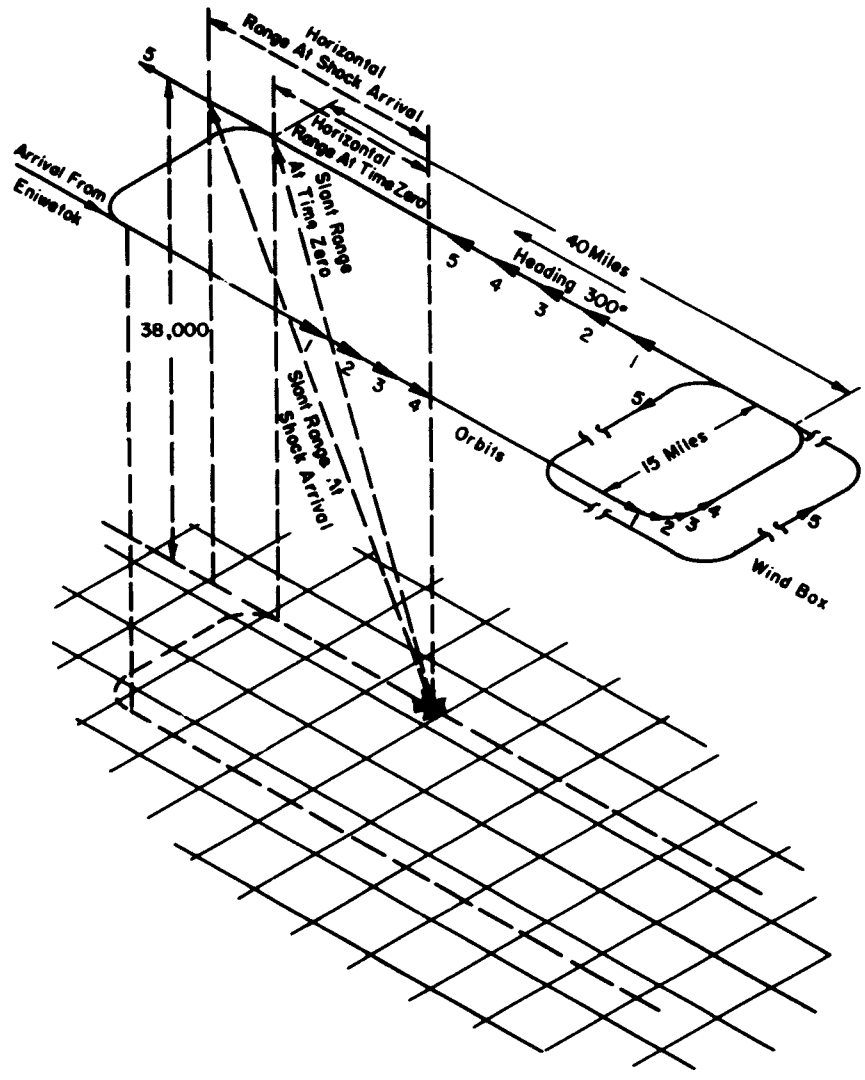

Figure 3.1 Typical flight pattern.

velocity, true air speed, and such other navigational data as were necessary for the execution of given time-position requirements. This was important to the analysis associated with overpressure, gust, and thermal effects.

The typical flight pattern consisted of four timing runs followed by a wind box. Each of the timing runs was a race-track pattern with two approximately 40-nautical-mile legs and two 3-minute turns. The turns were executed with one 90-degree turn followed by a 1-minute leg and then another standard 90-degree turn. The time correlation on the final run was computed accurately the auxiliary positioning computer (APC), which compared real time with time to the desired point in space from the K-4 system. The results of the comparison were presented to both the pilot and navigator on a panel indicator in terms of seconds late or early along the path.

Chapter 4
RESULTS

The results presented herein were derived principally from data which were recorded on oscillograph paper and film within the aircraft. The data were reduced both manually and with semiautomatic data-reduction equipment. A time-history presentation of all recorded data has been made in Reference 12. Significant results for each measured parameter are included herein.

4.1 OPERATIONAL RESULTS

The standard flight plan was flown using the aircraft K system with tracking accomplished by Raydist navigation equipment. Intended and actual aircraft range relative to ground zero appear as part of Table 4.1. The aircraft was tracked successfully by Raydist during Shots Cherokee, Flathead, Dakota, Navajo, and Tewa. For those cases in which Raydist data were not available, it was necessary to use auxiliary sources. These sources were the two photo panels, a mapping camera, cameras aimed at ground zero, and the K system.

Other recorded flight operational results such as speed, heading, wind vector, etc., also appear in Table 4.1. Position yield, design yield and actual yield have also been incorporated in Table 4.1 for convenience, even though they are independent of aircraft operations. Meteorological data for all flights are presented in Table 4.2.

4.2 THERMAL INPUT

Values of peak irradiance and total radiant exposure obtained from radiometers and calorimeters are summarized in Table 4.3. These values were obtained by using a data reduction procedure as prescribed by NRDL. This procedure corrected the data for the change in thermal emf of the thermocouple and the heat capacity of the receiver as a function of temperature. For the calorimeters, the NRDL procedure also corrected the data for the heat loss of the particular instrument. Further corrections for transmission losses because of filter and for angle of incidence of incoming energy have been made in applicable cases for Table 4.3.

Time-history plots of irradiance, radiant exposure, and temperature rise in the reference panel (Figure 2.2) are presented in Figure 4.1. The data are from Shot Dakota and show the expected relation of these quantities.

Two calorimeters were used to determine the effect of paint on the transmission of radiant energy through the plastic radome. One calorimeter received energy through the honeycombed material painted white (absorptivity, 0.2) while the other viewed through the natural finish of honeycomb (absorptivity, 0.7). Results from three tests showed the painted area reduced transmission of radiant energy by 65, 60, and 53 percent, as would be expected.

Scatter measurement of radiant exposure was made by a calorimeter mounted perpendicularly to a ray from ground zero. This instrument measured extremely small outputs, ranging from 0.08 to 0.69 cal/cm^2, when measurable. It was significant that these exposures fell in the rather limited range of 2.1 to 2.6 percent of the total radiant exposure looking directly at the detonation.

4.3 THERMAL RESPONSES

4.3.1 Temperature Rise. A summary of temperature rises for various skin thicknesses and the outer radome laminate is presented in Table 4.4. The absorptivity and angle of incidence of

TABLE 4.1 SUMMARY OF OPERATIONAL RESULTS

		Cherokee	Zuni	Flathead	Dakota	Mohawk	Apache	Navajo	Tewa	Huron
Horizontal range, 10^3 ft	Intended	31.9	31.5	3.5	10.1	51.0	28.0	22.9	28.5	47.2
(time zero)	Actual	53.8	32.5	3.4	10.4	51.0	29.0	33.3	25.6	46.0
Horizontal range, 10^3 ft	Intended	86.2	87.2	32.0	30.0	40.0	73.7	55.5	66.4	38.0
(shock arrival)	Actual	156.7	82.5	33.3	29.4	42.3	79.5	88.9	69.6	39.0
Slant range, 10^3 ft	Intended	45.9	44.2	38.2	26.0	62.8	41.0	41.0	45.1	52.1
(time zero)	Actual	63.4	44.9	38.2	26.2	62.8	41.8	47.5	42.7	51.0
Slant range, 10^3 ft	Intended	92.3	92.5	49.7	38.4	54.3	79.6	65.1	75.1	43.9
(shock arrival)	Actual	160.2	88.1	50.5	38.0	56.2	85.0	95.1	77.5	44.8
Ground speed, ft/sec	Intended	747	770	747	733	750	773	759	757	708
(time zero)	Actual	752	750	716	724	786	745	783	780	744
Ground speed, ft/sec	Intended	747	770	747	733	750	773	759	757	708
(shock arrival)	Actual	768	754	724	724	779	745	774	763	727
True air speed, ft/sec	Intended	747	770	747	733	750	773	759	757	708
(time zero)	Actual	758	756	725	726	743	752	794	788	727
True air speed, ft/sec	Intended	747	770	747	733	750	773	759	757	708
(shock arrival)	Actual	776	760	733	726	736	752	785	771	710
True heading, deg	Intended	294	250	300	270	020	320	270	270	000
(time zero)	Actual	293	257	303	271	019	324	263	269	004
True heading, deg	Intended	294	250	300	270	020	320	270	270	000
(shock arrival)	Actual	286	252	303	271	018	324	260	269	002
True course, deg	Intended	294	250	300	270	020	320	270	270	000
(time zero)	Actual	296	258	306	272	021	325	264	269	003
True course, deg	Intended	294	250	300	270	020	320	270	270	000
(shock arrival)	Actual	289	253	306	272	020	325	261	269	001
Bearing to ground zero, deg	Intended	180	180	180	180	308	180	180	180	302
(time zero)	Actual	157	173	167	179	306	178	180	181	300
Bearing to ground zero, deg	Intended	180	180	180	180	270	180	180	180	270
(shock arrival)	Actual	177	181	182	180	265	180	183	180	266
Time of shock arrival, sec	Intended	73	72	38	27	42.5	51.9	43	50	35.5
	Actual	138.44	66.87	41.48	26.95	44.10	67.82	71.15	57.02	36.60
Altitude above ground zero, 10^3 ft	Intended	33.0	31.0	38.0	24.0	36.7	30.0	34.0	35.0	22.0
	Actual	33.0	31.0	38.0	24.1	36.7	30.05	33.8	34.2	22.15
Altitude above MSL, 10^3 ft	Intended	38.0	31.0	38.0	24.0	37.0	30.0	34.0	35.0	22.0
	Actual	38.0	31.0	38.0	24.1	37.0	30.05	33.8	34.2	22.15
Pitch attitude at time zero, deg		3.0	2.5	3.0	1.5	2.0	1.5	1.0	3.0	2.0
Roll attitude at time zero, deg		2*	0	0	0	0	0	0	0	0
Gross weight, kips (Intended, 115.0 kips)		113.0	115.0	120.3	114.8	112.8	114.3	114.3	115.2	117.4
Center of gravity location, pct MAC (Intended, 25 pct)		24	20	21	20	18.9	21.5	21.4	21.3	18.9
Yield, Mt	Position	6.0	5.0	0.70	0.85	0.70	5.0	10.0	15.0	0.30
	Design	4.5	2.0	0.40	0.80	0.50	4.0	7.0	7.0	0.25
	Actual	3.8	3.5	0.38	1.15	0.35	1.9	4.8	5.0	0.27

* Left roll.

TABLE 4.2 METEOROLOGICAL DATA

NA, not available.

Shot	Ambient Temperature at Sea Level	Ambient Pressure at Sea Level	Visibility at Sea Level	Water Vapor Pressure at Sea Level	Ambient Temperature at Aircraft Altitude	Ambient Pressure at Aircraft Altitude	Wind Speed and Direction at Aircraft Altitude	Cloud Cover		
								Fraction of Sky Covered	Type *	Altitude
	F	psi	miles	mm Hg	F	psi	deg/fps			$\times 10^3$ ft
Cherokee	81.0	14.634	10+	NA	−58.0	3.26	210/37	2/10	C	1.8
								2/10	CR	38
Zuni	81.0	14.656	8	NA	−24.3	4.47	205/10	4/10	AC	8.0
								6/10	AS	17
								4/10	CR	25
								6/10	CS	35
Flathead	82.0	14.691	10	21.6	−54.0	3.29	230/42	4/10	SC	2.0
								10/10	CS	30
Dakota	82.0	14.636	10	22.8	−1.3	5.93	190/17	3/10	AS	12
								7/10	CS	35
Mohawk	79.6	14.652	10	21.4	−50.8	3.48	230/50	1/10	C	1.3
								1/10	SC	4.8
								10/10	AS	6.5
Apache	80.3	14.656	10+	22.1	−22.7	4.68	270/12	2/10	C	1.5
								2/10	SC	2.0
								3/10	CS	30
Navajo	81.2	14.652	10	21.6	−39.8	3.94	205/20	2/10	C	1.8
								6/10	C	2.0
								7/10	CS	30
Tewa	82.0	14.639	10+	NA	−42.2	3.89	270/8	2/10	C	2.0
								1/10	CS	30
Huron	81.4	14.617	10	NA	+11.8	6.50	155/19	3/10	C	1.8
								10/10	CS	30

* Cloud cover type legend: C, cumulus, AS, altostratus, CS, cirrostratus, AC, altocumulus, SC, stratocumulus, and CR, cirrus.

TABLE 4.3 THERMAL RADIATION

Numbers in parentheses are fields of view of instruments in degrees. NA, not available. NR, not reducible.

Shot	Irradiance		Radiant Exposure, cal/cm²						
	Peak Value	Peak Time	On Horizontal Plane *		On Plane Normal to Ray from Detonation				
			Predicted †	Measured (160)	Predicted †	Measured (21)	Measured (45)	Measured (90)	Measured (160)
	(cal/cm²)/sec	sec							
Cherokee	4.51	2.03	16.8	10.19	22.1	NR	NR	16.37	17.71
Zuni	8.40	1.87	17	21.28	22.40	18.58	26.40	31.17	30.78
Flathead	3.16	0.68	5.25	3.64	NA	2.16	2.41	3.85	3.93
Dakota	13.29	1.10	27	21.20	30.3	20.39	23.38	27.86	26.32
Apache	5.76	1.38	11.8	9.03	15.1	11.09	12.54	13.56	12.94
Navajo	8.51	2.09	21.8	20.69	26.3	8.12	26.62	33.19	33.15
Tewa	10.29	2.09	33.5	24.46	38.1	NR	31.15	33.58	32.79

* Measured values of thermal energy incident on horizontal plane are naturally not corrected for angle of incidence. All other measured values are corrected.

† Predicted values based on final yields and aircraft positions.

TABLE 4.4 SUMMARY OF PEAK TEMPERATURE RISE

Data in this table is not applicable to Shots Flathead, Mohawk and Huron. λ - angle of incidence at time zero. α - absorptivity. ΔT - temperature rise, F.

		Cherokee	Zuni	Dakota	Apache	Navajo	Tewa
Elevator Lower Skin *							
Left Elevator Sta. 148.0,	λ	54	43	18	39	39	33
0.025, 24S - T3	α	0.30	0.81	0.96	0.96	0.41	0.36
	ΔT	75	346	547 †	250	210	225
Right Elevator Sta. 148.0,	λ	53	42	18	39	39	33
0.025, 24S - T3	α	0.27	0.32	0.96	0.96	0.42	0.41
	ΔT	58	170	520	266	211	212
Right Aileron							
Trailing Edge Sta. 476.0,	λ	56	45	22	42	42	37
0.020, 24S - T3	α	0.24	0.82	0.96	0.81	0.21	0.21
	ΔT	54	380	480	227	140	156
Trailing Edge Sta. 767.0,	λ	58	46	22	42	43	37
0.020, 24S - T3	α	0.19	0.82	0.81	0.81	0.48	0.51
	ΔT	41	430	432	235	315	315
Right Stabilizer							
Stabilizer Sta. 168.0,	λ	60	49	25	46	46	40
0.064, 75S - T6	α	0.25	0.25	0.20	0.17	0.16	0.17
	ΔT	20	50	50	18	43	44
Stabilizer Sta. 192.0,	λ	60	49	25	46	46	40
0.040, 75S - T6	α	0.23	0.97	0.96	0.96	0.16	0.18
	ΔT	29	328	388	170	82	93
Radome Outer Surface							
Fuselage Sta. 202.0, left	λ	58	42	22	38	37	32
	α	0.22	0.20	0.20	0.24	0.25	0.20
	ΔT	47	120	162	76	148	162
Fuselage Sta. 202.0, right	λ	43	38	21	36	37	33
	α	0.70	0.70	0.70	0.70	0.72	0.70
	ΔT	92	321	387	169	321	322

* Spare elevator used on all shots except Cherokee.

† Average taken from reference panel, (no temperature values available here for this flight).

each surface is included for comparison of data. In all cases, the temperature rise listed was the maximum measured value. Data from Shots Flathead, Mohawk, and Huron are not presented because the aircraft was positioned for gust loading and negligible temperature rises were recorded.

Typical temperature distributions in instrumented structural members and panels under investigation have been prepared to show the relative temperature rises as a function of time.

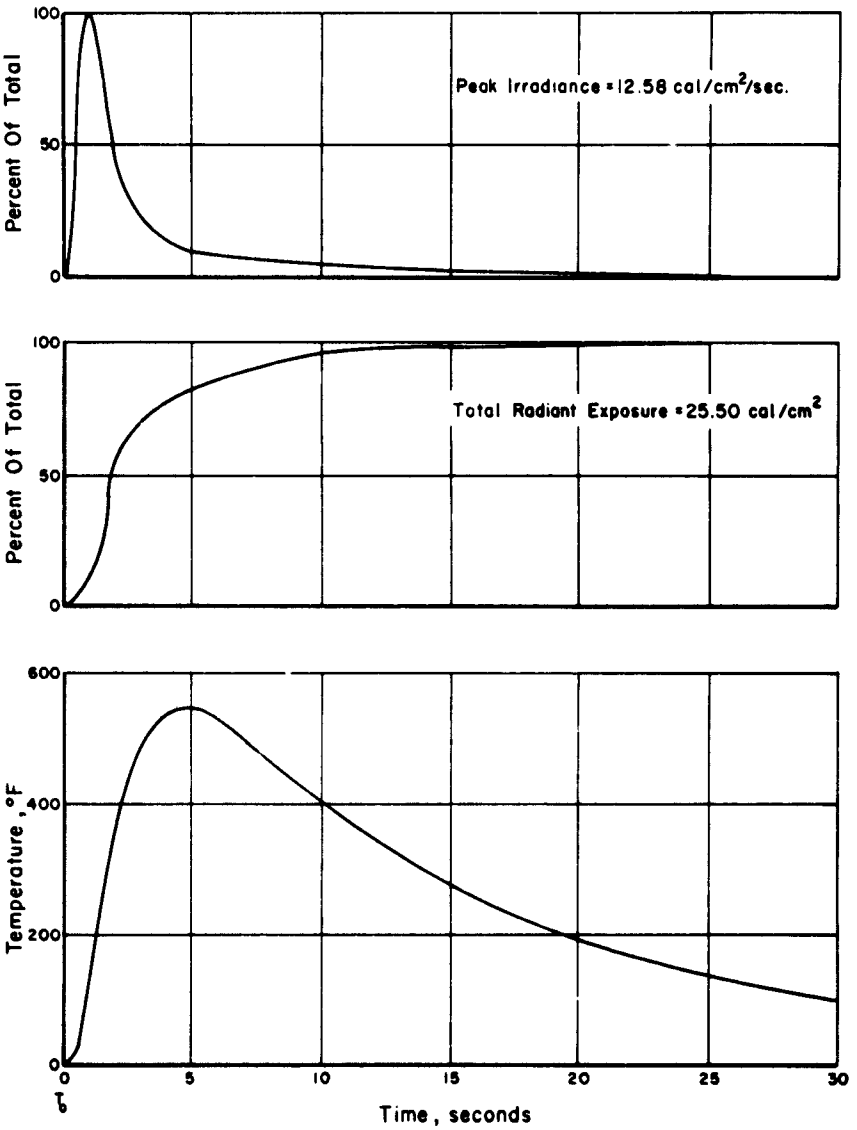

Figure 4.1 Time-history representation of irradiance, radiant exposure, and temperature rise on reference panel, ground-zero mount, for Shot Dakota.

In most cases flight Tewa was used since this event produced the greatest thermal inputs.

Figure 4.2 shows the temperature distribution in the right elevator inboard rib. As was expected, the proximity of the thermocouples to the irradiated surface determined the relative peaks and times to peak of the temperature rises at the rib flange and at the center of the rib.

Figure 4.3 shows the chord-wise temperature distribution in the right stabilizer skin panel for Shot Tewa. In all cases these thermocouples were mounted on 0.040-inch aluminum painted white (absorptivity of $\alpha = 0.18$). The only variable here should be the surface convective cooling coefficient. Since the coefficient of cooling is an inverse function of distance from the leading edge, the more distant points should be expected to rise to the highest temperatures. This is shown to be the case since maximum temperatures (from leading edge aft) were 80 F, 83 F, and 93 F.

Figure 4.4 shows span-wise temperature distributions for the right stabilizer at the same distance from the leading edge and the same skin absorptivity. Temperature rises of 0.064-inch

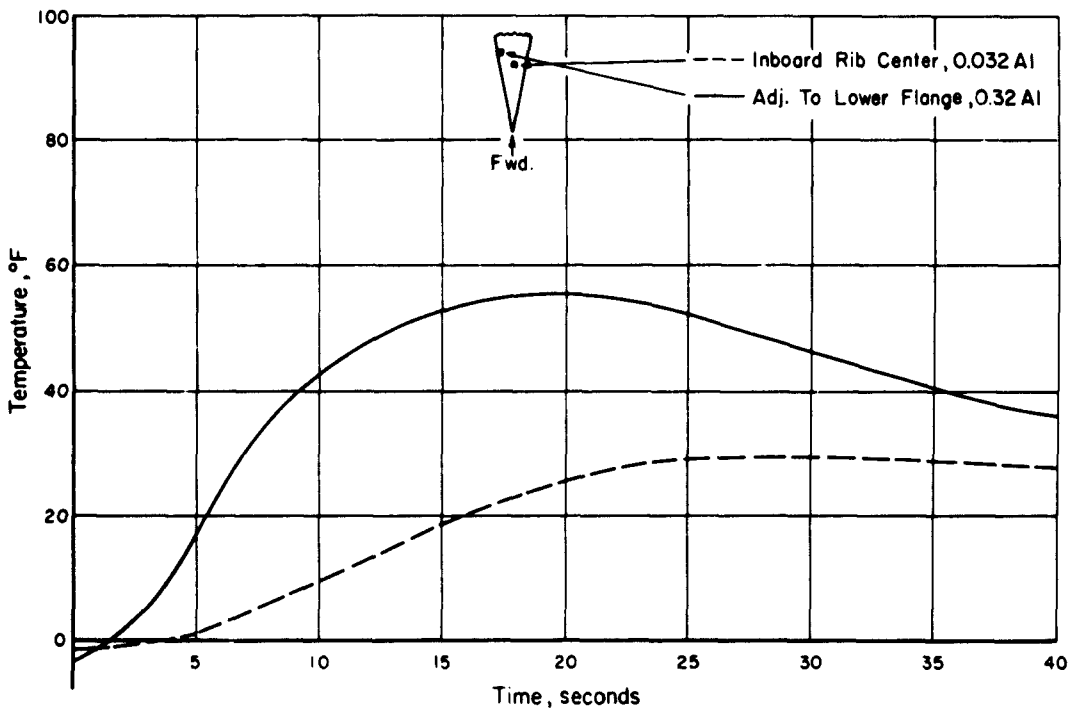

Figure 4.2 Time-history representation of temperature rise on the inboard instrumented rib of the right elevator.

and 0.040-inch aluminum have been compared to show relative temperature rise with skin thickness being the only variable.

Temperature distribution in the radome honeycomb is shown in Figure 4.5. White paint on the surface reduced the temperature rises to less than 50 percent of the temperature rises that existed in the unpainted area.

Temperature distributions in the bomb-bay doors are shown in Figure 4.6. Here a 0.032-inch aluminum panel of the bomb-bay door is compared to a 0.040-inch magnesium panel of the same door. The aluminum panel temperature rose only 92 F as compared to 136 F for the magnesium panel.

4.3.2 Thermal Strain. The elongation strains (total measured strains) of the elevator ribs, front spar and upper skin were corrected for the expansion of aluminum using the temperature provided by adjacent thermocouples. The corrected data thus consisted only of stress-producing strain (due to axial and bending loads). Peak values of this corrected strain are summarized in

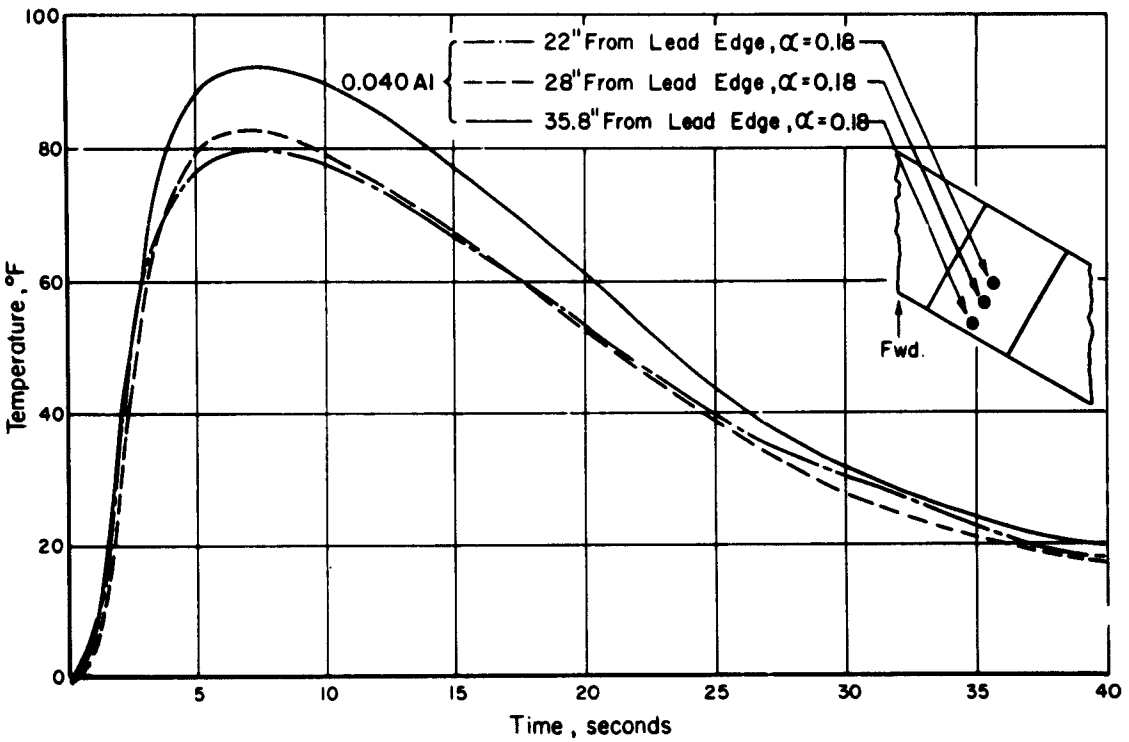

Figure 4.3 Time-history representation of chord-wise temperature distribution on the lower skin of the right stabilizer when painted white.

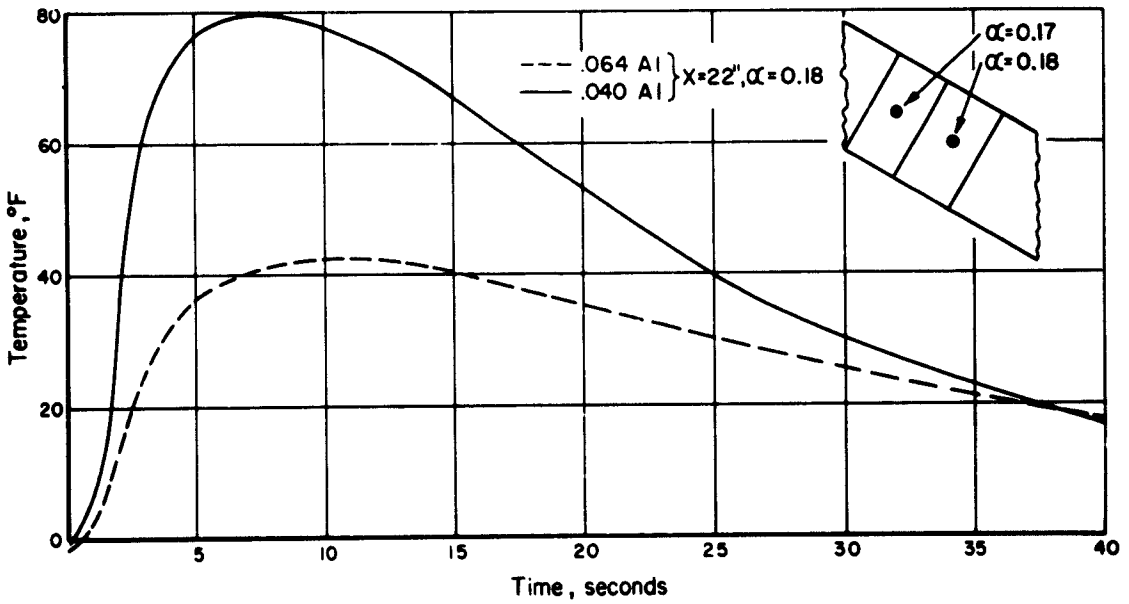

Figure 4.4 Time-history representation of span-wise temperature distribution on the lower skin of the right stabilizer when painted white.

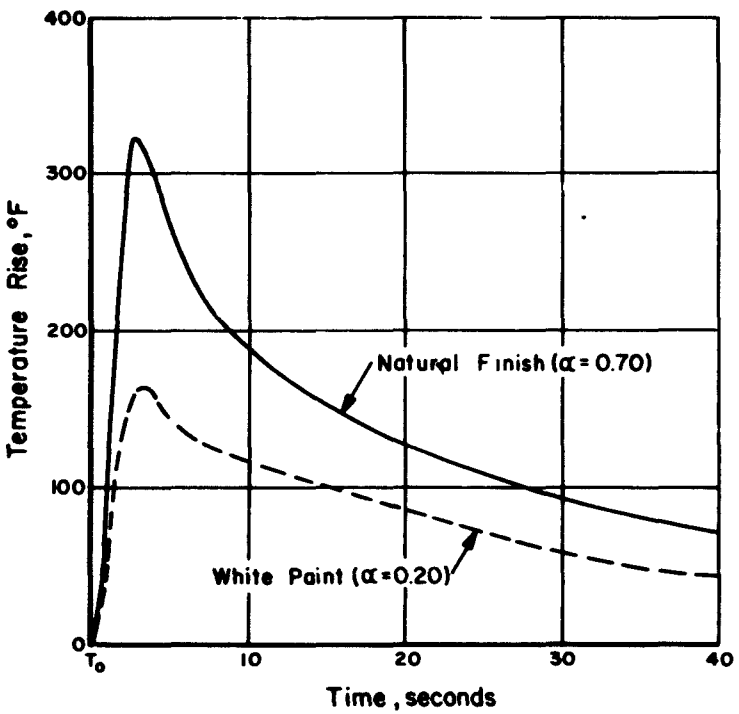

Figure 4.5 Time-history representation of temperature rise on the radome as a function of surface condition.

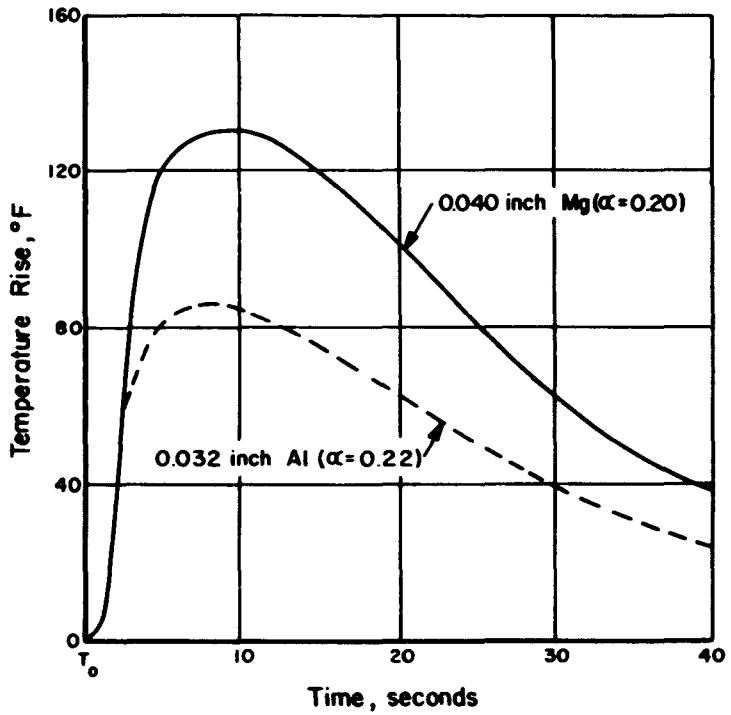

Figure 4.6 Time-history representation of temperature rise on the aluminum and magnesium panels of the bomb-bay door.

Tables 4.5 and 4.6. Peak values of stress-producing strain in the left elevator ribs have been compared with maximum lower-skin temperature rise (Figure 4.7). Since the tension applied to the rib by the heated, expanding skin changed abruptly in the skin-temperature range of 350 to 450 F, this comparison of rib strain versus skin temperature indicated that yield of the skin had

TABLE 4.5 SUMMARY OF PEAK ELEVATOR* STRAINS, CAP MOUNTED GAGES

+ equals tension; − equals compression. NR_e equals data not reducible.

Location	Strain, μin/in				
	Cherokee	Zuni	Dakota	Apache	Navajo
Left Outboard Rib, Upper Cap	+ 120	+ 180	+ 220	+ 80	+ 95
Left Outboard Rib, Lower Cap	NR_e	+ 1,020	+ 980	+ 560	+ 495
Left Inboard Rib, Upper Cap	+ 60	+ 150	+ 212	+ 160	+ 95
Left Inboard Rib, Lower Cap	+ 640	+ 1,650	+ 1,660	+ 1,150	+ 922
Right Inboard Rib, Upper Cap	+ 100	+ 60	+ 160	NR_e	NR_e
Right Inboard Rib, Lower Cap	NR_e	+ 875	+ 1,300	NR_e	NR_e
Left Front Spar, Upper Cap	NR_e	− 200	− 350	− 220	− 120
Left Front Spar, Lower Cap	+ 150	− 540	− 545	+ 320	+ 410
Right Front Spar, Upper Cap	− 20	− 35	+ 127	+ 122	+ 120
Right Front Spar, Lower Cap	+ 160	+ 335	− 635	+ 170	+ 315

* Spare elevator used on all shots except Cherokee.

apparently occurred. Hence, there was little change in rib strain at higher skin temperatures. This also provided evidence that failure of skin occurred before failure of the primary structure.

The strain gages mounted on the elevator lower skin shielded the skin immediately under the gage, thus adversely affecting the temperature of the material instrumented. In order to evaluate the complete correction necessary for this temperature differential effect, in addition to the effect of expansion of the material, similar model tests were conducted at Cook Research Laboratories. Similarity or duplication was achieved in instrumentation, shape, thickness, types of materials, surface paints, and mode of heating radiation. The panels tested were unrestrained in order to obtain direct corrections for all the adverse effects of the thermal load-

TABLE 4.6 SUMMARY OF PEAK ELEVATOR* STRAINS INTERNALLY MOUNTED ROSETTES, (MAXIMUM ARM)

+ equals tension; − equals compression.

Location	Strain, μin in				
	Cherokee	Zuni	Dakota	Apache	Navajo
Left Upper Skin	+ 80	+ 180	+ 155	− 120	− 110
Left Outboard Rib	+ 245	+ 473	+ 450	+ 345	+ 295
Left Inboard Rib	+ 155	+ 1,420	+ 1,610	+ 1,010	+ 840
Right Inboard Rib	+ 350	+ 810	+ 1,200	+ 720	+ 660
Left Front Spar	+ 60	− 190	− 240	+ 115	+ 175
Right Front Spar	+ 72	+ 130	+ 180	+ 115	+ 150

* Spare elevator used on all shots except Cherokee.

ing on the gage readings. Application of these corrections to the field test data provided the stress-producing strains. These peak values for the elevator lower skin are summarized in Table 4.7. High thermal radiation combined with the high absorptivity of the elevator lower skin panel (0.96) on Shot Dakota destroyed the majority of the skin strain gages. Therefore,

elevator lower-skin strain-gage data were not available for Shot Dakota and subsequent shots.

A post-flight Shot Dakota photograph of the left elevator thermal panel (after paint had been removed) is presented in Figure 4.8. This photograph shows the effects of thermally induced loads in thin-skinned sections painted with high absorptivity paint. The residual buckles caused by plastic deformation at the l..gh temperatures are clearly visible.

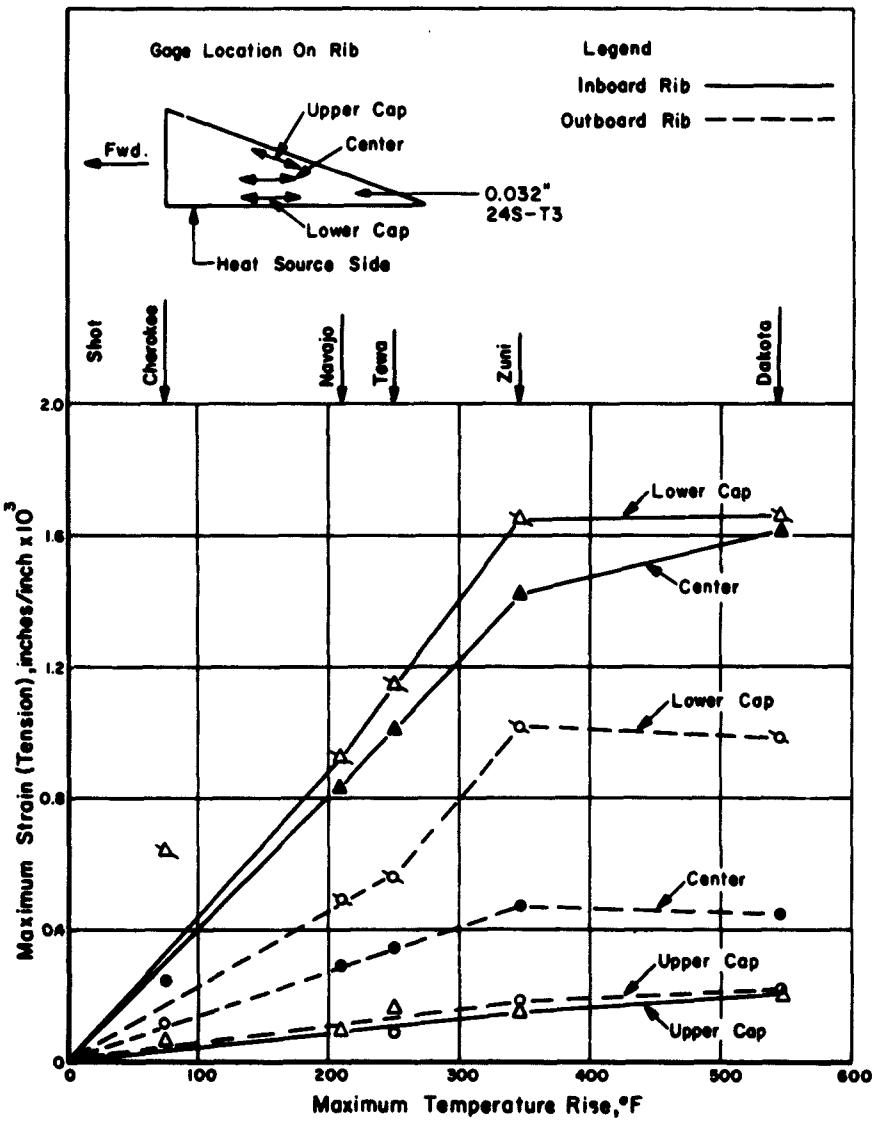

Figure 4.7 Relative rib strains versus maximum lower skin temperature rise.

4.4 GUST INPUTS

Pressure-sensing instruments were orientated about the fuselage at Station 1227.0 and at the bottom of the fuselage at Station 292.0 as described in Section 2.2.4. This sensor arrangement insured pressure measurement at a point tangential to the impinging shock front and a measure-

ment of shock propagation time along the aircraft fuselage. Table 4.8 summarizes the peak overpressure and shock-wave-propagation time from Fuselage Station 1227.0 to 292.0 for all events. All pressures are differential values measured from ambient conditions for level flight at aircraft altitude.

Measured overpressure taken from Shot Dakota is presented in Figure 4.9. The dual time scale permits a time-history investigation of the peak condition and the duration of the positive phase.

4.5 GUST LOAD EFFECTS

4.5.1 Aircraft Disposition. Aircraft accelerations were measured in the vertical, longitudinal, and lateral directions by linear accelerometers located near the aircraft center of gravity

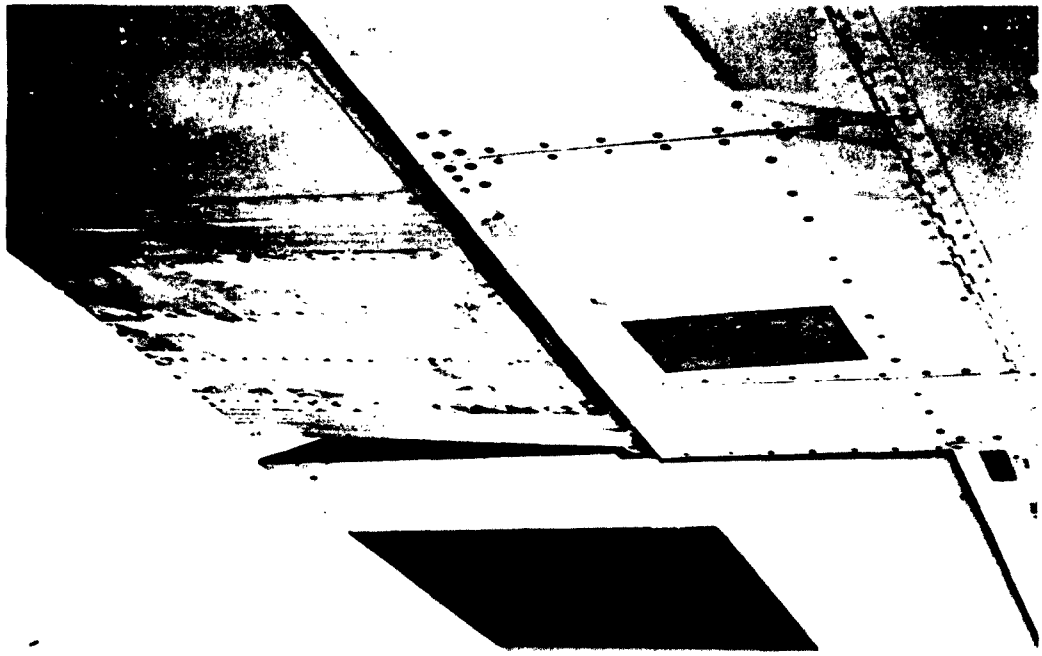

Figure 4.8 Residual buckles evident in the lower skin of the left elevator after Shot Dakota.

(c.g.). Also located near the c.g. was an accelerometer measuring angular acceleration about the aircraft lateral axis, together with a rate of pitch gyro. Change in angle of attack was measured on the vertical fin.

Time-history graphs of differential vertical acceleration, differential angle of attack, and differential rate of pitch taken during Shot Dakota are presented in Figures 4.10 through 4.12. Peak differential values of accelerations and attitudes are summarized in Table 4.9. Aircraft disposition measurements were taken from a 1.0 g flight condition.

TABLE 4.7 SUMMARY OF PEAK ELEVATOR STRAINS, LOWER-SKIN-MOUNTED ROSETTES, (MAXIMUM ARM)

+ equals tension; - equals compression. NR_e equals data not reducible. (This also exists for all gages after Zuni.)

Location	Strain	
	Cherokee	Zuni *
	μin/in	
Left, Outer Surface, Center of Panel	+ 420	+ 1,600
Left, Inner Surface, Center of Panel	− 745	− 1,830
Left, Outer Surface Near Rib	+ 420	− 970
Left, Inner Surface, Near Rib	− 305	− 1,650
Left, Outer Surface, Near Trailing Edge	NR_e	+ 1,320
Left, Inner Surface, Near Trailing Edge	+ 260	− 2,200
Right, Outer Surface, Center of Panel	+ 400	+ 1,170
Right, Inner Surface, Center of Panel	− 315	− 1,120
Right, Outer Surface, Near Rib	+ 760	+ 640
Right, Inner Surface, Near Rib	− 215	− 1,300
Right, Outer Surface, Near Trailing Edge	+ 385	− 1,190
Right, Inner Surface, Near Trailing Edge	+ 420	− 1,670

* Spare elevator used for all shots except Cherokee.

TABLE 4.8 SUMMARY OF GUST INPUTS

Shot	Recorded Overpressure	Propagation Time Sta 1227.0 to Sta 292.0
	psi	sec
Zuni	0.40	0.160
Flathead	0.27	0.082
Dakota	0.80	0.090
Mohawk	0.25	—
Apache	0.34	0.174
Navajo	0.46	0.153
Tewa	0.57	0.150
Huron	0.33	—

TABLE 4.9 SUMMARY OF PEAK ATTITUDE CHANGES AND ACCELERATIONS

Sign convention: linear accelerations up, to the right, and aft are positive. Angular acceleration causing a nose-up aircraft attitude is positive. Pitch to a nose-up aircraft attitude is positive. Angle of attack to a nose-up attitude is positive.

	Zuni	Flathead	Dakota	Mohawk	Apache	Navajo	Tewa	Huron
Differential Vertical Acceleration, g's	1.25	1.20	1.89	1.07	0.92	1.50	2.00	1.04
Differential Longitudinal Acceleration, g's	—	0.12	0.43	0.10	0.22	0.23	0.33	0.10
Differential Lateral Acceleration, g's	—	−0.03	−0.04	0.12	0	0	0	0.30
Differential Angular Acceleration, (rad/sec)/sec	—	—	−2.10	−0.47	−0.80	−1.12	−1.40	−0.90
Differential Rate of Pitch, deg/sec	−4.29	−3.25	−8.00	−2.66	−2.40	−4.15	−5.10	−2.00
Differential Angle of Attack, deg	1.55	1.82	4.00	—	1.45	2.60	2.60	3.95

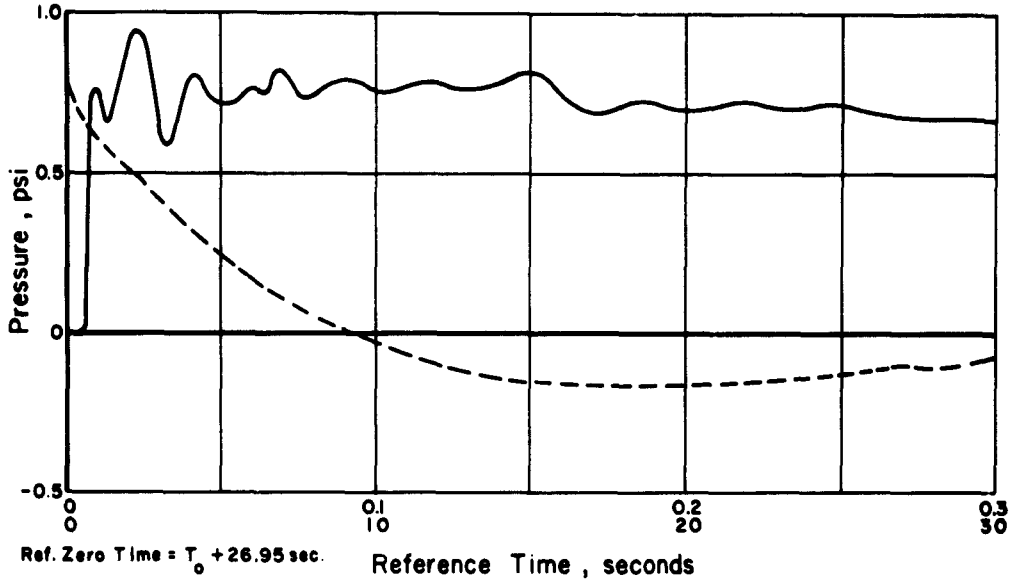

Figure 4.9 Time-history representation of overpressure taken at the aircraft during Shot Dakota.

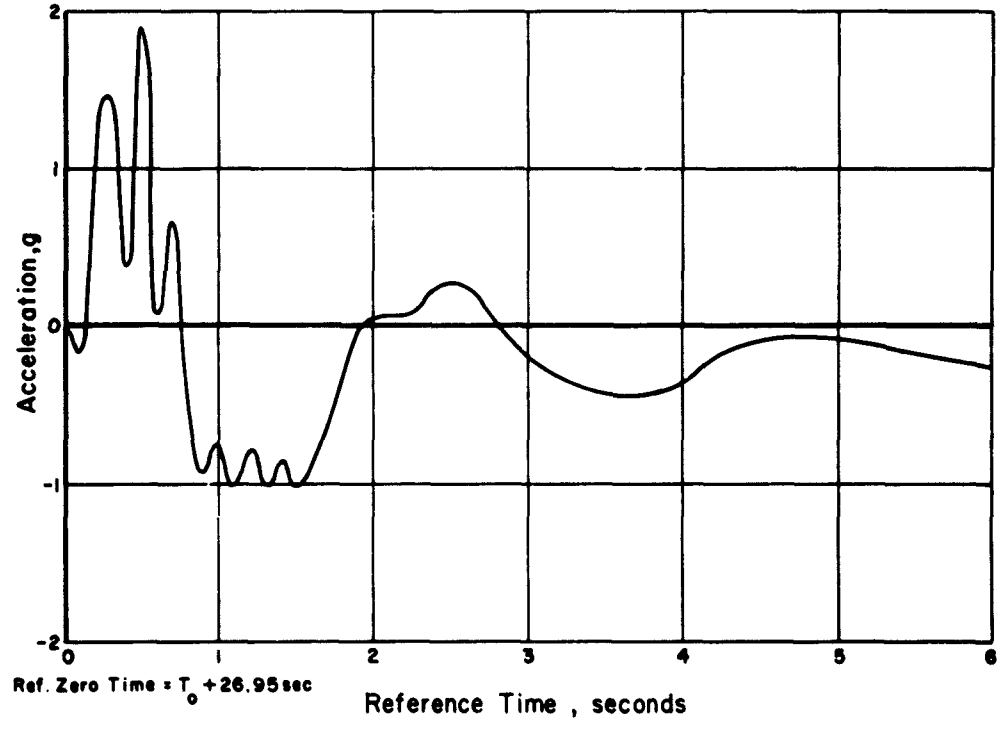

Figure 4.10 Time-history representation of differential vertical acceleration taken at the aircraft center of gravity during Shot Dakota.

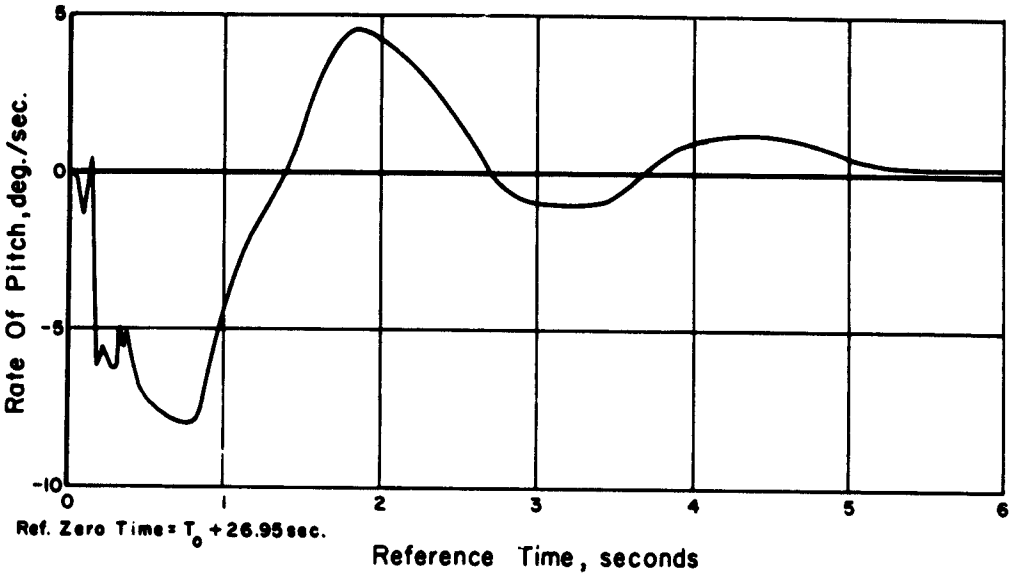

Figure 4.11 Time-history representation of differential angle of attack taken during Shot Dakota.

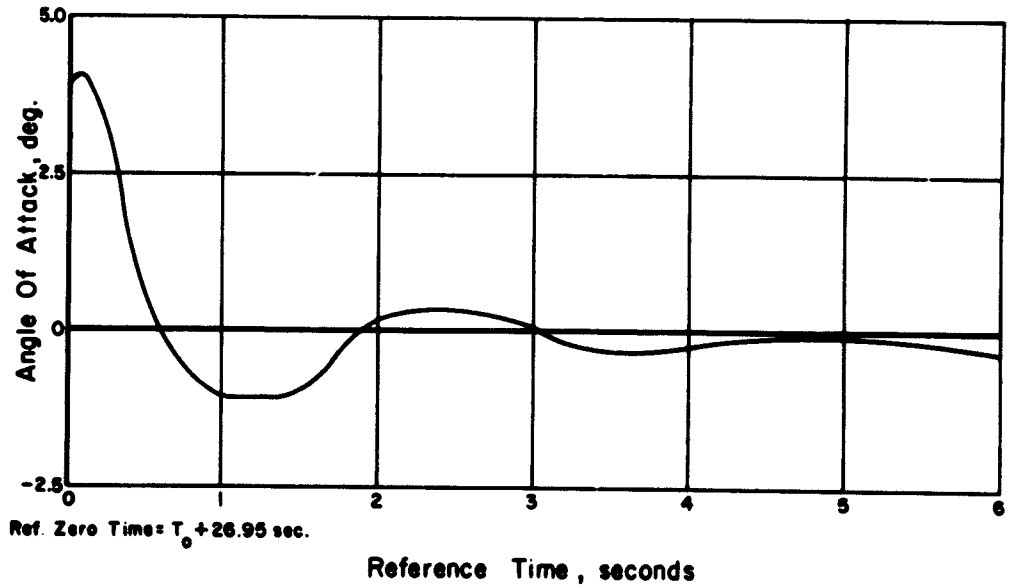

Figure 4.12 Time-history representation of differential rate of pitch taken during Shot Dakota.

4.5.2 Structural Response. Time-history plots of the wing and stabilizer differential load effects for Shot Dakota and of fuselage differential load effects for Shot Huron are shown in Figures 4.13 through 4.16. Figure 4.17 shows a time-history record of differential wing deflection for Shot Flathead. A summary of peak incremental bending moment, shear, and torque at all

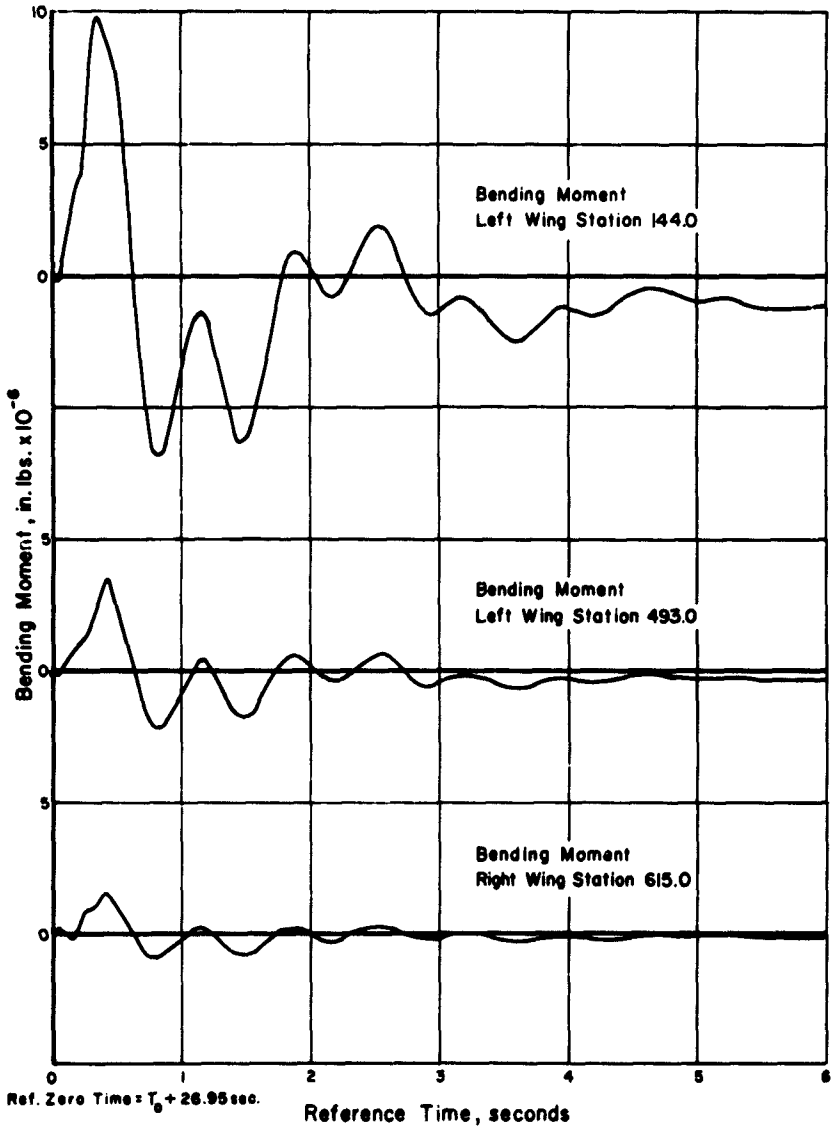

Figure 4.13 Time-history representation of differential wing bending moment taken during Shot Dakota.

instrumented stations is given in Table 4.10. Instrumentations of Right Wing Station 615.0 and Fuselage Stations 800.0 and 1044.0 were initiated in the field. These installations were completed just prior to Shots Flathead, Tewa, and Mohawk, respectively; therefore, no data for events prior to these exist. Since the aircraft was positioned for symmetrical loading during

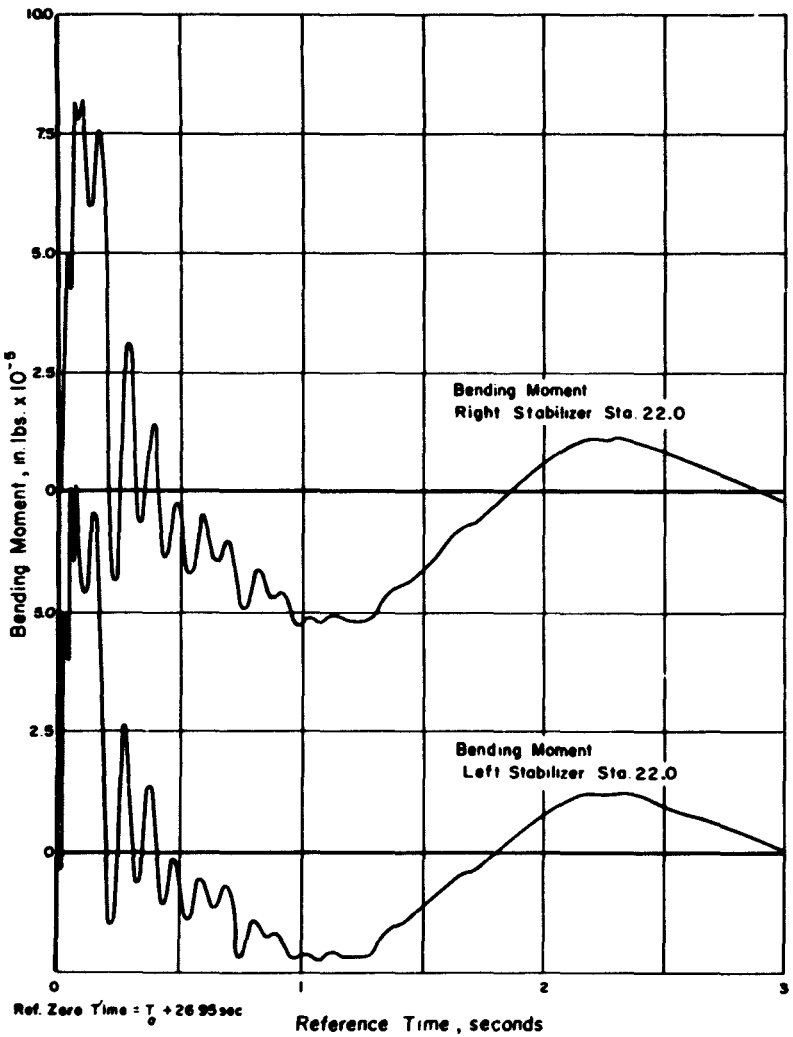

Figure 4.14 Time-history representation of differential stabilizer bending moment taken during Shot Dakota.

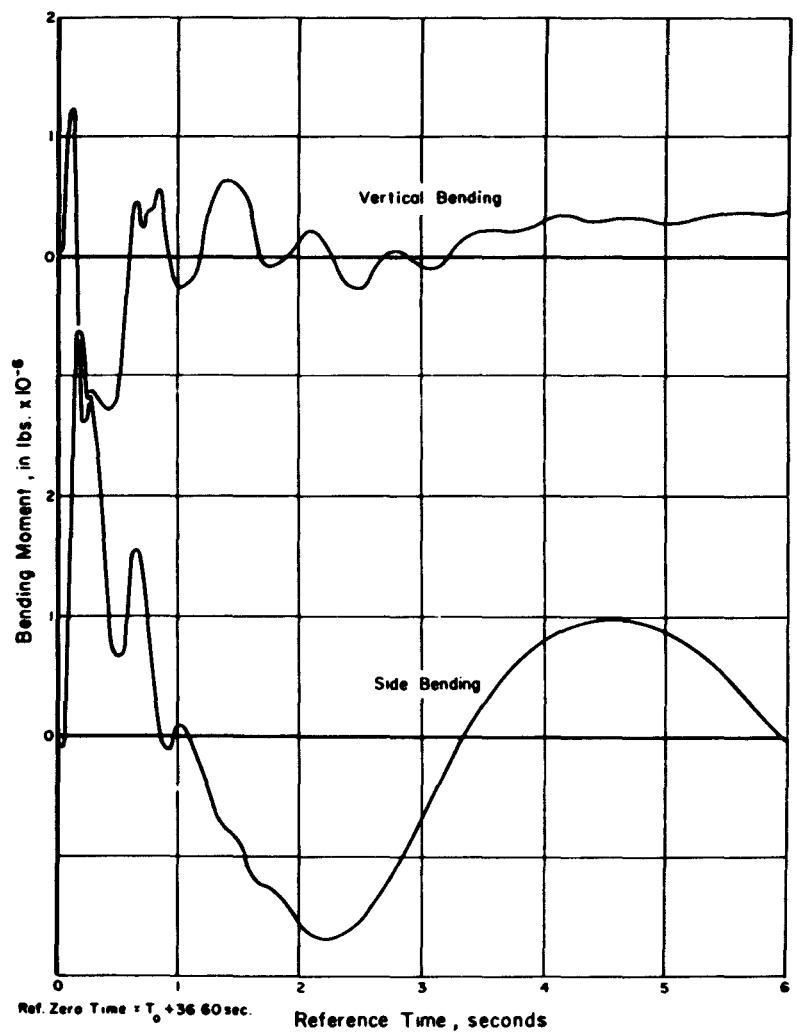

Figure 4.15 Time-history representation of differential bending moment taken at Fuselage Station 800.0 during Shot Dakota.

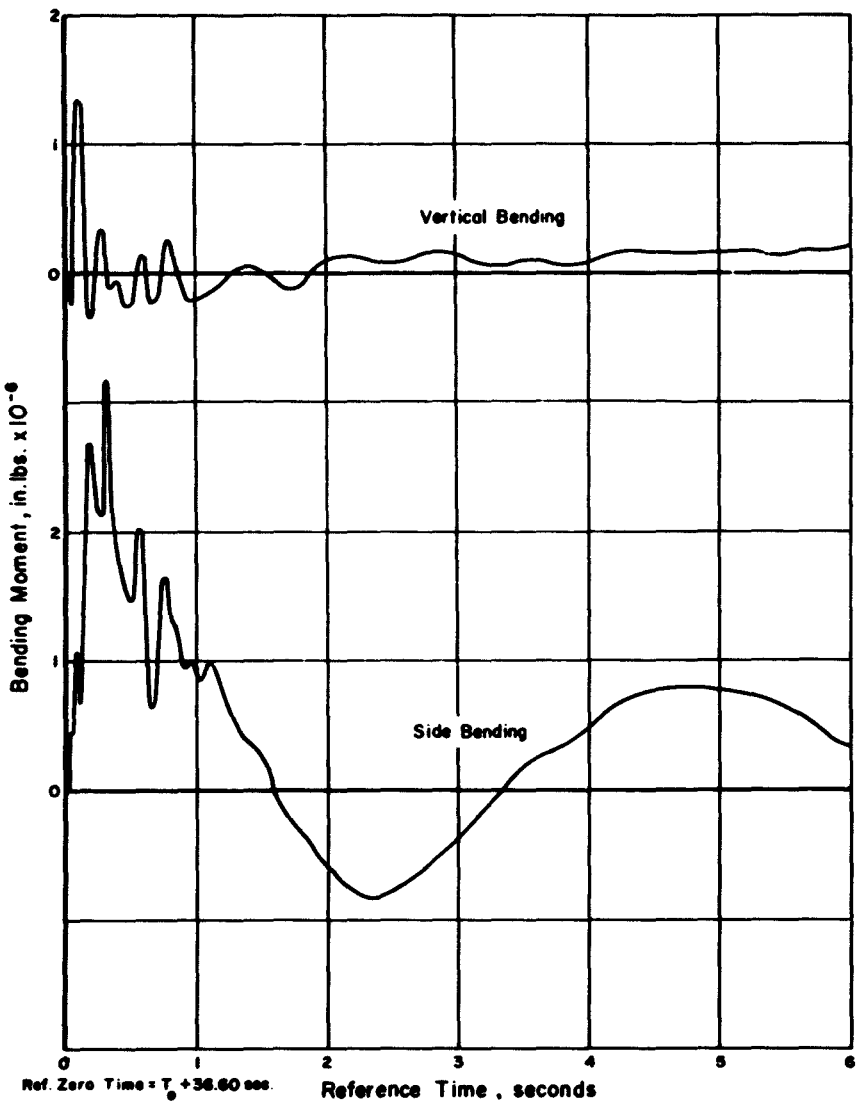

Figure 4.16 Time-history representation of differential bending moment taken at Fuselage Station 1044.0 during Shot Huron.

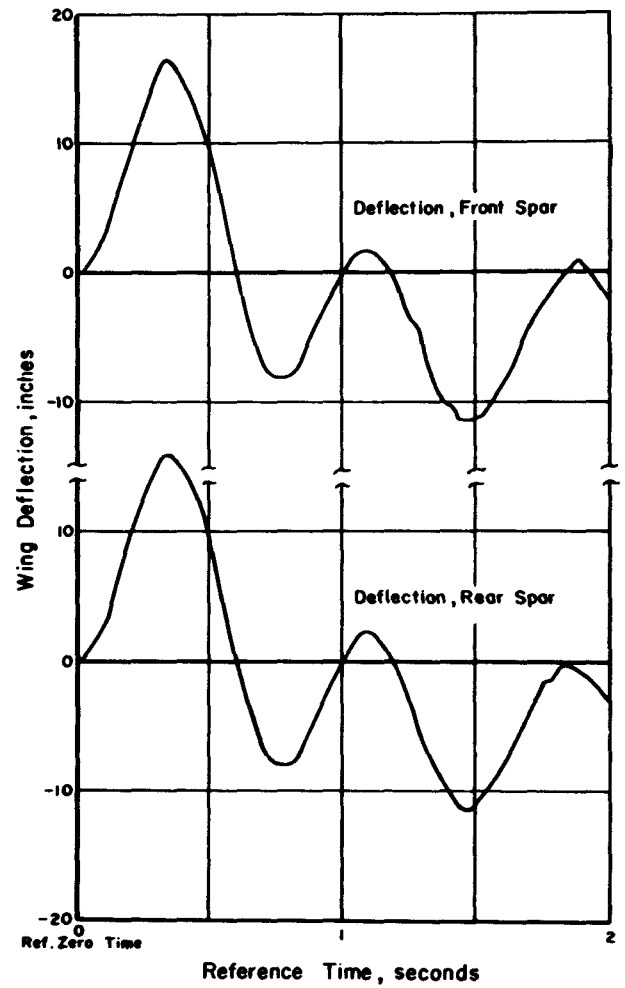

Figure 4.17 Time-history representation of differential wing deflection taken during Shot Flathead.

TABLE 4.10 SUMMARY OF GUST LOAD EFFECTS

ND, data not recorded or not reduced; NR_e, data not reducible.

	Zuni	Flathead	Dakota	Mohawk	Apache	Navajo	Tewa	Huron
Peak Incremental Moment, in-lb × 10^{-6}								
Left Wing Sta. 144.0	3.73	5.37	9.83	4.90	3.19	4.35	5.80	4.37
Left Wing Sta. 493.0	1.17	1.72	3.52	1.00	0.90	1.40	1.82	1.11
Right Wing Sta. 615.0	ND	0.91	1.45	1.08	0.45	0.66	0.92	0.34
Left Stabilizer Sta. 22.0	0.36	0.41	0.75	0.29	0.25	0.33	0.32	0.15
Right Stabilizer Sta. 22.0	0.37	0.36	0.82	0.41	0.25	0.35	0.44	0.37
Fuselage Sta. 800.0, vertical	ND	ND	ND	ND	ND	ND	3.20	−1.41 *
Fuselage Sta. 800.0, side	ND	ND	ND	ND	ND	ND	ND	3.33
Fuselage Sta. 1044.0, vertical	ND	ND	ND	0.69	ND	ND	1.80	1.34
Fuselage Sta. 1044.0, side	ND	ND	ND	0.83	ND	ND	ND	3.15
Peak Incremental Shear, lb × 10^{-4}								
Left Wing Sta. 144.0	1.05	1.39	2.69	1.47	0.73	1.01	1.30	1.08
Left Wing Sta. 493.0	0.60	0.92	1.78	0.72	0.46	0.73	0.98	0.71
Right Wing Sta. 615.0	ND	0.73	1.54	0.87	0.46	0.59	0.84	0.80
Left Stabilizer Sta. 22.0	0.40	0.51	1.37	0.38	0.33	0.48	0.64	0.35
Right Stabilizer Sta. 22.0	0.46	0.49	1.37	0.48	0.33	0.41	0.58	0.46
Fuselage Sta. 800.0, vertical	ND	ND	ND	ND	ND	ND	0.85	0.83
Fuselage Sta. 800.0, side	ND	ND	ND	ND	ND	ND	ND	1.03
Fuselage Sta. 1044.0, vertical	ND	ND	ND	0.57	ND	ND	1.05	0.67
Fuselage Sta. 1044.0, side	ND	ND	ND	0.20	ND	ND	ND	1.53
Peak Incremental Torque, in-lb × 10^{-6}								
Left Wing Sta. 144.0	0.67	0.78	1.47	0.90	0.42	0.62	0.83	1.23
(Torque axis, aft of rear spar, in)	12.86	16.19	12.86	12.86	12.86	12.86	12.86	12.86
Left Wing Sta. 493.0	0.45	0.89	1.74	0.89	NR_e	0.66	0.88	0.65
(Torque axis, aft of rear spar, in)	49.56	49.56	49.56	49.56	NR_e	49.56	49.56	49.56
Right Wing Sta. 615.0	ND	0.61	1.22	0.63	0.95	1.26	1.79	1.52
(Torque axis, aft of rear spar, in)	ND	44.82	44.82	44.82	176.14	176.14	176.14	176.14
Left Stabilizer Sta. 22.0	0.14	0.15	0.46	0.10	0.11	0.13	0.17	0.11
(Torque axis, aft of rear spar, in)	4.05	4.05	4.05	4.05	4.05	4.05	4.05	4.05
Right Stabilizer Sta. 22.0	0.18	0.17	0.51	0.15	0.12	0.15	0.21	0.19
(Torque axis, aft of rear spar, in)	9.69	9.69	9.69	9.69	9.69	9.69	9.69	9.69
Fuselage Sta. 800.0	ND	ND	ND	ND	ND	ND	−0.78	1.00
Fuselage Sta. 1044.0	ND	ND	ND	0.87	ND	ND	ND	0.93
Peak Incremental Deflection, in								
Wing Sta. 840.75	13.00	16.20	35.50	15.00	9.20	14.10	17.80	NR_e

* Positive peak of 1.24×10^6 in-lb occurs at same time as peak shear.

TABLE 4.11 REFERENCE BENDING MOMENTS (in-lb × 10^{-6})

NA, not available. Sign convention: Wing and Stabilizer: moment, shear—up load outboard of station is positive. Torque—up load forward of torque reference axis is positive. Fuselage: vertical moment, vertical shear—up load aft of station is positive. Side moment, side shear—load pushed from left is positive. Torque—load which creates clockwise torque about fuselage centerline, looking forward, is positive.

Condition	W.S. 144	W.S. 493	W.S. 615	S.S. 22	F.S. 800 (Vertical)	F.S. 800 (Side)	F.S. 1044 (Vertical)	F.S. 1044 (Side)
1.0 g flight	8.6	1.86	0.804	0	0	0	0	0
Limit load	32.3	6.00	2.52	1.36	NA	NA	NA	NA

TABLE 4.12 SUMMARY OF ENGINE PERFORMANCE

NA - Data not available.

Engine Parameters J-47-25A Engine	Shot							
	Zuni	Flathead	Dakota	Mohawk	Apache	Navajo	Tewa	Huron
Compressor Inlet Pressure, Probe No. 1, psi*	0.18	0.03	0.52	0.07	0.13	0.20	0.23	0.42
Compressor Inlet Pressure, Probe No. 2, psi*	0.21	0.04	0.50	0.07	0.15	0.20	0.21	0.42
Compressor Inlet Pressure, Probe No. 3, psi*	0.18	0.07	0.57	0.07	0.13	0.14	0.21	0.42
Compressor Discharge Pressure, psi*	0.90	0.70	1.77	0.95	0.83	1.23	1.22	1.26
Tail-Pipe Pressure, psi*	0.29	0.33	0.62	0.17	0.34	0.33	0.32	0.34
Compressor Discharge Temperature, F†	356.0	316.0	290.0	NA	347.0	297.0	335.0	NA
Exhaust-Gas Temperature, F†	838.5	848.0	537.0	NA	799.0	794.0	826.0	615.0
Engine rpm, pct max‡	87.0	87.0	76.0	83.0	85.4	85.2	86.8	NA

* Peak incremental measurements. † Absolute measurement. ‡ Engine rpm at time of shock arrival.

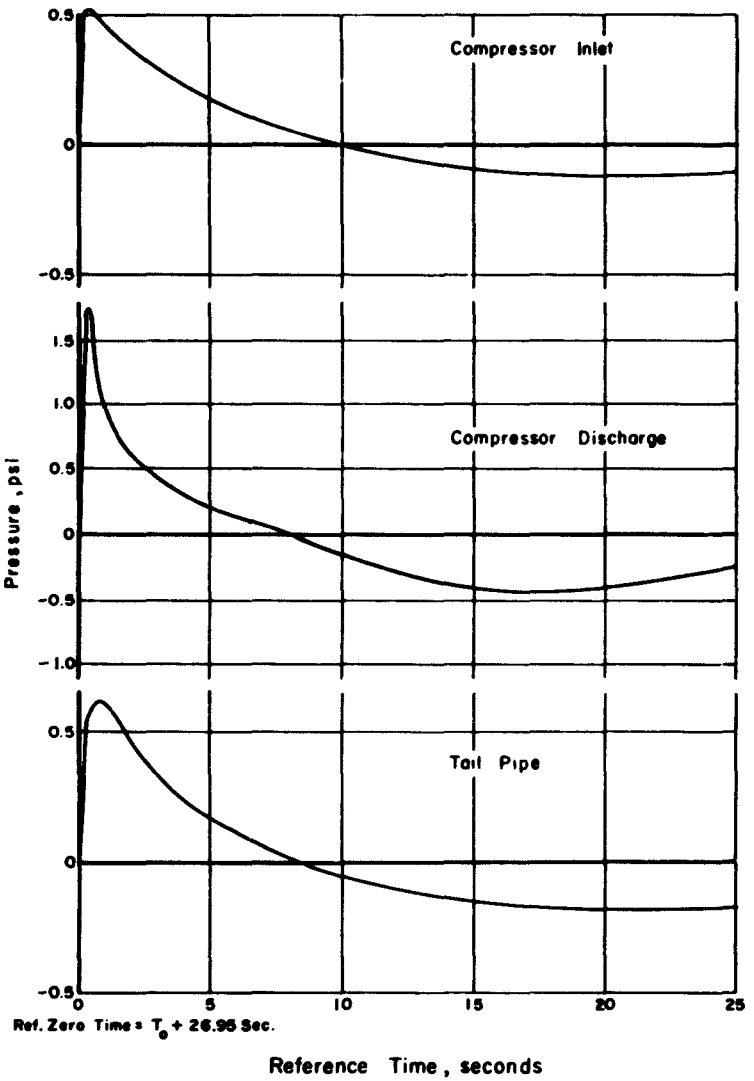

Figure 4.18 Time-history representation of differential engine pressure taken during Shot Dakota.

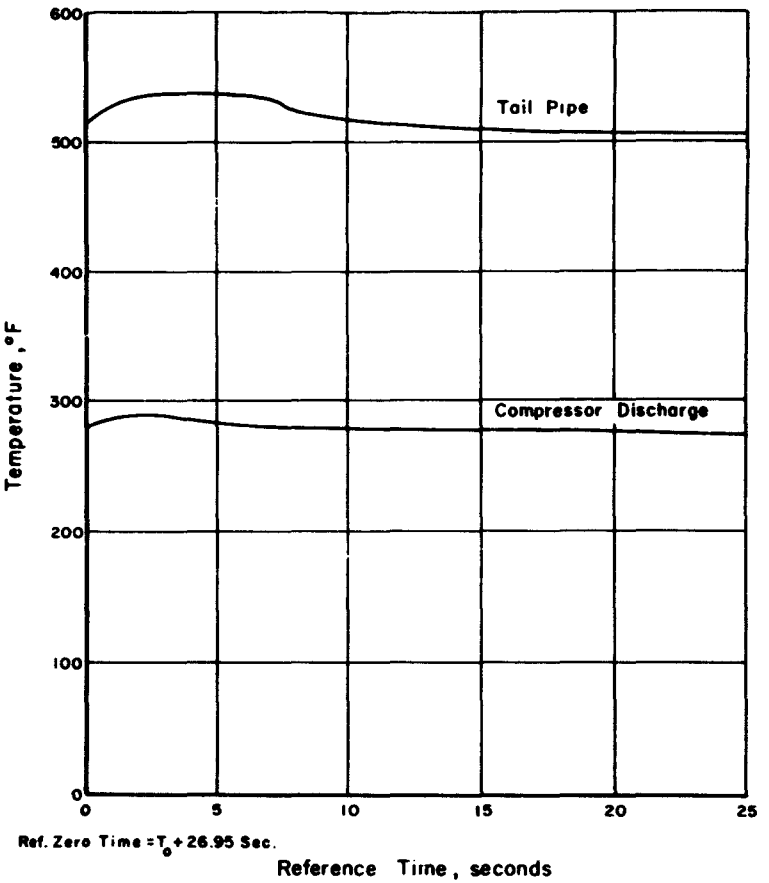

Figure 4.19 Time-history representation of engine temperature taken during Shot Dakota.

Shot Tewa, vertical-loads data were developed and side-loads data were neglected at the fuselage stations.

One g bending moment at a constant dynamic pressure, within the range of dynamic pressure encountered during test events, in addition to design limit loads and sign convention, are presented in Table 4.11. Measured incremental moment added to the one g moment enables determination of the percent of design limit moment measured.

4.5.3 Effects on Engine Performance. Data listed in Table 4.12 were obtained from pressure transducers and thermocouples installed directly on the engine and recorded in the CRA, with the exception of engine rpm, which was indicated directly on the chaff chute photo panel. Time-history graphs of engine performance for Shot Dakota appear in Figures 4.18 and 4.19.

Chapter 5
DISCUSSION

It was possible to participate successfully in all shots of Operation Redwing which had been selected for capability data. Two of these shots were used for obtaining data on side-load effects. Aircraft instrumentation, including all primary and auxiliary data sources and recorders, was from 91 to 96 percent operational during the test series. Events utilized to test the aircraft's weapon delivery capabilities included Shots Cherokee, Zuni, Flathead, Dakota, Apache, Navajo, and Tewa. Events utilized to obtain side-load data were Shots Mohawk and Huron.

The selection of events for capability data on the B-47E was made to give reasonable assurance of near-limit inputs for gust and/or thermal loads. A more conservative positioning criterion was used in the selection of events for side-load data. Actual yields varied from 33 to 135 percent of preshot positioning yield; therefore, a good range of data was established relating to both aircraft capability and weapon effects.

The decision to investigate the effects of side loads on a bomber-type aircraft was made during the course of the operation, when it was ascertained that data sufficient for capability studies would be obtained. It was determined that the aircraft could be instrumented for measurement of side loads and positioned to receive the side inputs from Shots Mohawk and Huron without sacrificing primary capability data. The decision to study side-load effects was based upon the need for data to correlate effects on bomber-type aircraft with those being obtained for a fighter type aircraft (Project 5.5, F-84F Research Aircraft) and to refine prediction methods for side-load effects.

All predicted values appearing herein are based on final yields and aircraft positions.

5.1 THERMAL INPUTS

Predictions of total radiant exposure were found to be generally conservative; i.e., higher than actual radiant exposure as measured by the calorimeters. This conservative trend is evident in Figures 5.1 and 5.2 where the data can be seen to lie, in general, closer to the 20 percent line than to the perfect agreement line. Measured total radiant exposure was based upon the readings of three calorimeters aimed at ground zero, equipped with quartz filters and possessing 90-degree fields of view.

In both Figure 5.1 and Figure 5.2, Shots Navajo and Zuni show unusually high measured values in comparison with the predicted, while in both cases the measured values which were lowest with respect to predicted were recorded on Shots Cherokee and Tewa. The meteorological data of Table 4.2 indicate a possible reason for this occurrence. During all shots, the heaviest cloud coverage at altitudes between the device and the aircraft was reported for Shots Navajo and Zuni and the lightest for Shots Cherokee and Tewa.

The effect of clouds on thermal radiation is a complex phenomenon depending on cloud thickness, particle size and distribution, absorption, albedo, geometry, atmospheric attenuation, source spectral distribution, and the albedo of the underlying ground. The problem was discussed in Reference 13 and it was concluded that although the effect of clouds above the aircraft altitude could probably be neglected, a laboratory model study indicated that clouds between the device and the aircraft could greatly increase the thermal radiation at the aircraft in certain areas of space. This increase can be brought about either by reflection or transmission, since both are primarily scattering processes, although the water vapor absorption also present is an attenuating process.

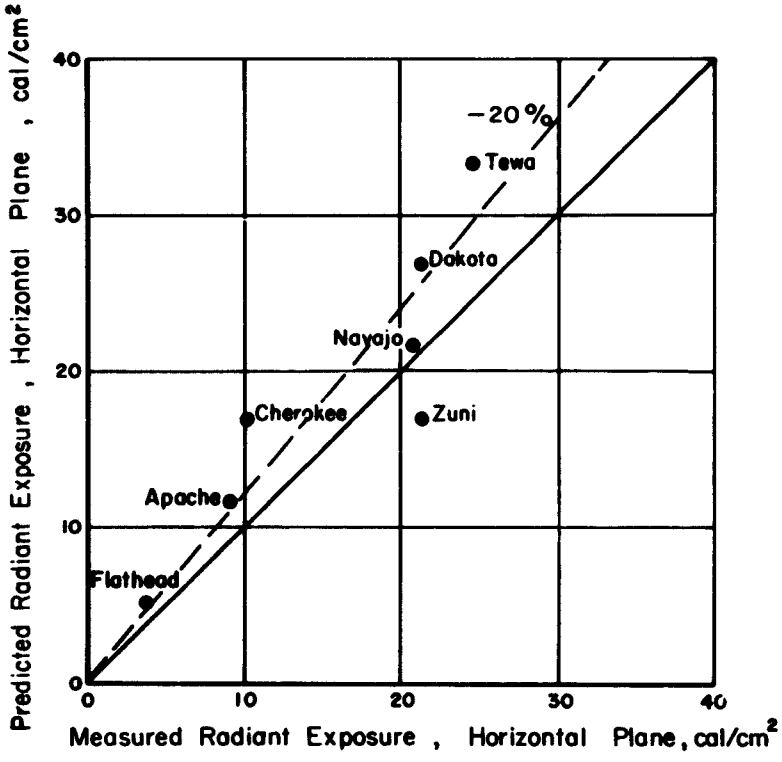

Figure 5.1 Predicted versus measured radiant exposure incident upon a horizontal plane.

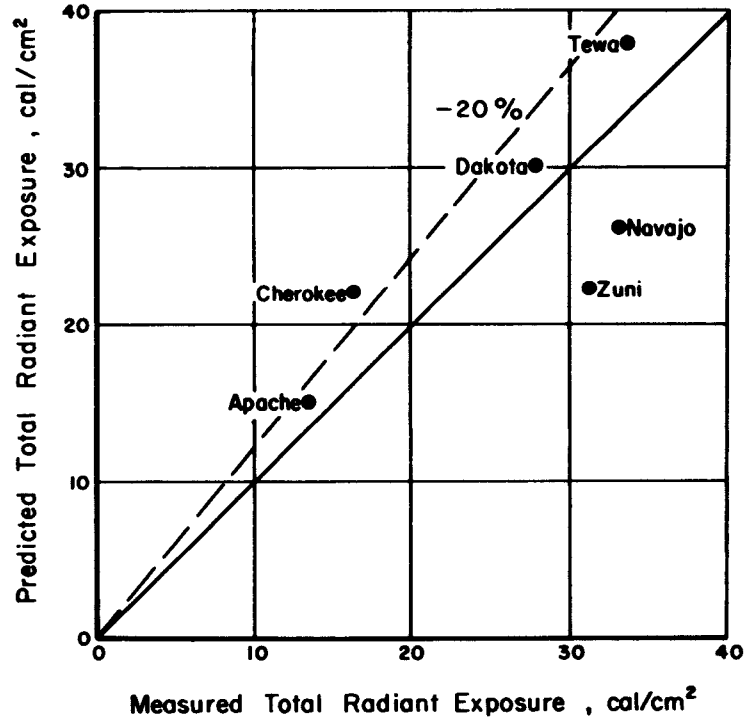

Figure 5.2 Predicted versus measured total radiant exposure direct from ground zero.

It seems likely, then, that the prediction trend was 20 percent or more conservative, and that the heavy cloud coverage on Shots Navajo and Zuni caused an unpredicted increase in measured thermal energy.

It was possible to ascertain the effect of the angle of the field of view for the calorimeter upon the readings obtained. Table 4.2 showed readings for 21-degree, 45-degree, and 160-degree fields of view as well as the 90-degree field of view values. It can be seen that the 21-degree field of view sees about 60 percent, the 45-degree field of view sees about 80 percent, and the 160-degree field of view sees about the same as the 90-degree field of view calorimeter.

The reliability of measured values of irradiance and radiant exposure can be estimated by integration of the thermal irradiance curve to a time where further integration would not add significantly to the total value. At that particular time, a comparison was made of measured radiant exposure and the integrated irradiance. The comparison is shown in Figure 5.3, and good correlation is evident.

5.2 THERMAL RESPONSES

5.2.1 Temperature Rises. Measured temperature rises in the lower center panel of the right elevator have been compared to predicted values in Figure 5.4. The predicted temperature rises are based upon measured thermal radiation at the surface. The theoretical rises are seen to be higher than measured rises, showing conservatism in the prediction theory.

In attempting to cause plastic deformation, test areas were painted with high absorptivity paint. For Shot Dakota, the entire elevator and reference panel were black (α = 0.96), and maximum temperature rise was 547 F in the reference panel. Paint blistering may have acted as an insulation barrier and have effectively reduced the peak temperature rise. The application of paint under field conditions probably caused the failure of the paint in this and other test panels. Even though the paint blistered, much valuable information concerning plastic deformation at elevated temperatures and thermal strains was derived from the test. The thermal responses obtained were of such magnitudes that large areas of thin-skinned control surface were buckled without adverse effect on control or stability of the aircraft, either in flight or under landing conditions.

5.2.2 Visible Effects. Together with the elevator buckling shown in Figure 4.8, another visible thermal effect was observed in the postshot examination of the aircraft after Shot Dakota. This effect was a hole of dimensions roughly 1 by $1\frac{1}{2}$ inches burned in the outboard seal of the elevator.

In several other shots, the pilot observed that engine fire warning lights came on at time zero, but went off after a few seconds. This effect was undoubtedly caused by direct radiant exposure of the fire warning sensor and not by engine malfunction.

5.2.3 Thermal Strain. Maximum elevator-stress-producing strains were obtained on the lower skin surface. Peak values of 760 μin/in tension for Shot Cherokee and 2,200 μin/in compression for Shot Zuni were indicated in the summaries of stress-producing strain, Tables 4.5, 4.6, and 4.7. The yield stress for 24S-T3 clad aluminum was 37,000 psi indicating the value of yield strain to be about 3,500 μin/in. Comparison of these values clearly shows that destructive permanent set was not attained on Shots Cherokee or Zuni on the left elevator.

Figure 4.8 showed that significant permanent set occurred on Shot Dakota, as evidenced by the relatively large residual buckles. Correlation of skin strain to temperature rise, in order to obtain the condition at which permanent set first occurs, was not possible because of the destruction of strain gages mounted on surfaces receiving high temperature rises. In order to obtain some related information, the temperature rise of the lower skin must be compared to strain data of another surface instrumented. This comparison might be made on the upper skin

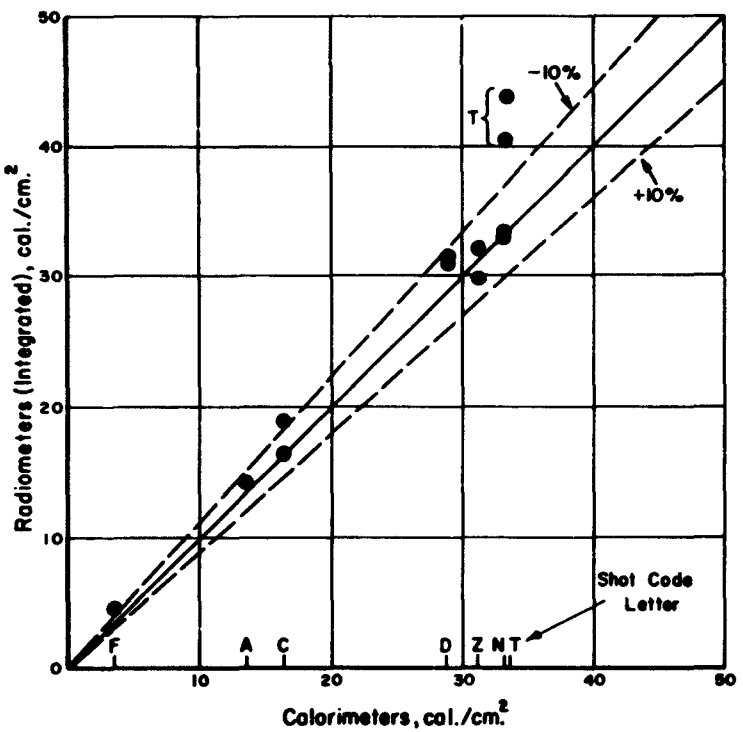

Figure 5.3 Integrated radiometer inputs versus calorimeter inputs.

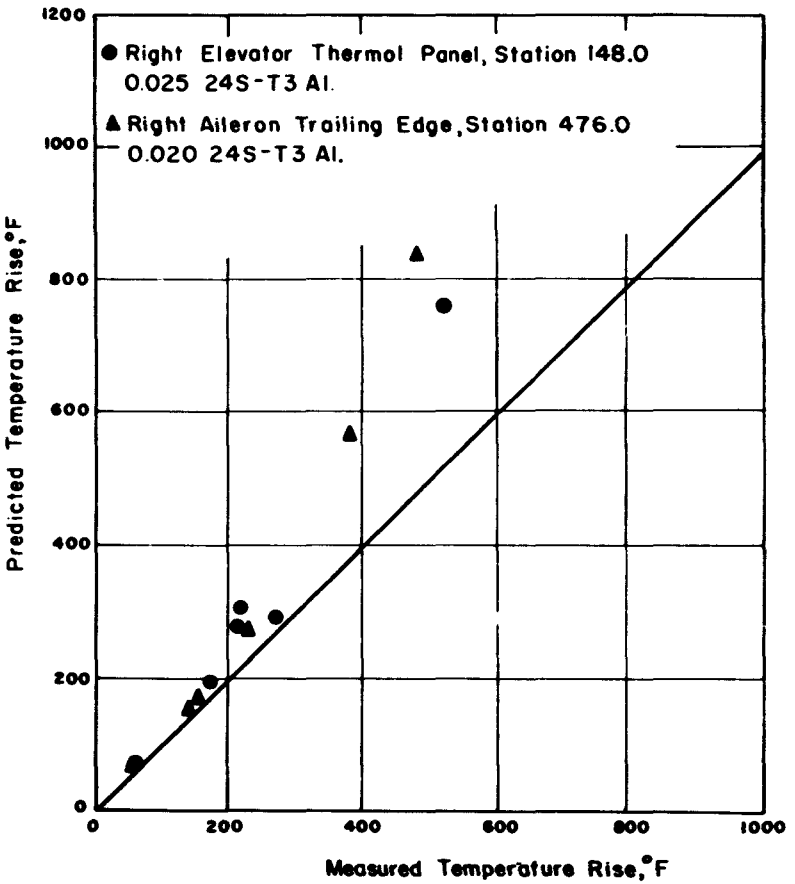

Figure 5.4 Predicted versus measured temperature rise.

of the elevator but the single rosette mounted there showed small reactions, as indicated in Table 5.1. Therefore, the only possible strain available for such correlation lies on the primary structure.

The maximum listed stress-producing strain for primary structures, Tables 4.5 and 4.6, was 1,660 μin/in tension. Since the tensile yield stress for 24S-T3 clad aluminum alloys was 37,000 psi (with a value of strain of approximately 3,500 μin/in) the data indicated that at no time did either the ribs or the front spar go into significant permanent set.

Although the lower skin gages were burned off on high input shots, the gages mounted on the primary structure reacted for all tests considered. Thus, it is evident that gages mounted on internal primary structures are operative past the point where gages fail on the secondary surface, the lower skin. Also, from data presented in Figures 4.7 and 5.5 and discussion relating thereto, it is evident that the lower skin will go into significant permanent set, fail, or be completely destroyed before failure will occur in the primary structures.

The stress-producing strain values of the left elevator ribs were related to the maximum temperature rise of the lower skin surface. The strain values considered were for gages

TABLE 5.1 SUMMARY OF PEAK LEFT ELEVATOR STRAINS, UPPER-SKIN-MOUNTED ROSETTE (MAXIMUM ARM)

+ equals tension, – equals compression.

Shot	Strain	ΔT_{max}
	μin/in	F
Cherokee	+80	75
Zuni	+180	346
Dakota	+155	547
Apache	–120	250
Navajo	–109	210

mounted on the lower rib cap, the center of the rib oriented parallel to the lower cap, and the upper rib cap. The maximum strain values attained on each point were related to maximum lower skin temperature rise and presented in Figure 4.7. In order to present a time correlation of rib reactions to the maximum lower skin temperature rise (all at the same time), Figure 5.5 was developed. This figure also provides a visual presentation of the variation of rib strain related to gage distance from the lower skin. Both Figures 4.7 and 5.5 indicate the existence of a strain transition zone between maximum temperature rise values of 350 F and 450 F. Also indicated is a consistent difference in strain reactions between similar locations on the inboard and outboard ribs.

Since the tensile-stress-producing strains indicated for the ribs were due primarily to the difference in the expansion rates of the lower skin and rib proper, then any relief of the expansion of the lower skin would result in a decrease of the rib strains. The most obvious relief of the lower skin expansion would be yield or significant permanent set (large buckled area) of the material. Thus, the transition zone is an indication of this effect on the lower skin structure. Further evidence of this transition zone is indicated from the observed visual effects on Shot Zuni. Local buckling in the lower skin was observed after this shot with a maximum temperature rise of 346 F. This also indicates yield point in the vicinity of 350 F or greater.

Because of the existence of lightening holes in the outboard rib of the left elevator, the mass is less than that of the inboard rib. Because of this mass difference, the temperature rise for the outboard rib is always larger and more rapid than for similar points on the inboard rib.

This causes the outboard rib to exhibit temperature reactions more similar to the lower skin surface than does the inboard rib; thus, the stress-producing strains in the inboard rib are always greater for similar points when compared to the outboard rib as shown in Figures 4.7 and 5.5.

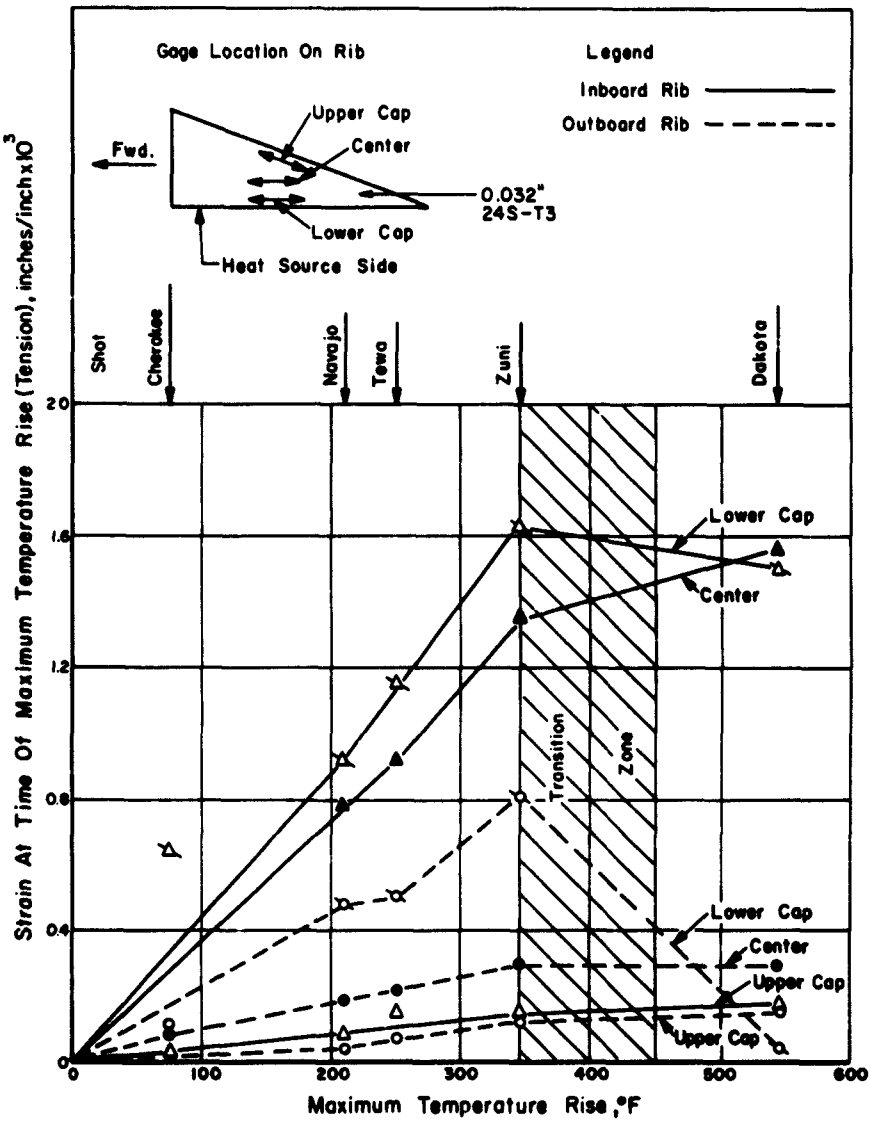

Figure 5.5 Related rib strains of the left elevator thermal panel.

5.3 GUST INPUTS

As shown in Table 4.8, peak overpressures measured on the aircraft fuselage ranged from 0.25 to 0.80 psi. The correlation of measured and final postshot predicted overpressures is shown in Figure 5.6. The predicted values were based on final measured yield and aircraft position. Data from all shots indicated that the theoretical method of predicting overpressure was

accurate to within approximately 10 percent. The data shown in Figure 5.6 were measured at a point tangential to the direction of shock propagation to eliminate as much as possible the effect of dynamic pressure and air-flow disturbances. A comparison of the pressure measured tangential to the impinging shock front and pressure measured on the bottom fuselage is shown in Figure 5.7 to illustrate the effect of dynamic pressure.

Peak values of recorded overpressures were determined by extrapolation of a relatively flat portion of the time-history plot back to time of shock arrival (T_{sa}). The portion used for extrapolation generally appears after the decay of initial high frequency disturbances caused by shock.

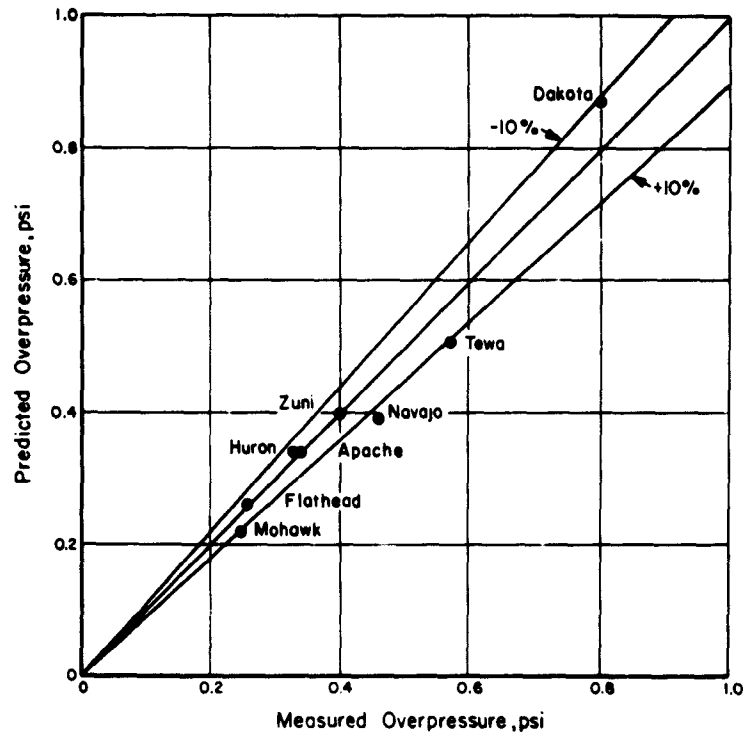

Figure 5.6 Predicted versus measured overpressure.

In the case where disturbances last for more than 0.4 second, an average is taken through the disturbances and extrapolated to time of shock arrival.

5.4 GUST LOAD EFFECTS

5.4.1 Aircraft Disposition. The effective change in angle of attack, because of gust velocity behind the shock wave, was evaluated by two different techniques: (1) direct measurement of wind vector relative to an aircraft datum using a Specialties Incorporated Model L-30 angle-of-attack indicator, and (2) measurement of shock wave propagation time along the line of flight.

Shock wave propagation times were used primarily to evaluate shock wave angle of incidence; however, if the gust vector was assumed coincident with the shock front vector, it was possible to evaluate change in angle of attack. The relationship between gust angle of incidence and propagation time is:

$$\gamma = \cos^{-1} \frac{V_s}{d/\Delta_t + V_a}$$

Where: γ = angle of incidence to horizontal plane
Δ_t = propagation time over a distance d
d = distance between measured points
V_a = aircraft velocity
V_s = shock front velocity

The above relationship applies only for symmetrical loading (shock front vector and aircraft lie in the same vertical plane).

The Rankine-Hugoniot expressions were used to compute the magnitude of the gust while the direction of the gust was assumed identical with the direction of the shock vector. The change

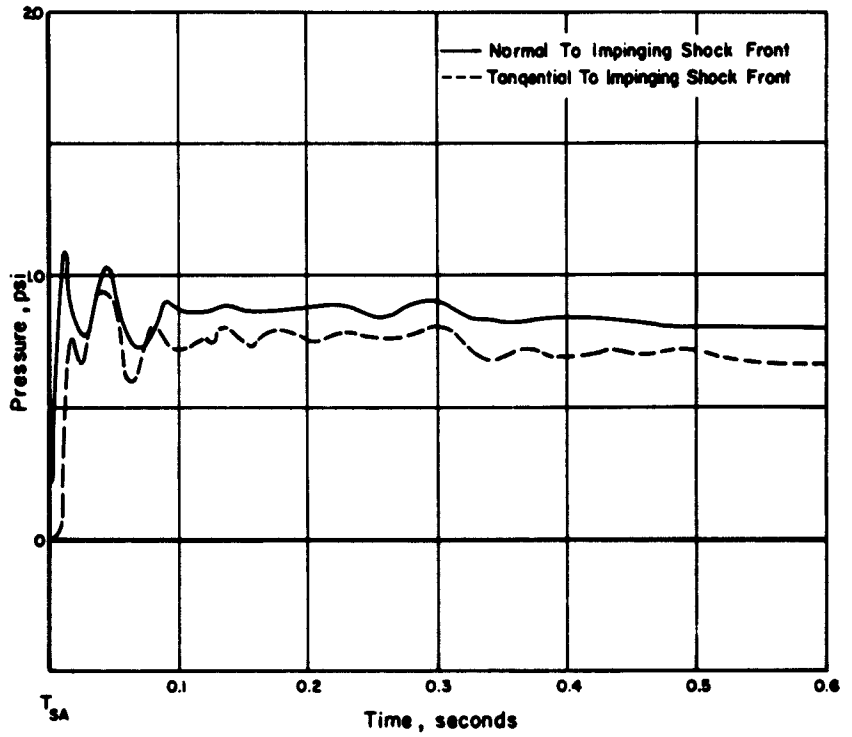

Figure 5.7 Comparison of differential pressures taken at points tangential and normal to the impinging shock front.

in angle of attack was then computed by adding vectorially the aircraft and gust velocities.

Peak values of differential angle of attack derived from the two methods, together with gust velocity and angle of incidence appear in Table 5.2. The angle of attack calculated by Method 2 above is an instantaneous change occurring at time of shock arrival, while the value of Method 1 above was taken at the time of maximum measured differential angle of attack (maximum occurred at 0.1 to 0.2 second). Although the results of both methods are referred to as angle of attack, the values will differ for the following reasons:

1. The measured change in angle of attack was taken relative to an aircraft datum. Pitching of the aircraft into the relative wind was evident in all events. Therefore, the amount of pitch during the time lapse from time of shock arrival to time of shock arrival plus 0.1 to 0.2 second would result in a measured angle of attack, by Method 1, of lower value than would be expected from the results of Method 2.

2. The calculated change in angle of attack uses in its derivation a value of material velocity which was developed using the value of measured overpressure extrapolated to T_{sa}. The extrapolated value of overpressure would be higher than that existing at the time of maximum measured angle of attack; therefore, the calculation would yield values of angle of attack larger than measured.

5.4.2 Structural Response. In order to establish primary aircraft capabilities, the structural reactions of the wing due to gust effects were measured and compared to predicted reactions, based on existing theories using final yield and aircraft position. Comparisons of wing bending at Wing Stations 615.0 and 493.0 showing the correlation between measured and predicted values, are given in Figures 5.8 and 5.9. The coordinates are the incremental wing-bending increases from the 1.0 g flight conditions. The comparisons for Wing Station 615.0 show theory to be un-

TABLE 5.2 CALCULATED GUST INPUTS AND ATTITUDES

Shot	Differential Angle of Attack *	Differential Angle of Attack †	Angle of Shock Wave Incidence	Estimated Gust Velocity
	deg	deg	deg	ft/sec
Zuni	1.55	2.67	31.52	63.0
Flathead	1.82	3.63	52.62	56.1
Dakota	4.00	6.17	45.78	96.8
Mohawk	—	—	—	49.4
Apache	1.45	2.00	28.25	51.9
Navajo	2.60	3.70	35.47	80.2
Tewa	2.60	4.65	34.53	99.0
Huron	—	—	—	37.2

* Direct measurement of wind vector relative to an aircraft datum added.
† Calculated by vector addition of aircraft and gust velocities.

conservative by about 20 percent. Conversely, the comparisons for Wing Station 493.0 show at least a 40 percent conservative trend.

A plot of percent limit bending moment at Wing Station 615.0 versus percent limit bending moment at Wing Station 493.0 (Figure 5.10) indicates that in all but two events, Shots Huron and Dakota, Wing Station 615.0 appeared to be more nearly critical.

The correlation of data at Wing Station 144.0 with preliminary postshot predictions indicated approximately a 30 percent conservative trend in measured bending moment.

5.4.3 Visible Damage. Postshot inspection of the aircraft consisted of a close examination of all structural elements and aircraft components (radome, fairing, etc.) which would be subject to blast damage. Visible effects of blast damage were in evidence only after Shots Dakota and Tewa.

Damage to the aircraft from Shot Dakota was limited primarily to the doors of the forward wheel well and bomb bay. A photograpn of damage to the left bomb-bay door is shown in Figure 5.11. A similar buckle pattern was in evidence on the right bomb-bay door. The damaged section included the rear two rib sections having 0.040-inch magnesium skin (QQ heat treat). The stops for the rear bomb-bay doors were completely ruptured; they were reinforced when replaced. The rupturing of the door stops probably contributed to the doors' buckling. Repair of damage was considered unnecessary, and the remaining missions were flown with the original doors. Fire-extinguisher knockouts on all engines were dislodged.

Bomb-bay and forward-wheel-well doors showed slight effects of gust damage after Shot Tewa. Paint was spalled off rivets and serrated along the peaks and valleys of the major buckles caused by Shot Dakota.

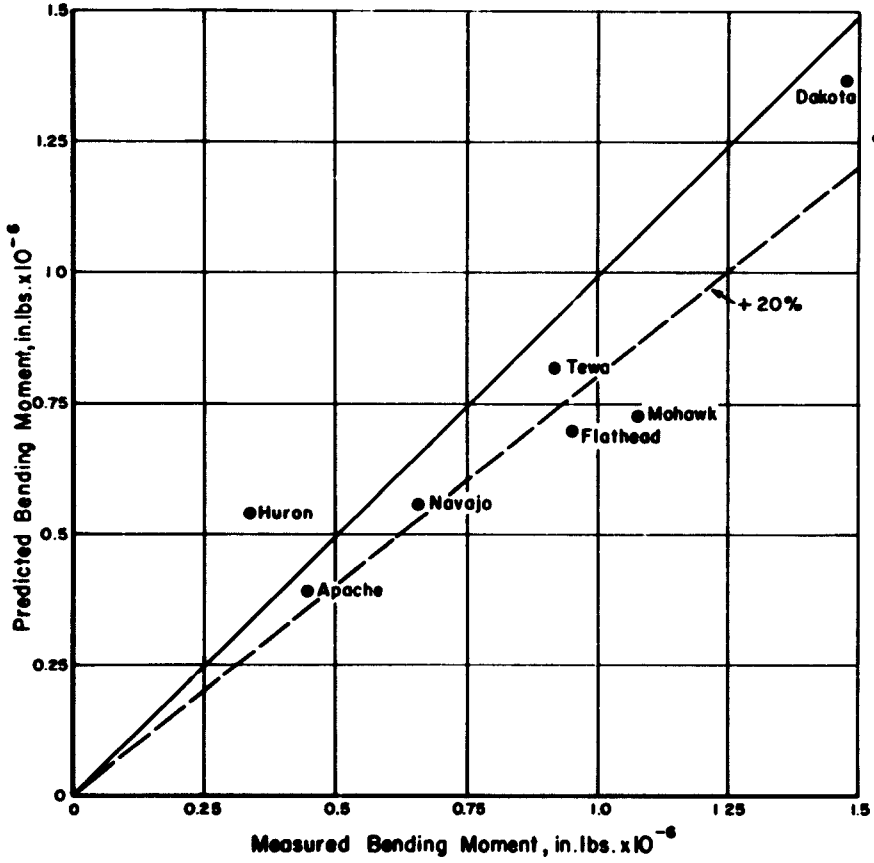

Figure 5.8 Predicted versus measured bending moment at Right Wing Station 615.0.

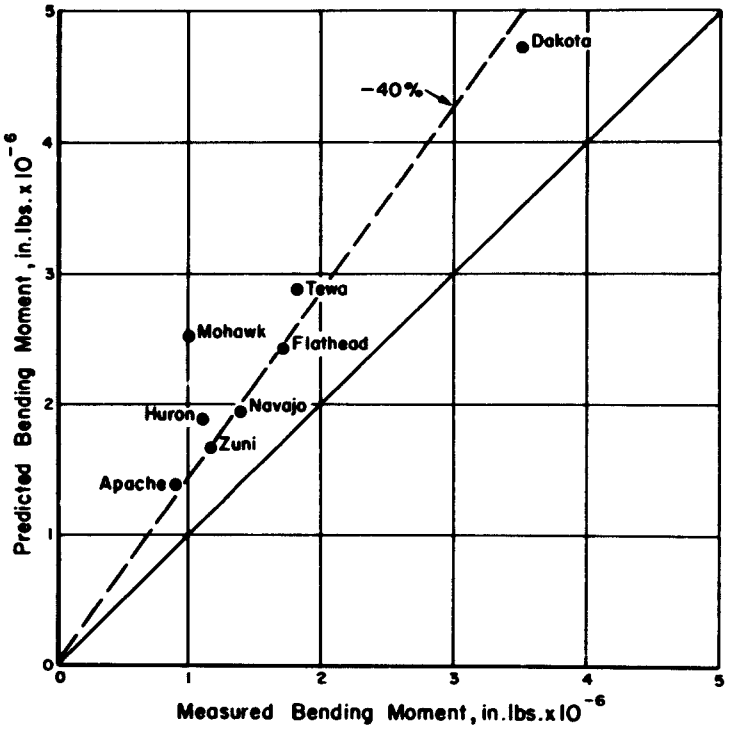

Figure 5.9 Predicted versus measured bending moment at Left Wing Station 493.0.

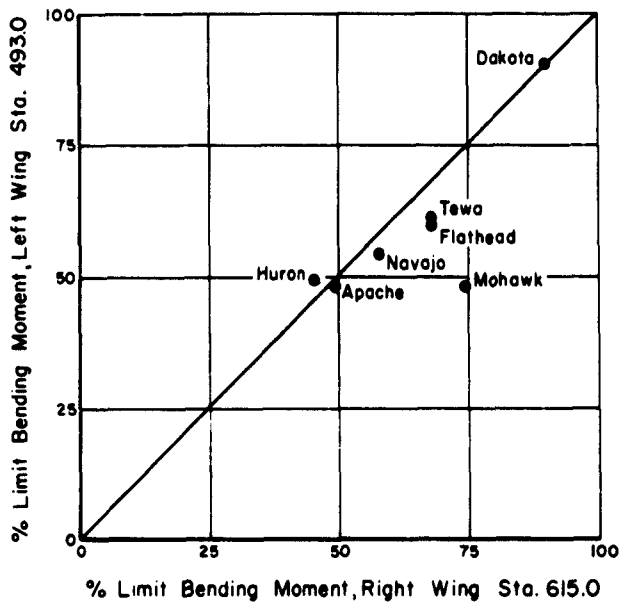

Figure 5.10 Comparison of the percent limit bending moments of Wing Stations 615.0 and 493.0.

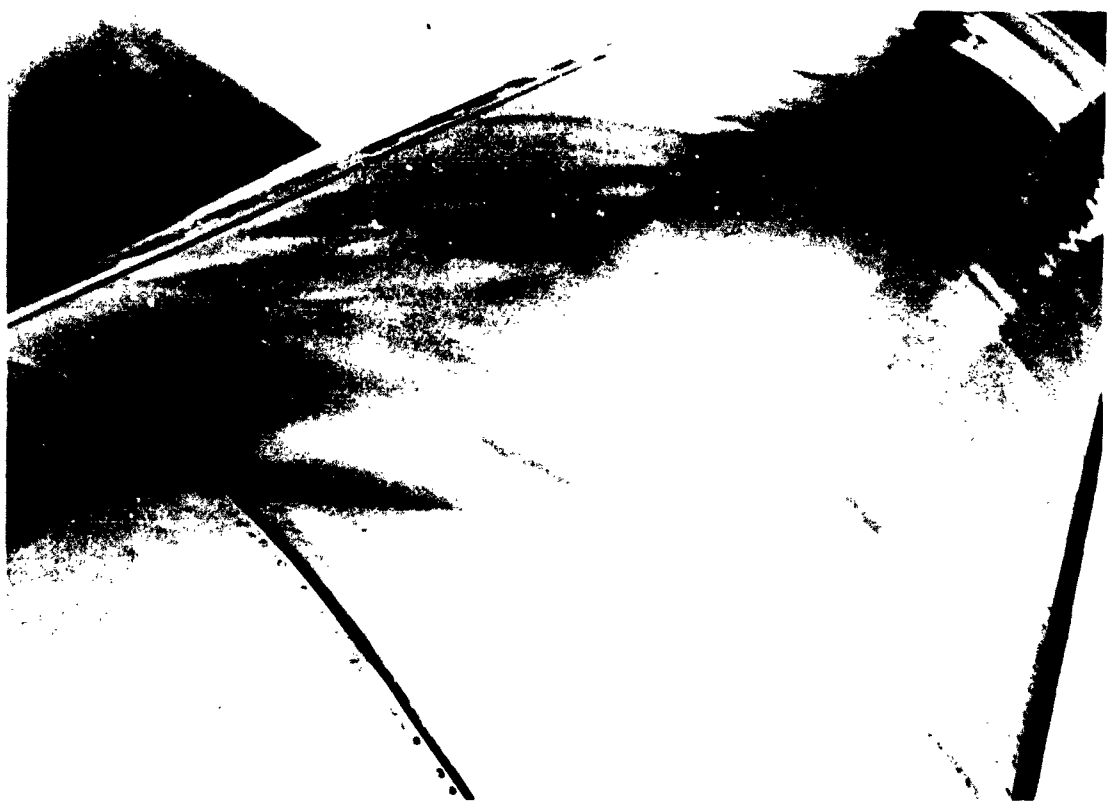

Figure 5.11 Gust damage evident in the bomb-bay area after Shot Dakota.

5.4.4 Engine Response. Initially it was expected that gust effects on the J-47-25 engine would result in increased tail-pipe temperature (TPT) to the point where an engine change would be necessary because of annealing and rupture of the tail-pipe complex. The cause of the temperature rise was a point of theoretical consideration, but most plausible causes were believed to be: (1) increase in TPT because of overpressure and unchoking of exhaust nozzle; and (2) change in inlet angle of attack because of gust, coupled with an increase in overpressure.

Unchoking of the exhaust nozzle resulted in a change of flow in the nozzle from supersonic to subsonic. This change in operating condition would cause some increase in temperature, but it was found in the Operation Redwing data that the change was negligible.

A change in compressor-inlet angle of attack and pressure could conceivably cause an increase in TPT, but the more significant and direct effect would be compressor stall. Compressor stall is caused in the J-47-25 engine by the fuel regulator, which senses compressor-inlet pressure; for an increase in pressure, the regulator causes more fuel to be released into the combustion chamber. Under gust conditions associated with a tail-on attitude of the aircraft, the angle of attack is increased and air flow is reduced. Thus, with more fuel and less air, the equivalent ratio decreases and frame temperatures increase. However, this type of compressor stall has been experienced under several types of operating conditions of the B-47E, and it is not probable that TPT would ever approach the limit of 1,850 F as a result of the gust effects from nuclear detonations.

Data obtained during Operation Redwing have demonstrated that limiting structural considerations preclude the probability of adverse engine effects of the J-47-25 on a B-47E aircraft. The 0.80 psi overpressure from Shot Dakota, associated with a peak gust velocity of 96.8 ft/sec at 45.8 degrees, caused a change of 4.0 degrees in the angle of attack. No adverse engine effects were noted; in fact, measured changes in engine parameters were significantly negligible. However, the bending moment at the critical wing station reached a peak of 89 percent of limit, and considerable blast damage was evidenced. Under operating conditions of the B-47E similar to those during Operation Redwing, it is not expected that the aircraft could be positioned to experience adverse engine effects without exceeding the structural limits of the aircraft.

Chapter 6
CONCLUSIONS and RECOMMENDATIONS

From the final data gathered by this project, the following conclusions and recommendations are made:

6.1 CONCLUSIONS

1. The participation of the B-47E aircraft in Operation Redwing provided sufficient structural-effects data to verify or correct the B-47E Weapons Delivery Handbook.
2. Predicted skin-temperature rises were higher than those measured. However, the thermal responses were sufficient to buckle large areas of thin-skinned control surfaces. These buckles did not produce any adverse effects on the control or stability of the aircraft.
3. The thin-skinned lower elevator panel on the B-47E aircraft will yield when subjected to temperature rises in the range of 350 to 450 F. However, this set will occur before failure in any primary structure.
4. White paint on the radome surface reduced the temperature rise to less than 50 percent of that existing in the unpainted areas.
5. The most critical of the tested wing stations was Station 615.0, with Station 493.0 being almost as critical. Gust response predictions at Station 615.0 were approximately 20 percent unconservative. Predictions at Wing Station 493.0 were approximately 40 percent conservative, and those at Wing Station 144.0 were approximately 30 percent conservative.
6. Under the conditions encountered during Operation Redwing the B-47 engines operated satisfactorily, and there were no indications that engine limitations could be approached without exceeding other structural limitations.
7. Predictions of radiant exposure were conservative with respect to actual measurements obtained. With respect to these measurements, correlation of integrated radiometer readings and those obtained from calorimeters was good.

6.2 RECOMMENDATIONS

1. It is recommended that the B-47E not participate in any future nuclear tests for the purposes of determining its weapon delivery capabilities. It is further recommended that the data gathered by this project be used to substantiate the B-47E Weapons Delivery Handbook.
2. It is also recommended that the data gathered by this project be used to verify and/or correct existing prediction techniques.

Appendix A
TRANSDUCER DATA

The following instruments were used to record all data: (1) oscillographs; (2) magnetic tape, (3) cameras; and (4) voice tape recorder.

TABLE A.1 SUMMARY OF TRANSDUCERS

Letters in parentheses indicate type of equipment used to record data: (A), oscillographs, (B), magnetic tape, and (C), cameras.

Transducers	Location	Recorded Channels	Range
1. Strain gage bridges for gust loads			
Bending Moment	L.W. Sta. 144.0	4 (A)	—
Shear	L.W. Sta. 144.0	7 (A)	—
Torsion	L.W. Sta. 144.0	2 (A)	—
Bending Moment	L.W. Sta. 493.0	4 (A)	—
Shear	L.W. Sta. 493.0	7 (A)	—
Torsion	L.W. Sta. 493.0	2 (A)	—
Bending Moment	R.W. Sta. 615.0	4 (A)	—
Shear	R.W. Sta. 615.0	4 (A)	—
Bending Moment	L.S. Sta. 22.0	7 (A)	—
Shear	L.S. Sta. 22.0	12 (A)	—
Bending Moment	R.S. Sta. 22.0	6 (A)	—
Shear	R.S. Sta. 22.0	9 (A)	—
Bending Moment	Fus. Sta. 800.0	8 (A)	—
Shear	Fus. Sta. 800.0	6 (A)	—
Bending Moment	Fus. Sta. 1044.0	10 (A)	—
Shear	Fus. Sta. 1044.0	7 (A)	—
2. Strain gage bridges for thermal loads			
Strain Rosette	L.E. Sta. 148.0	30 (A)	—
Strain Gage	L.E. Sta. 148.0	6 (A)	—
Strain Rosette	R.E. Sta. 148.0	24 (A)	—
Strain Gage	R.E. Sta. 148.0	4 (A)	—
Strain Rosette	Fus. Sta. 1330.0	6 (A)	—
3. Temperature			
Thermocouple	L.E. Sta. 148.0	15 (A)	−326 to 700 deg F
Thermocouple	R.E. Sta. 148.0	12 (A)	−326 to 700 deg F
Thermocouple	R.S. Sta. 192.0	5 (A)	−326 to 700 deg F
Thermocouple	R.S. Sta. 168.0	1 (A)	−326 to 700 deg F
Thermocouple	Fus. Sta. 1330.0	5 (A)	−326 to 700 deg F
Convection Calorimeter, uncovered	L.S. Sta. 192.0	3 (A)	−326 to 700 deg F
Convection Calorimeter, covered	L.S. Sta. 192.0	3 (A)	−326 to 700 deg F
Convection Calorimeter, uncovered	R.W. TE Sta. 476.0	1 (A)	−326 to 700 deg F
Convection Calorimeter, covered	R.W. TE Sta. 476.0	1 (A)	−326 to 700 deg F
Thermocouple - Radome	Fus. Sta. 202.0	6 (A)	−326 to 700 deg F
Thermocouple - Bomb Bay	Fus. Sta. 515.0	2 (A)	−326 to 700 deg F
Thermocouple - Bomb-Bay Door	Fus. Sta. 488.0	3 (A)	−326 to 700 deg F
Thermocouple - Bomb-Bay Door	Fus. Sta. 599.0	3 (A)	−326 to 700 deg F
Thermocouple - Central Recording Assembly	Fus. Sta. 515.0	2 (A)	−326 to 700 deg F
Thermocouple - Optigraph Mount	Fus. Sta. 446.0	1 (A)	−326 to 700 deg F
Thermocouple - Aileron	R.W. TE Sta. 476.0	3 (A)	−326 to 700 deg F
Thermocouple - Aileron	R.W. TE Sta. 767.0	3 (A)	−326 to 700 deg F
Thermocouple - Engine No. 6	R.W. Sta. 554.0	1 (A)	0 to 2,500 deg F
		1 (A)	−326 to 700 deg F
4. Thermal Radiation (Calorimeters and Radiometers)			
Ground Zero	Fus. Sta. 1330.0	18 (A)	—
True Vertical	Fus. Sta. 1227.0	3 (A)	—
Left Stabilizer	L.S. Sta. 156.0	1 (A)	—

TABLE A.1 CONTINUED

Letters in parentheses indicate type of equipment used to record data: (A), oscillographs, (B), magnetic tape, and (C), cameras.

Transducers	Location	Recorded Channels	Range
Radome	Fus. Sta. 202.0	2 (A)	—
Forward Scatter	Fus. Sta. 118.0	4 (B)	—
Forward Scatter	Fus. Sta. 446.0	2 (B)	—
Back Scatter	Fus. Sta. 1330.0	1 (A)	—
5. Pressure			
Overpressure	Fus. Sta. 292.0	1 (A)	P-131, ± 2.5 psid *
Overpressure	Fus. Sta. 1227.0	4 (A)	P-131, ± 2.5 psid *
Ram Monitor	Fus. Sta. 240.0	1 (A)	P-68, 0 to 30 psia
Static Monitor	Fus. Sta. 320.0	1 (A)	P-68, 0 to 10 psia
Engine Compressor Inlet	R. W. Sta. 554.0	2 (A)	P-69, 0 to 3 psid *
		1 (A)	P-69, 0 to 1 psid *
Engine Compressor Discharge	R. W. Sta. 554.0	1 (A)	P-96, ± 20 psid *
Tailpipe	R. W. Sta. 554.0	1 (A)	P-68, 0 to 30 psia
Small Slot Fuel System	R. W. Sta. 554.0	1 (A)	P-122, 0 to 500 psia
6. Angle of Attack			
Differential Pressure	L. S. Sta. 192.0	1 (A)	P-69, ± 1 psid *
Air Stream Direction Detector	V. F. Sta. 332.0	1 (A)	Model L-30, ± 15 deg
7. Linear Acceleration			
Vertical	Fus. Sta. 570.0	1 (A)	No. 24118, ± 5.0 g
Lateral	Fus. Sta. 573.0	1 (A)	No. 24118, ± 1.0 g
Longitudinal	Fus. Sta. 573.0	1 (A)	No. 24118, ± 2.5 g
8. Angular Acceleration			
Angular Accelerometer	Fus. Sta. 560.0	1 (A)	AA17B, ± 3 rad/sec^2
9. Rate of Pitch			
Rate Gyro	Fus. Sta. 573.0	1 (A)	RG-01-0200, 0 to 10 deg/sec
10. Position Indicators			
Rudder	Fus. Sta. 1194.0	1 (A)	No. 85175A, ± 20 deg
Elevator	Fus. Sta. 1180.0	1 (A)	No. 85175A, +25 −15 deg
Aileron	L. W. TE Sta. 461.0	1 (A)	No. 85175A, ± 18 deg
11. Deflection Indicators			
Push-Pull Pot	L. E. Sta. 148.0	2 (A)	± 0.5 in
12. Cameras			
Ground Zero	Fus. Sta. 1330.0	6 (C)	N-9, 16 mm
True Vertical	Fus. Sta. 1237.0	2 (C)	N-9, 16 mm
Wing Deflection	Fus. Sta. 446.0	2 (C)	Beattie, 35 mm
Wing Deflection	Fus. Sta. 446.0	1 (C)	N-9, 16 mm
Empennage Deflection	Fus. Sta. 446.0	1 (C)	N-9, 16 mm
Stabilizer Deflection	Fus. Sta. 1146.0	1 (C)	N-9, 16 mm
Elevator Ripple	Fus. Sta. 1248.0	2 (C)	N-9, 16 mm
Navigator's Panel	Fus. Sta. 135.0	1 (C)	A-4, 35 mm
Frame Correlation	Fus. Sta. 759.0	1 (C)	B1-A, 16 mm
Forward Scatter	Fus. Sta. 118.0	1 (C)	N-9, 16 mm
Cloud Cover	Fus. Sta. 275.0	1 (C)	N-9, 16 mm
Mapping	Fus. Sta. 1063.0	1 (C)	K-17

* Pounds per square inch, differential.

Appendix B
INPUT and RESPONSE THEORY

Outlines of methods used to predict thermal and blast effects of nuclear weapons and aircraft response to these inputs are presented in this appendix.

References are given for each analysis presented. Symbols used in each section correspond with the symbols used in the reference from which the analysis was taken.

B.1 OVERPRESSURE AND MATERIAL VELOCITY PREDICTION

Empirical expressions have been developed for predicting overpressure at a point in space due to a nuclear burst.

$$\Delta P_{sl} = \frac{34.5}{x} + \frac{68.1}{x^2} + \frac{4,140}{x^3} \quad \text{for } \Delta P_{sl} > 2 \text{ psi}$$

$$\Delta P_{sl} = \frac{31.3}{X\sqrt{\log_{10} x - 0.880}} \quad \text{for } \Delta P_{sl} < 2 \text{ psi}$$

$X = R/W^{1/3}$

R = range to point of interest, ft

W = weapon yield, pounds

ΔP_{sl} = sea level overpressure, psi

Relating this to an arbitrary burst altitude in a homogeneous atmosphere

$$\frac{\Delta P_b}{\Delta P_{sl}} = \frac{P_b}{P_{sl}}$$

ΔP_b = overpressure at burst altitude, psi

P_b = ambient pressure at burst altitude, psi

P_{sl} = ambient pressure at sea level, psi

Defining overpressure at any point in a homogeneous atmosphere and adding an exponential correction, α, relating overpressures at any point in a homogeneous atmosphere to the overpressures at any point in a stratified atmosphere.

$$\Delta P_h = \left[\frac{P_h}{P_b}\right]^{\alpha} \Delta P_b$$

ΔP_h = overpressure at any point, psi

P_h = ambient pressure at any point, psi

$\alpha = \alpha(Q_h)$

Where $Q_h = \Delta P_b / P_h$

Tables of α as a function of Q_h may be found in Reference 17.

The equation is plotted for the regimes of interest in Appendix B, WADC-TN-55-175.

Knowing ΔP at the point under consideration and the ambient pressure at this point the material velocity behind the shock may be found using tables of Rankine-Hugoniot relationships. For this purpose the pressure ratio across the shock may be written:

$$\frac{P_1}{P_0} = 1 + \frac{\Delta P}{P_0}$$

P_1 = ambient pressure behind shock, psi

P_0 = ambient pressure before shock, psi

ΔP = overpressure = $P_1 - P_0$, psi

Appendix B of WADC-TN-55-175 may be consulted for this complete analysis and for charts of these equations.

B.2 THERMAL ENERGY RECEIVED

For a spherical, isotropic source with no atmospheric attenuation the caloric input impinging normally to a surface

$$Q = 3.77 \times 10^7 \frac{W^{0.94}}{d^2}, \text{ cal/cm}^2$$

W = weapon yield, kt

d = distance from burst center, ft

For a hemispherical non-isotropic source with no atmospheric attenuation the caloric input impinging normally to a surface

$$Q_n = \frac{3.77 \times 10^7 (W)^{0.94}}{d^2} \left\{ (t_a/t_0) + (t_{hs}/t_0)\left[f(h, W)\cos(\tfrac{2}{3}\theta)\right], \right\} \text{ cal/cm}^2$$

t_a/t_0 = average power-weighted fraction of time spent by fireball as sphere

t_{hs}/t_0 = average power-weighted fraction of time spent by fireball as hemisphere

$f(h, W)$ = function describing energy emitting behavior of fireball during time it is a hemisphere

θ = angle enclosed by vertical line drawn through burst center and effective slant line of interest, deg

$\cos(\frac{2}{3}\theta)$ = factor expressing geometric consideration for non-isotropy of hemispherical fireball

Values of t_a/t_0 and t_{hs}/t_0 are established using a scaled burst height, $h/W^{1/3}$, where h = actual height of burst.

Finally, including effects of special orientation of the receiver, atmospheric attenuation, albedo, etc., the expression for total thermal energy impinging normal to a horizontal surface may be written,

$$Q_{rec} = Q_n\left[F_V(T_V\cos\theta + T'_V\rho\gamma) + F_{IR}(T_h T_w\cos\theta + T'_h T'_w \rho\gamma)\right]\Delta, \text{ cal/cm}^2$$

primed terms are for reflected radiation
unprimed terms are for direct radiation

T_V = fractional transmission due to scattering in visible range

F_V = fraction of thermal energy in visible region

ρ = surface albedo

γ = ratio of reflected to direct energy

F_{IR} = fraction of thermal energy in infrared region

T_h = fractional transmission due to scattering in haze layer for entire spectrum

T_w = fractional transmission due to water vapor absorption in infrared range

Δ = function of weapon yield (= 1 for w< 500 kt)

A much more detailed presentation of the analysis outlined above is included in WADC-TN-55-172, while a nomographic presentation for rapid calculation is the major portion of WADC-TN-55-172. The method of analysis was originally developed in AFCRC-TN-54-25.

B.3 RESPONSE TO BLAST LOADING

For a detailed discussion of the dynamic analysis used for the wing and horizontal stabilizer response to blast loading WADC-TN-55-175 and WADC-TR-53-176 must be consulted.

An outline of the analysis including calculation simplifications through the use of nomographs is presented here.

The incremental dynamic gust load factor, $\Delta n_{eg.}$, is the parameter used to establish limit allowable gust load envelopes.

$$\Delta n_{eg.} = (D.M.)\,\Delta n_r$$

(D. M.) = Dynamic Magnification Factor

Δn_r = incremental rigid-body gust load factor. This factor is a function of the weapon input and initial aircraft orientation.

$$\Delta n_r = \mu_1/\mu_0\sqrt{1 + (\bar{W}/U)^2 + 2(\bar{W}/U)\cos\phi}\left[1 + \frac{\bar{W}}{U}\,\frac{\sin(\phi + \alpha_0)}{\alpha_0}\right] - 1$$

μ_1 = peak density following shock wave, slugs/ft^3

μ_0 = ambient density, slugs/ft^3

$\bar{W}$ = peak material velocity following shock wave, ft/sec

α_0 = initial angle of attack, radian ($\sin\alpha_0 \cong \alpha_0$)

U = airplane initial velocity, ft/sec

ϕ = elevation angle from burst point to airplane in symmetrical plane, radians

Derivation of this equation is found on pages 45 to 47, WADC-TR-53-176.

The Dynamic Magnification Factor has been computed by means of the dynamic analysis described in detail in Appendix II of WADC-TR-53-176. It is a function of airplane forward speed, U, dimensionless duration of the positive phase of the pressure pulse, s_0, and airplane mass parameter, K.

$$s_0 = \frac{U t_0}{C/2}$$

U = true air speed, ft/sec

t_0 = duration of the positive phase of the pressure pulse, seconds

C = wing MAC, ft

Actual computation of s_0 is accomplished using Nomograph 3.1, page 26, WADC-TN-55-175.

$$K = \frac{\rho_0\,(C/4)\,S_W\,(C_{L\alpha})_a}{M}$$

S_W = wing area, ft^2

$(C_{L\alpha})_a$ = airplane lift slope, per radian

M = airplane mass, slugs

Computation of K is accomplished using Nomograph 3.2, pages 28 and 29, WADC-TN-55-175.

The wing Dynamic Magnification Factor may now be found using Nomograph 3.3, page 31, WADC-TN-55-175.

A (D. M.) is computed for the critical section of a particular wing, therefore, care should be used in extrapolating values for this factor to other wings.

Calculation of the horizontal stabilizer Dynamic Magnification Factor is the same as that for the wing. The parameter, s_0, is redefined using the horizontal stabilizer semi-mean aerodynamic chord, and K is assumed equal to zero.

B.4 THERMAL RESPONSE

Thermal response can be divided into two phases: (1) determining the temperature rise of a panel with a given thermal energy input; and (2) determining the maximum deflection of a panel with a given temperature rise.

A semi-empirical expression—

$$W = b/2\sqrt{2.408\,[f(a/b)\,\alpha_e\,\Delta T]}$$

W = maximum panel deflection, in

$f(a/b)$ = function of (a/b) as shown in Figure 2.1, page 11, WADC-TN-55-175

b = characteristic dimension of panel shown on Figure 2.1

ΔT = temperature rise, °F

α_e = $[\,11.8 + 0.00256\,(\Delta T + 2\,T_0 + 80°)\,] \times 10^{-6}$, per °F

T_0 = ambient temperature, °F

—was developed in Section IV of WADC-TN-55-176 and is presented on page 12 of WADC-TN-55-175.

Arbitrary acceptable damage levels may be chosen by specifying corresponding maximum deflections. The allowable temperature rise for the critical panel is then specified.

The temperature rise is given by

$$\Delta T = R\,\frac{Q_{rec}\,\alpha}{\rho C_p t}$$

α = absorptivity of the metal

ρ = density of the metal, pcf

R = ratio of temperature rise with cooling to temperature rise without cooling

C_p = specific heat of the metal, Btu/lb-°F

t = thickness of the metal, ft

Q_{rec} = thermal energy received, Btu/ft^2

The ratio R is given by the Department of Engineering, UCLA, as a plot of R versus $\bar{\tau}$ where

$$\bar{\tau} = \frac{h_c\,\tau}{\rho C_p t\,(3{,}600)}$$

τ = time to peak of the thermal pulse

$\tau \approx \sqrt{Mt}$ second

Mt = weapon yield in megatons

h_c = convective cooling coefficient, Btu/ft^2-°F-hr

$$h_c = 0.056\,T_f^{0.5}\,\frac{(u_x\,\gamma)^{0.5}}{(x)^{0.5}}\text{, for laminar flow}$$

$$h_c = 0.051\,T_f^{0.3}\,\frac{(u_x\,\gamma)^{0.8}}{(x)^{0.2}}\text{, for turbulent flow}$$

T_f = film temperature, $\frac{T_s + T_\gamma}{2}$, °R

T_s = surface temperature

T_γ = ambient temperature

γ = ambient air density, pcf

u_x = airfoil local velocity, ft/sec

x = distance from leading edge, ft

h_c equations developed in Appendix A, WADC-TR-52-216 Volume I.

The above calculation has been set up in nomographic form in Nomographs 2.1, 2.2, 2.3, 2.4, pages 7 to 10, WADC-TN-55-175. Entering the nomographs with true air speed, altitude and weapon yield $\Delta T/\alpha$ may be found for a specified Q_{rec} or Q_{rec} may be found for a specified $\Delta T/\alpha$.

All of the above except the convective cooling coefficient equations are presented in more detail in Section II of WADC-TN-55-175.

WADC-TN-55-172, August 1955; Wright Air Development Center, Wright-Patterson Air Force Base, Ohio; Secret Restricted Data.

15. D. J. Fink and J. M. Kane; "Handbook for the Computation of Dynamic Gust Loads Received by a B-50D Airplane Subjected to the Shock Wave of a Nuclear Explosion"; WADC-TR-53-176, July 1953; Wright Air Development Center, Wright-Patterson Air Force Base, Ohio; Secret Restricted Data.

16. A. Ambrosio, B. Bussell, and W. F. MacInnes; "Temperature Distributions in a Typical Aircraft Structure Due to Transient External Heating"; Volume I, T-33 Airplane, WADC-TR-52-216, April 1953; Wright Air Development Center, Wright-Patterson Air Force Base, Ohio; Unclassified.

17. F. O. Ledsham and H. H. M. Pike; "The Effect of Atmospheric Variations on the Propagation of Blast Waves to High Altitudes"; Report Number 31/50, January 1951; Armament Research Establishment, Great Britain; Secret Discreet.

DISTRIBUTION

Military Distribution Category 52

ARMY ACTIVITIES

1 Deputy Chief of Staff for Military Operations, D/A, Washington 25, D.C. ATTN: Dir. of SW&R
2 Chief of Research and Development, D/A, Washington 25, D.C. ATTN: Atomic Div.
3 Assistant Chief of Staff, Intelligence, D/A, Washington 25, D.C.
4 Chief of Engineers, D/A, Washington 25, D.C. ATTN: ENGTB
5- 6 Office, Chief of Ordnance, D/A, Washington 25, D.C. ATTN: ORDTW
7 Chief of Transportation, D/A, Office of Planning and Int., Washington 25, D.C.
8- 10 Commanding General, U.S. Continental Army Command, Ft. Monroe, Va.
11 Director of Special Weapons Development Office, Headquarters CONARC, Ft. Bliss, Tex. ATTN: Capt. Chester I. Peterson
12 President, U.S. Army Artillery Board, Ft. Sill, Okla.
13 President, U.S. Army Air Defense Board, Ft. Bliss, Tex.
14 President, U.S. Army Aviation Board, Ft. Rucker, Ala. ATTN: ATBG-DG
15 Commandant, U.S. Army Command & General Staff College, Ft. Leavenworth, Kansas. ATTN: ARCHIVES
16 Commandant, U.S. Army Air Defense School, Ft. Bliss, Tex. ATTN: Command & Staff Dept.
17 Commandant, U.S. Army Artillery and Missile School, Ft. Sill, Okla. ATTN: Combat Development Department
18 Commandant, U.S. Army Aviation School, Ft. Rucker, Ala.
19 Commandant, U.S. Army Ordnance School, Aberdeen Proving Ground, Md.
20 Commandant, U.S. Army Ordnance and Guided Missile School, Redstone Arsenal, Ala.
21 Commanding General, U.S. Army Chemical Corps, Research and Development Comd., Washington 25, D.C.
22- 23 Commanding Officer, Chemical Warfare Lab., Army Chemical Center, Md. ATTN: Tech. Library
24 Commanding Officer, Diamond Ord. Fuze Labs., Washington 25, D.C. ATTN: Chief, Nuclear Vulnerability Br. (230)
25- 26 Commanding General, Aberdeen Proving Grounds, Md. ATTN: Director, Ballistics Research Laboratory
27- 28 Commanding General, U.S. Army Ord. Missile Command, Redstone Arsenal, Ala.
29 Commander, Army Rocket and Guided Missile Agency, Redstone Arsenal, Ala. ATTN: Tech Library
30 Commanding General, White Sands Proving Ground, Las Cruces, N. Mex. ATTN: ORDBS-OM
31 Commander, Army Ballistic Missile Agency, Redstone Arsenal, Ala. ATTN: ORDAB-HT
32 Commanding General, Ordnance Ammunition Command, Joliet, Ill.
33 Commanding Officer, USA Transportation Research Command, Ft. Eustis, Va. ATTN: Chief, Tech. Info. Div.
34 Commanding Officer, USA Transportation Combat Development Group, Ft. Eustis, Va.
35 Director, Operations Research Office, Johns Hopkins University, 6935 Arlington Rd., Bethesda 14, Md.
36 Commander-in-Chief, U.S. Army Europe, APO 403, New York, N.Y. ATTN: Opot. Div., Weapons Br.

NAVY ACTIVITIES

37 Chief of Naval Operations, D/N, Washington 25, D.C. ATTN: OP-03EG
38 Chief of Naval Operations, D/N, Washington 25, D.C. ATTN: OP-75
39 Chief of Naval Operations, D/N, Washington 25, D.C. ATTN: OP-922G1
40- 41 Chief of Naval Research, D/N, Washington 25, D.C. ATTN: Code 811
42- 43 Chief, Bureau of Aeronautics, D/N, Washington 25, D.C.
44- 48 Chief, Bureau of Aeronautics, D/N, Washington 25, D.C. ATTN: AER-AD-41/20
49 Chief, Bureau of Ordnance, D/N, Washington 25, D.C.
50 Chief, Bureau of Ordnance, D/N, Washington 25, D.C. ATTN: S.P.
51 Director, U.S. Naval Research Laboratory, Washington 25, D.C. ATTN: Mrs. Katherine H. Cass
52- 53 Commander, U.S. Naval Ordnance Laboratory, White Oak, Silver Spring 19, Md.
54 Director, Material Lab. (Code 900), New York Naval Shipyard, Brooklyn 1, N.Y.
55 Commanding Officer, U.S. Naval Mine Defense Lab., Panama City, Fla.
56- 57 Commanding Officer, U.S. Naval Radiological Defense Laboratory, San Francisco, Calif. ATTN: Tech. Info. Di
58 Commandin Officer, U.S. Naval Schools Command, U.S. Naval Station, Treasure Island, San Francisco, Calif.
59 Superintendent, U.S. Naval Postgraduate School, Monterey, Calif.
60 Commanding Officer, Nuclear Weapons Training Center, Atlantic, U.S. Naval Base, Norfolk 11, Va. ATTN: Nuclear Warfare Dept.
61 Commanding Officer, Nuclear Weapons Training Center, Pacific, Naval Station, San Diego, Calif.
62 Commanding Officer, U.S. Naval Damage Control Tng. Center, Naval Base, Philadelphia 12, Pa. ATTN: ABC Defense Course
63 Commanding Officer, Air Development Squadron 5, VX-5, China Lake, Calif.
64 Director, Naval Air Experiment Station, Air Material Center, U.S. Naval Base, Philadelphia, Pa.
65 Commander, Officer U.S. Naval Air Development Center, Johnsville, Pa. ATTN: NAS, Librarian
66 Commanding Officer, Naval Air Sp. Wpns. Facility, Kirtland AFB, Albuquerque, N. Mex.
67 Commander, U.S. Naval Ordnance Test Station, China Lake, Calif.
68 Commandant, U.S. Marine Corps, Washington 25, D.C. ATTN: Code AO3H
69 Director, Marine Corps Landing Force, Development Center, MCS, Quantico, Va.
70 Commanding Officer, U.S. Naval CIC School, U.S. Naval Air Station, Glynco, Brunswick, Ga.

AIR FORCE ACTIVITIES

71 Assistant for Atomic Energy, HQ, USAF, Washington 25, D.C. ATTN: DCS/O
72 Hq. USAF, ATTN: Operations Analysis Office, Office, Vice Chief of Staff, Washington 25, D. C.
73- 74 Air Force Intelligence Center, HQ. USAF, ACS/I (AFCIN-3V1) Washington 25, D.C.
75 Director of Research and Development, DCS/D, HQ. USAF, Washington 25, D.C. ATTN: Guidance and Weapons Div.
76 The Surgeon General, HQ. USAF, Washington 25, D.C. ATTN: Bio.-Def. Pre. Med. Division
77 Commander, Tactical Air Command, Langley AFB, Va. ATTN: Doc. Security Branch
78 Commander, Air Defense Command, Ent AFB, Colorado. ATTN: Assistant for Atomic Energy, ADLDC-A
79 Commander, Hq. Air Research and Development Command, Andrews AFB, Washington 25, D.C. ATTN: RDSWA
80 Commander, Air Force Ballistic Missile Div. HQ. ARDC, Air Force Unit Post Office, Los Angeles 45, Calif. ATTN: WDSOT
81- 82 Commander, AF Cambridge Research Center, L. G. Hanscom Field, Bedford, Mass. ATTN: CRQST-2
83- 87 Commander, Air Force Special Weapons Center, Kirtland AFB, Albuquerque, N. Mex. ATTN: Tech. Info. & Intel. Div.

88- 89 Director, Air University Library, Maxwell AFB, Ala.
90 Commander, Lowry Technical Training Center (TW), Lowry AFB, Denver, Colorado.
91 Commandant, School of Aviation Medicine, USAF, Randolph AFB, Tex. ATTN: Research Secretariat
92 Commander, 1009th Sp. Wpns. Squadron, HQ. USAF, Washington 25, D.C.
93- 95 Commander, Wright Air Development Center, Wright-Patterson AFB, Dayton, Ohio. ATTN: WCOSI
96- 97 Director, USAF Project RAND, VIA: USAF Liaison Office, The RAND Corp., 1700 Main St., Santa Monica, Calif.
98 Commander, Air Defense Systems Integration Div., L. G. Hanscom Field, Bedford, Mass. ATTN: SIDE-3
99 Chief, Ballistic Missile Early Warning Project Office, 220 Church St., New York 13, N.Y. ATTN: Col. Leo V. Skinner, USAF
100 Commander, Air Technical Intelligence Center, USAF, Wright-Patterson AFB, Ohio. ATTN: AFCIN-4Bla, Library
101 Assistant Chief of Staff, Intelligence, Hq. USAFE, APO 633, New York, N.Y. ATTN: Directorate of Air Targets
102 Commander-in-Chief, Pacific Air Forces, APO 953, San Francisco, Calif. ATTN: PFCIE-MB, Base Recovery

OTHER DEPARTMENT OF DEFENSE ACTIVITIES

103 Director of Defense Research and Engineering, Washington 25, D.C. ATTN: Tech. Library
104 Chairman, Armed Services Explosives Safety Board, DOD, Building T-7, Gravelly Point, Washington 25, D.C.
105 Director, Weapons Systems Evaluation Group, Room 1E880, The Pentagon, Washington 25, D.C.
106-109 Chief, Defense Atomic Support Agency, Washington 25, D.C. ATTN: Document Library
110 Commander, Field Command, DASA, Sandia Base, Albuquerque, N. Mex.
111 Commander, Field Command, DASA, Sandia Base, Albuquerque, N. Mex. ATTN: FCTG
112-116 Commander, Field Command, DASA, Sandia Base, Albuquerque, N. Mex. ATTN: FCWT
117 Administrator, National Aeronautics and Space Administration, 1520 "H" St., N.W., Washington 25, D.C. ATTN: Mr. R. V. Rhode
118 Commander-in-Chief, Strategic Air Command, Offutt AFB, Neb. ATTN: OAWS
119 Commander-in-Chief, EUCOM, APO 128, New York, N.Y.

ATOMIC ENERGY COMMISSION ACTIVITIES

120-122 U.S. Atomic Energy Commission, Technical Library, Washington 25, D.C. ATTN: For DMA
123-124 Los Alamos Scientific Laboratory, Report Library, P.O. Box 1663, Los Alamos, N. Mex. ATTN: Helen Redman
125-129 Sandia Corporation, Classified Document Division, Sandia Base, Albuquerque, N. Mex. ATTN: H. J. Smyth, Jr.
130-131 University of California Lawrence Radiation Laboratory, P.O. Box 808, Livermore, Calif. ATTN: Clovis G. Craig
132 Essential Operating Records, Division of Information Services for Storage at ENC-H. ATTN: John E. Hans, Chief, Headquarters Records and Mail Service Branch, U.S. AEC, Washington 25, D.C.
133 Weapon Data Section, Technical Information Service Extension, Oak Ridge, Tenn.
134-170 Technical Information Service Extension, Oak Ridge, Tenn. (Surplus)